Modeling Geometric and Hemodynamic Cues in Cardiovascular Biology

Christian Mandrycky

A dissertation
submitted in partial fulfillment of the
requirements for the degree of

Doctor of Philosophy

University of Washington
2020

Reading Committee:
Ying Zheng, Chair
Michael Regnier,
Barry Gumbiner

Program Authorized to Offer Degree:
Bioengineering

University of Washington

Abstract

Modeling Geometric and Hemodynamic Cues in Cardiovascular Biology

Christian Mandrycky

Chair of Supervisory Committee:

Ying Zheng

Department of Bioengineering

From the capillaries to the aorta, the behavior of endothelial cells lining the vasculature is guided by local hemodynamic conditions that can induce both development and disease. Much remains unknown, however, about how these local conditions are integrated by endothelial cells to produce both endothelial and parenchymal responses. The lack of in vitro models that enable careful perturbation with the diversity of biophysical conditions present in vivo has been a barrier to a deeper understanding of these responses. The following dissertation reports on the development of model systems to further understand the role of geometric and hemodynamic cues on the response of endothelial cells to flow and their interactions with parenchymal populations. We first develop a spiral microvessel model that enables precise control of vessel curvature and torsion, showing that modification of these geometric features can alter the response of endothelial cells and shedding light on the role of structural heterogeneity in vascular biology. We further interrogate these curvature induced effects in a large vessel aneurysm model, demonstrating changes in endothelial phenotype are associated with geometric and hemodynamic conditions. Based on insights from these experiments we then investigate the role of pressure in endothelial flow sensing and vascular remodeling. We find that pressure conditions help shape the endothelial response to shear stress and can also guide vascular remodeling in engineered tissues. To enable further study of pressure induced effects we finally develop a perfusable model of early heart development in which pressure stimulated endothelial-cardiomyocyte interactions can be interrogated. By modeling these diverse geometric and hemodynamic features we gain valuable new insights into endothelial biology and provide new tools for investigating endothelial responses to blood flow and interactions with cardiovascular tissues.

Contents

Acknowledgements

I would first like to thank my advisor, Dr. Ying Zheng, for her support and guidance throughout my graduate education. Ying trusted me with considerable freedom to pursue a wide range of projects while also ensuring things stayed on track. I will forever be grateful for her seemingly endless enthusiasm and her incredible ability to find positivity and motivation in even the bleakest seeming results. I would also like to thank the members of the Gree team, Drs. Nathan Sniadecki, Kelly Stevens, Jen Davis, Cole DeForest, Deok-Ho Kim, Charles Murry, and Michael Regnier, for their insight and support over the course of my training. It was an incredible privilege to regularly have the eyes and ears of so many extraordinarily talented scientists. I would also like to thank Dr. Barry Gumbiner for his insightful and carefully considered feedback which has helped shape this work. Thank you also to Dr. Brandon Hadland, for his expertise and collaboration on several sequencing experiments.

I must also thank the members of the Zheng lab for their friendship and support throughout graduate school. From late night microscope sessions to relay races, you all provided an incredibly welcoming, supportive, and entertaining environment in which to have spent my graduate years.

Most importantly I would like to thank my family. To my sisters, Claire and Nicole, for their love and support. To my parents, Cathy and Nick, for their unwavering and unquestioning support and unflappable belief in me I am extraordinarily grateful. To our cat, Luna, for countless nights of keeping my feet company or lap occupied. And finally to my wife, Alex, for her love, support, and, somewhat frequently, her programming skills.

1. Chapter 1: Motivation and Specific Aims

1.1 Research Motivation

From the earliest stages of development through adult life, the cardiovascular system is under constant revision. Hemodynamic forces[1,2] and a variety of signaling pathways[3–5] play key roles in both cardiac and vascular remodeling *in vivo*. Pressure gradients, flow shear, and interstitial flow have been shown in several *in vitro* systems to regulate cellular alignment,[6,7] morphogenesis,[8] and angiogenesis.[9] Nonetheless, a fundamental understanding of the role of hemodynamic forces in cardiac and vascular remodeling remains elusive, and is partially attributed to the absence of *in vitro* models that challenge cells with the full range of normal biophysical forces. The goal of this dissertation work is to address this challenge by engineering cardiovascular systems for the study of the hemodynamic factors and cellular mechanisms that control vascular and cardiac remodeling, and to utilize this knowledge to guide the development of engineered tissues.

This will be achieved through three aims, each involving the development of new tools to unravel the role of biophysical forces in cardiovascular biology. In Aim 1, we will engineer and characterize vessels that mimic the geometry and biophysical forces experienced by cells *in vivo*. In Aim 2, we will evaluate the role of pressure in the endothelial response to flow and the regulation of vascular remodeling. Finally, in Aim 3 we will apply this approach to cardiac tissue engineering and develop a model based on early heart development to investigate the effect the of hemodynamic forces on engineered heart tissues.

1.2 Specific Aims

1.1.1 Aim 1 Engineer blood vessels with 3D curvature

Hypothesis: Endothelial cell phenotype will be altered by changes in blood vessel curvature and flow. Blood vessels twist and curve in three dimensions throughout the body, but existing *in vitro* systems fail to capture this complexity. As a result, a more complete understanding of the independent effects of flow in 3D blood vessels on the endothelium has been limited. We developed a platform to engineer blood vessels with controlled curvature to produce vascularized 3D tissues and to determine the response of endothelial cells to the fluid dynamics of flow in curved vessels. We will demonstrate that endothelial cell gene expression is altered by curvature and flow.

1.1.2 Aim 2: Determine the effect of pressure on the endothelial response to shear stress and vascular remodeling.

Hypothesis: Changes in hydrostatic pressure can modulate the endothelial response to shear stress and can alter vascular remodeling in engineered 3D tissues

A fundamental understanding of how the different hemodynamic forces interact to form a coherent endothelial response remains elusive. In particular, the role of pressure in flow sensing and vascular remodeling is not well defined despite its fluctuations in both disease and development. We will develop systems to determine if pressure alters endothelial cell phenotype and if pressure can serve as a guiding cue to create hierarchy in engineered blood vessels.

1.1.3 Aim 3: Develop a model for investigating the effect of hemodynamic conditioning on engineered cardiac tissues

Hypothesis: Hemodynamic conditions can be used to control endothelial-myocardial crosstalk and promote PSC-derived cardiomyocyte maturation.

The development of functional engineered cardiac tissues has been hampered by challenges in promoting stem cell derived cardiomyocyte (CM) maturation. While mechanical cues promote CM maturation, adult-like CM have not yet been created *de novo*. In addition to the mechanical stresses present in development, signaling between the endocardium and myocardium is essential for the development of the heart. In this aim we create a developmentally inspired cardiac tube model to determine if hemodynamic forces can be used to promote CM maturation through mechanical stimulation and endothelial-myocardial signaling.

1.3 References

1. Lucitti, J. L. *et al.* Vascular remodeling of the mouse yolk sac requires hemodynamic force. *Dev. Camb. Engl.* **134,** 3317–26 (2007).

2. Udan, R. S., Vadakkan, T. J. & Dickinson, M. E. Dynamic responses of endothelial cells to changes in blood flow during vascular remodeling of the mouse yolk sac. *Dev. Camb. Engl.* **140,** 4041–50 (2013).

3. Stratman, A. N., Davis, M. J. & Davis, G. E. VEGF and FGF prime vascular tube morphogenesis and sprouting directed by hematopoietic stem cell cytokines. *Blood* **117,** 3709–3719 (2011).

4. Baeyens, N. *et al.* Vascular remodeling is governed by a VEGFR3-dependent fluid shear stress set point. *eLife* **4,** e04645 (2015).

5. Fischer, A., Schumacher, N., Maier, M., Sendtner, M. & Gessler, M. The Notch target genes Hey1 and Hey2 are required for embryonic vascular development. *Genes Dev.* **18,** 901–911 (2004).

6. Ng, C. P. & Swartz, M. A. Fibroblast alignment under interstitial fluid flow using a novel 3-D tissue culture model. *Am. J. Physiol. Heart Circ. Physiol.* **284,** H1771-7 (2003).

7. Polacheck, W. J., Charest, J. L. & Kamm, R. D. Interstitial flow influences direction of tumor cell migration through competing mechanisms. *Proc. Natl. Acad. Sci. U. S. A.* **108,** 11115–20 (2011).

8. Helm, C.-L. E., Fleury, M. E., Zisch, A. H., Boschetti, F. & Swartz, M. A. Synergy between interstitial flow and VEGF directs capillary morphogenesis in vitro through a gradient amplification mechanism. *Proc. Natl. Acad. Sci.* **102,** 15779–15784 (2005).

9. Vickerman, V. & Kamm, R. D. Mechanism of a flow-gated angiogenesis switch: early signaling events at cell-matrix and cell-cell junctions. *Integr. Biol. Quant. Biosci. Nano Macro* **4,** 863–74 (2012).

2. Chapter 2: Introduction

2.1 Vascular development and remodeling

The vasculature takes shape through multiple processes during development and is regulated throughout life. New blood vessels form through vasculogenesis, where endothelial cells or endothelial precursors form tubules and self-assemble into vascular structures.[1] This is a distinct process from angiogenesis, or the growth of new blood vessels off the existing vasculature by endothelial proliferation and migration.[2] Vascular regression and pruning compete with these methods of vascular expansion to act to maintain an efficient vascular network.[3]

In the embryo these processes are all on display. The first blood vessels form as mesodermal endothelial precursors (angioblasts) surround primitive blood cells that have aggregated to form blood islands.[4] These cells undergo vasculogenesis as they coalesce around the blood islands in the embryonic yolk sac to form early vessels (around embryonic day 7.5 in the mouse). Angiogenesis supports the anastomosis of island to island and in this process forms a dense vascular plexus with little apparent hierarchy. This changes rapidly as the heart tube forms and blood begins to flow. Overnight, the vascular bed undergoes significant remodeling to pare down the plexus to an organized and hierarchical vascular network with vessels of different size and smooth muscle coating.[5]

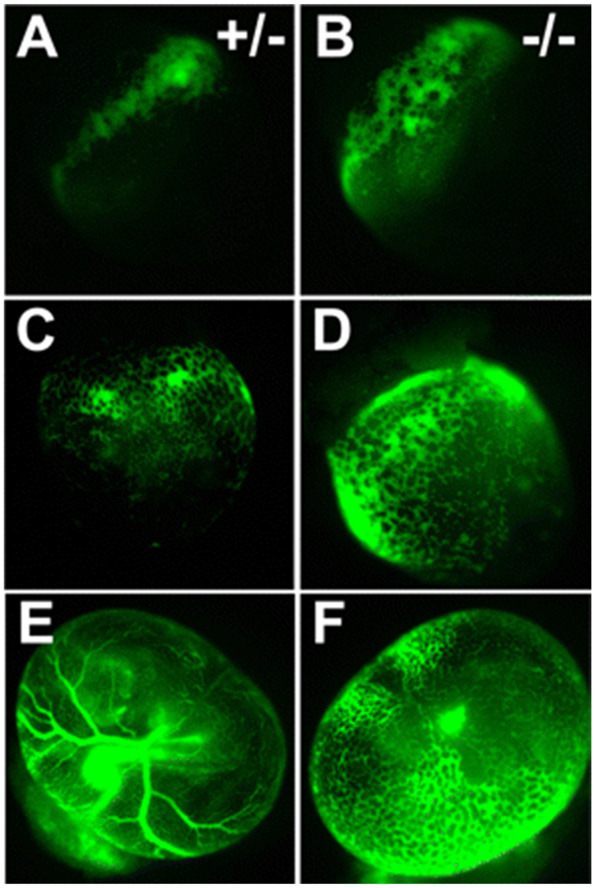

Figure 1. The yolk sac vasculature requires flow to remodel. The vascular plexus takes shape at E7.5 (A,B), E8.5 (C,D), and E9.5 (E, F). With knockout of MLC2a and an interruption to the heartbeat (B,D,F) this plexus does not remodel to form a hierarchical vasculature as it does in wild-type (A,C,E) mice. Green cells are GFP expressing erythroblasts. Figure adapted from Lucitti et al.

Here the Notch signaling pathway plays an important role. The Notch transmembrane receptor and its family of ligands are involved in vascular remodeling, where loss of function mutants can prevent the remodeling of the yolk sac plexus.[6] Loss of the core endothelial Notch receptor (Notch1) prevents vascular remodeling at this stage as well as other problems across the embryo.[7] Disruption in the expression of individual Notch ligands, including Dll4 and Jag1, also acts against the formation of a branched hierarchical vascular network.[8,9] Loss of the Notch target genes Hey1 and Hey2 result in similar remodeling defects.[10]

Remodeling at this stage is also dependent on flow through the vascular bed. If the heartbeat is disrupted by mutation to atrial myosin light chain 2 (MLC2a), this plexus does not undergo normal remodeling (Figure 1).[11,12] Lucitti and colleagues showed through careful analysis that this result is dependent on fluid forces on the endothelium, illustrating the importance of hemodynamics in the vasculature from the earliest stages of development. Mechanosensory components of the endothelial cell are activated in this stage of remodeling, but it is not clear what the key regulators of that process are. How the cell senses flow and transduces this into phenotypic changes is an essential feature of the endothelium.

2.2 Endothelial mechanotransduction and *in vitro* models of flow

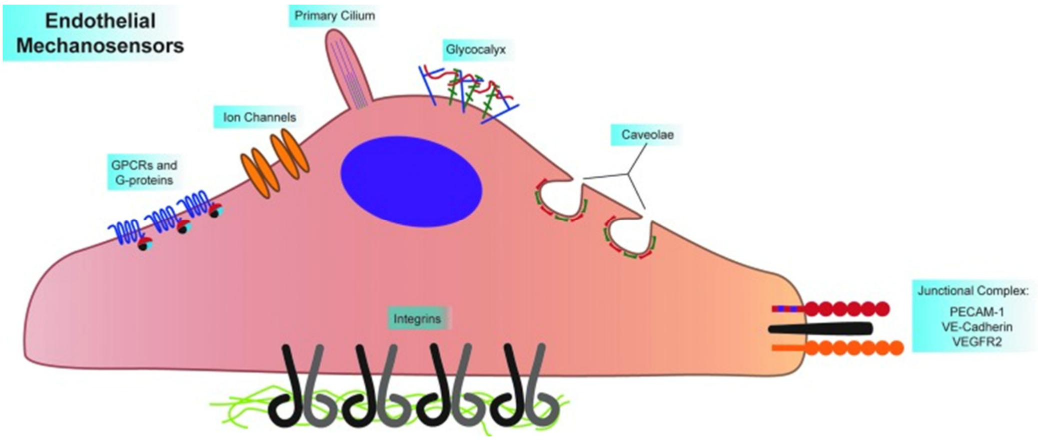

Figure 2. Mechanosensors line the endothelial cell. Mechanosensory proteins and structures exist on all surfaces of the endothelial cell and include direct sensors of mechanical force like PECAM-1 as well as secondary and adaptor proteins like VEGFR2.Figure adapted from Givens and Tzima.[13]

In lining the blood vessels endothelial cells (ECs) act as both a barrier and an interpreter. ECs sense patterns of shear stress and pressure in the circulatory system and initialize different cellular programs. To serve this function endothelial cells harbor a wide array of mechanosensory components (Figure 2).

Many of these sensors exist on the EC's apical surface. G-protein coupled receptors (GPCRs) are both involved in directly sensing shear stress as well as transducing shear induced signals downstream. For example, the bradykinin B2 receptor has been shown to undergo a conformational change in response to flow,[14] whereas the sphingosine-1-phosphate receptor ($S1P_1$) is a necessary component in activating other downstream shear responsive pathways.[15] Mechanosensitive ion channels including Piezo1[16] and TRPV4[17] act to depolarize the cell under shear stress. Some ECs in development or in regions of low shear stress express primary cilia,[18] which directly sense shear stress.[19,20]

Endothelial junctions are a source of additional mechanosensors. CD31 (Platelet endothelial cell adhesion molecule) is phosphorylated on the onset of flow[13] and can induce shear stress-like signaling when it is mechanically brought under tension.[21] VE-cadherin can act as a partner to CD31 in the shear-response cascade,[22] or it can induce shear signaling alone when under tension.[23] Other junctional molecules, including VEGFR2 and -3 are implicated in the shear response pathway, but it is not yet clear if they directly detect mechanical signals.[24,25] A variety of molecules fall into this shear-related category where there is not convincing evidence that they are mechanically sensitive. These are important components of the shear-response pathway and include integrins,[26,27] Tie receptors,[28] NOTCH1,[29] and other proteins.[13]

On signaling from these sensors, a variety of downstream effectors are activated by flow. ERK and JNK signaling pathways are activated by laminar flow, and contribute to matrix and cytoskeletal remodeling.[30–33] Nitric oxide (NO) production is rapidly ramped up through endothelial nitric oxide synthase (eNOS) and triggers additional intracellular changes as well as signaling to neighboring cells, like smooth muscle cells, where it can regulate vascular tone.[34,35] Importantly, these signals are dependent on the kind of flow sensed by ECs. In regions of disturbed flow, like near vessel bifurcations or in bends, the patterns of shear-activation are altered and lead to inflammatory signals through VCAM-1, ICAM-1 and other molecules that bring monocytes and leukocytes to the vessel wall.[36]

These discoveries have come through a combination of *in vitro* and *in vivo* investigations. Methods for pursuing disturbed flow in engineered model systems, however, rarely place endothelial cells in biomimetic conditions. Common approaches use parallel plate flow chambers[37] or cone-plate viscometers[38] to apply shear stress to endothelial monolayers. While the shear conditions on endothelial cells are precisely controlled in these systems, they do not resemble the native environment in a blood vessel. Blood vessels in the body have curvature and wind through space, causing alterations in the kind of flow that develops in the vessel and ultimately the response of ECs.[39] In vitro systems that recapitulate this can help elucidate this endothelial response in the absence of complicating factors found *in vivo*.

2.3 Heart development

Endothelial mechanosensing is functionally important for cardiac development as well. In the mouse, cardiomyocytes differentiate and begin beating as a closed heart tube is fully formed and pumping by embryonic day 8.5 (E8.5).[40] The transition between a linear heart tube and a 4-chambered heart is an incredibly complex process characterized by many levels of cell differentiation and large morphological changes.[41] In this process and the steps of growth and maturation that follow it, disruption of normal signaling pathways can lead to congenital heart defects.[42] This includes signals between the endothelial-like endocardial cells that line the inside of the heart.

Endothelial production of a variety of factors, including neuregulin (Nrg), neurofibromatosis type 1 (NF1), and platelet derived growth factor-B (PDGF-B) influence cardiac phenotype. Nrg can stimulate cardiomyocyte differentiation and proliferation in the heart and its knockout is embryonic lethal by E10.5 with an abnormally thin myocardium.[43] Endothelial specific inactivation of NF1 results in multiple cardiac deformations, including ventricular septal defects and thinning of the myocardium.[44] PDGF-B knockout mice display similar flaws in cardiac structure.[45]

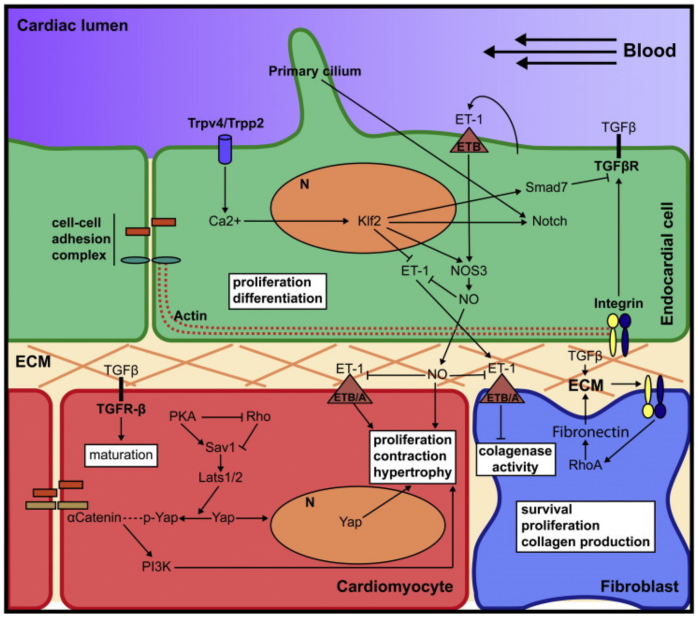

Figure 3. Shear sensitive endocardial-cardiomyocyte signaling pathways. Shear stress activates signaling pathways in the endocardium that affect cardiomyocytes. Disruption of normal flow profiles can alter endocardial-myocardial crosstalk and lead to cardiac defects. Figure adapted from Andreas-Delgado and Mercader.

The endocardium possesses much of the same flow sensing machinery as the vascular endothelium, and flow sensitive pathways in the endocardium act on cardiomyocytes throughout development (Figure 3).[46] Endothelin-1 (ET-1) release is mediated by shear stress,[47] and its knockout in mice causes septal defects in development.[48] ET-1 can also modify cardiomyocyte constriction by increasing intracellular calcium on binding the ET_A receptor.[49] Stretching of the endocardium can also cause upregulation of ET-1 through TRPC-6 ion channels.[50] Shear sensitive NO signaling can alter ET-1 production and modulate cardiomyocyte constriction. Unsurprisingly, loss of eNOS in mice leads to congenital heart defects.[51,52] Flow induced changes in Klf2 expression also affect the myocardium, as loss of Klf2 leads to heart failure and embryonic death by E14.5.[53]

The endocardial/myocardial signaling axis is clearly important in cardiac development, but few engineered cardiac systems incorporate both the cells and the hemodynamic signals that drive this pathway. Recapitulating this pathway *in vitro* may be a useful approach to investigate the dynamics of endocardial/myocardial crosstalk and ultimately produce more effective engineered tissues.

2.4 Significance

Engineering vessels with 3-dimensional curvature and flow

It is widely appreciated that bifurcations and bends in large vessels are sites of inflammation and disease, but cellularized *in vitro* models that mimic these conditions for large or small vessels do not exist. Approximations are made using simplified culture platforms, or studies are performed in living animals where control over hemodynamic factors is significantly restricted. These limitations impede the development of a more formal understanding of the vascular response to all types of flow in the vasculature. Through our aims, we will address this shortcoming of current model systems and characterize the response of endothelial cells to 3D flow in curved vessels *in vitro*. This will be useful not only for investigating the effect of flow on the endothelium, but also for interactions with cells that can be incorporated into the parenchyma.

The effect of pressure on endothelial cell shear sensing and vascular remodeling

Blood flow in the vasculature is a key driver of endothelial cell function, but a fundamental understanding of how the different hemodynamic forces interact to form a coherent endothelial response remains elusive. In particular, the role of pressure in flow sensing and in vascular remodeling is poorly understood. Pressure levels are elevated in prevalent diseases (i.e. hypertension), but little is known regarding the mechanisms by which this force is transduced and the effect it has on endothelial cells. In other developmental and pathological conditions relating to the development of vascular networks and vascular hierarchy, pressure levels are also variable. Through these aims we will probe the effect of pressure conditions on endothelial cell mechanotransduction, determining if it alters endothelial shear sensing pathways and if it contributes to 3D vascular remodeling. Addressing these unknowns will help reveal the role of pressure across multiple endothelial functions, indicating if it will have utility in manipulating endothelial cell behavior in disease or in the development of engineered tissues.

Determining the effect of cardiomyocyte-endothelial crosstalk on cardiac maturation

The maturation of PSC-derived cardiomyocytes remains an open problem in tissue engineering. Cardiomyocytes and endothelial cells are closely linked from the earliest stages of development and signaling between these two cell types is key to the formation of healthy cardiac tissue. We will engineer a model system to enable the study of the effect of hemodynamic cues on cardiac tissue development. In this system endothelial-myocardial signaling derived from hemodynamic cues acting on both cell types will allow for the effect of this signaling axis on engineered cardiac constructs to be determined.

2.5 References

1. Udan, R. S., Culver, J. C. & Dickinson, M. E. Understanding vascular development. *Wiley Interdiscip. Rev. Dev. Biol.* **2,** 327–346 (2013).
2. Drake, C. J. Embryonic and adult vasculogenesis. *Birth Defects Res. Part C Embryo Today Rev.* **69,** 73–82 (2003).
3. Ricard, N. & Simons, M. When it is better to regress: dynamics of vascular pruning. *PLoS Biol.* **13,** e1002148 (2015).
4. Ferkowicz, M. J. & Yoder, M. C. Blood island formation: longstanding observations and modern interpretations. *Exp. Hematol.* **33,** 1041–1047 (2005).
5. Blatnik, J. S., Schmid-Schönbein, G. W. & Sung, L. A. The influence of fluid shear stress on the remodeling of the embryonic primary capillary plexus. *Biomech. Model. Mechanobiol.* **4,** 211–220 (2005).
6. Hofmann, J. J. & Iruela-Arispe, M. L. Notch signaling in blood vessels: Who is talking to whom about what? *Circ. Res.* **100,** 1556–1568 (2007).
7. Krebs, L. T. *et al.* Notch signaling is essential for vascular morphogenesis in mice. *Genes Dev.* **14,** 1343–1352 (2000).
8. Gale, N. W. *et al.* Haploinsufficiency of delta-like 4 ligand results in embryonic lethality due to major defects in arterial and vascular development. *Proc. Natl. Acad. Sci.* **101,** 15949–15954 (2004).
9. Xue, Y. *et al.* Embryonic lethality and vascular defects in mice lacking the Notch ligand Jagged1. *Hum. Mol. Genet.* **8,** 723–730 (1999).
10. Fischer, A., Schumacher, N., Maier, M., Sendtner, M. & Gessler, M. The Notch target genes Hey1 and Hey2 are required for embryonic vascular development. *Genes Dev.* **18,** 901–911 (2004).
11. Huang, C. *et al.* Embryonic atrial function is essential for mouse embryogenesis, cardiac morphogenesis and angiogenesis. *Development* **130,** 6111–6119 (2003).
12. Lucitti, J. L. *et al.* Vascular remodeling of the mouse yolk sac requires hemodynamic force. *Dev. Camb. Engl.* **134,** 3317–26 (2007).
13. Givens, C. & Tzima, E. Endothelial Mechanosignaling: Does One Sensor Fit All? *Antioxid. Redox Signal.* **25,** 373–388 (2016).
14. Chachisvilis, M., Zhang, Y.-L. & Frangos, J. A. G protein-coupled receptors sense fluid shear stress in endothelial cells. *Proc. Natl. Acad. Sci. U. S. A.* **103,** 15463–15468 (2006).
15. Jung, B. *et al.* Flow-regulated endothelial S1P receptor-1 signaling sustains vascular development. *Dev. Cell* **23,** 600–610 (2012).
16. Ranade, S. S. *et al.* Piezo1, a mechanically activated ion channel, is required for vascular development in mice. *Proc. Natl. Acad. Sci. U. S. A.* **111,** 10347–10352 (2014).
17. Köhler, R. & Hoyer, J. Role of TRPV4 in the Mechanotransduction of Shear Stress in Endothelial Cells. in *TRP Ion Channel Function in Sensory Transduction and Cellular Signaling Cascades* (eds. Liedtke, W. B. & Heller, S.) (CRC Press/Taylor & Francis, 2007).
18. Goetz, J. G. *et al.* Endothelial cilia mediate low flow sensing during zebrafish vascular development. *Cell Rep.* **6,** 799–808 (2014).
19. Nauli, S. M. *et al.* Endothelial cilia are fluid shear sensors that regulate calcium signaling and nitric oxide production through polycystin-1. *Circulation* **117,** 1161–1171 (2008).
20. Van der Heiden, K. *et al.* Endothelial primary cilia in areas of disturbed flow are at the base of atherosclerosis. *Atherosclerosis* **196,** 542–550 (2008).
21. Collins, C. *et al.* Localized tensional forces on PECAM-1 elicit a global mechanotransduction response via the integrin-RhoA pathway. *Curr. Biol. CB* **22,** 2087–2094 (2012).
22. Tzima, E. *et al.* A mechanosensory complex that mediates the endothelial cell response to fluid shear stress. *Nature* **437,** 426–431 (2005).

23. Barry, A. K., Wang, N. & Leckband, D. E. Local VE-cadherin mechanotransduction triggers long-ranged remodeling of endothelial monolayers. *J. Cell Sci.* **128,** 1341–1351 (2015).
24. Shay-Salit, A. *et al.* VEGF receptor 2 and the adherens junction as a mechanical transducer in vascular endothelial cells. *Proc. Natl. Acad. Sci. U. S. A.* **99,** 9462–9467 (2002).
25. Coon, B. G. *et al.* Intramembrane binding of VE-cadherin to VEGFR2 and VEGFR3 assembles the endothelial mechanosensory complex. *J. Cell Biol.* **208,** 975–986 (2015).
26. Tzima, E., del Pozo, M. A., Shattil, S. J., Chien, S. & Schwartz, M. A. Activation of integrins in endothelial cells by fluid shear stress mediates Rho-dependent cytoskeletal alignment. *EMBO J.* **20,** 4639–4647 (2001).
27. Jalali, S. *et al.* Integrin-mediated mechanotransduction requires its dynamic interaction with specific extracellular matrix (ECM) ligands. *Proc. Natl. Acad. Sci. U. S. A.* **98,** 1042–1046 (2001).
28. Woo, K. V. *et al.* Tie1 attenuation reduces murine atherosclerosis in a dose-dependent and shear stress-specific manner. *J. Clin. Invest.* **121,** 1624–1635 (2011).
29. Mack, J. J. *et al.* NOTCH1 is a mechanosensor in adult arteries. *Nat. Commun.* **8,** 1620 (2017).
30. Li, S. *et al.* Fluid Shear Stress Activation of Focal Adhesion Kinase LINKING TO MITOGEN-ACTIVATED PROTEIN KINASES. *J. Biol. Chem.* **272,** 30455–30462 (1997).
31. Jo, H. *et al.* Differential Effect of Shear Stress on Extracellular Signal-regulated Kinase and N-terminal Jun Kinase in Endothelial Cells Gi2- AND Gβ/γ-DEPENDENT SIGNALING PATHWAYS. *J. Biol. Chem.* **272,** 1395–1401 (1997).
32. Mengistu, M., Brotzman, H., Ghadiali, S. & Lowe-Krentz, L. Fluid shear stress-induced JNK activity leads to actin remodeling for cell alignment. *J. Cell. Physiol.* **226,** 110–121 (2011).
33. Zheng, L. *et al.* Fluid shear stress regulates metalloproteinase-1 and 2 in human periodontal ligament cells: involvement of extracellular signal-regulated kinase (ERK) and P38 signaling pathways. *J. Biomech.* **45,** 2368–2375 (2012).
34. Hsieh, H.-J., Liu, C.-A., Huang, B., Tseng, A. H. & Wang, D. L. Shear-induced endothelial mechanotransduction: the interplay between reactive oxygen species (ROS) and nitric oxide (NO) and the pathophysiological implications. *J. Biomed. Sci.* **21,** 3 (2014).
35. Zhao, Y., Vanhoutte, P. M. & Leung, S. W. S. Vascular nitric oxide: Beyond eNOS. *J. Pharmacol. Sci.* **129,** 83–94 (2015).
36. Conway, D. E. & Schwartz, M. A. Flow-dependent cellular mechanotransduction in atherosclerosis. *J. Cell Sci.* **126,** 5101–5109 (2013).
37. Lane, W. O. *et al.* Parallel-plate Flow Chamber and Continuous Flow Circuit to Evaluate Endothelial Progenitor Cells under Laminar Flow Shear Stress. *J. Vis. Exp. JoVE* (2012). doi:10.3791/3349
38. Franzoni, M. *et al.* Design of a cone-and-plate device for controlled realistic shear stress stimulation on endothelial cell monolayers. *Cytotechnology* **68,** 1885–1896 (2016).
39. Han, H.-C. Twisted Blood Vessels: Symptoms, Etiology and Biomechanical Mechanisms. *J. Vasc. Res.* **49,** 185–197 (2012).
40. Tyser, R. C. *et al.* Calcium handling precedes cardiac differentiation to initiate the first heartbeat. *eLife* **5,** e17113 (2016).
41. Schleich, J.-M., Abdulla, T., Summers, R. & Houyel, L. An overview of cardiac morphogenesis. *Arch. Cardiovasc. Dis.* **106,** 612–623 (2013).
42. Bruneau, B. G. Signaling and Transcriptional Networks in Heart Development and Regeneration. *Cold Spring Harb. Perspect. Biol.* **5,** a008292 (2013).
43. Parodi, E. M. & Kuhn, B. Signalling between microvascular endothelium and cardiomyocytes through neuregulin. *Cardiovasc. Res.* **102,** 194–204 (2014).
44. Gitler, A. D. *et al.* *Nf1* has an essential role in endothelial cells. *Nat. Genet.* **33,** 75–79 (2003).

45. Van den Akker, N. M. S. *et al.* PDGF-B signaling is important for murine cardiac development: Its role in developing atrioventricular valves, coronaries, and cardiac innervation. *Dev. Dyn.* **237,** 494–503 (2008).

46. Andrés-Delgado, L. & Mercader, N. Interplay between cardiac function and heart development. *Biochim. Biophys. Acta* **1863,** 1707–16 (2016).

47. Malek, A. M., Gibbons, G. H., Dzau, V. J. & Izumo, S. Fluid shear stress differentially modulates expression of genes encoding basic fibroblast growth factor and platelet-derived growth factor B chain in vascular endothelium. *J. Clin. Invest.* **92,** 2013–2021 (1993).

48. Yamazaki, T. *et al.* Endothelin-1 Is Involved in Mechanical Stress-induced Cardiomyocyte Hypertrophy. *J. Biol. Chem.* **271,** 3221–3228 (1996).

49. Rich, S. & McLaughlin, V. V. Endothelin Receptor Blockers in Cardiovascular Disease. *Circulation* **108,** 2184–2190 (2003).

50. Nikolova-Krstevski, V. *et al.* Endocardial TRPC-6 Channels Act as Atrial Mechanosensors and Load-Dependent Modulators of Endocardial/Myocardial Cross-Talk. *JACC Basic Transl. Sci.* **2,** 575–590 (2017).

51. Nadeau, M. *et al.* An endocardial pathway involving Tbx5, Gata4, and Nos3 required for atrial septum formation. *Proc. Natl. Acad. Sci. U. S. A.* **107,** 19356–19361 (2010).

52. Lee, T. C., Zhao, Y. D., Courtman, D. W. & Stewart, D. J. Abnormal aortic valve development in mice lacking endothelial nitric oxide synthase. *Circulation* **101,** 2345–2348 (2000).

53. Lee, J. S. *et al.* Klf2 is an essential regulator of vascular hemodynamic forces in vivo. *Dev. Cell* **11,** 845–857 (2006).

3. Chapter 3: Engineering vessels with 3D curvature

3.1 3D curvature-instructed endothelial flow response and tissue vascularization

3.1.1 Abstract

Vascularization remains a long-standing challenge in engineering complex tissues, particularly in recapitulating 3D vascular features found in vivo, including continuous changes to diameter, curvature and torsion. Here, we developed a new spiral microvessel model that allows for precise control of curvature and torsion and supports homogeneous tissue perfusion at the centimeter scale. Using this system, we showed proof-of-principle modeling of tumor progression and engineered cardiac tissue vascularization. We demonstrated that 3D-curvature induced rotation and mixing under laminar flow, leading to unique phenotypic and transcriptional changes in endothelial cells (ECs). Bulk and single-cell RNAseq identified specific EC gene clusters in spiral microvessels, marking a pro-inflammatory phenotype associated with vascular development and remodeling, and a unique cell cluster expressing genes regulating vascular stability and development. Our results shed light on the role of heterogeneous vascular structures in differential development and pathogenesis and provide new tools to potentially improve tissue vascularization and regeneration.

3.1.2 Introduction

The human vasculature forms a complex three-dimensional (3D) architecture spanning a large range of diameter, curvature, and torsion in order to provide efficient perfusion and tissue oxygenation. Its structure continues to adapt and remodel throughout life to meet changing energy demands in both regeneration and disease progression. The sources of vascular remodeling, however, remain elusive, partially due to the complex and heterogeneous vascular structure found in vivo and the lack of tools to recapitulate them in vitro. Vascularization remains a critical challenge in engineering complex tissue for potential tissue repair and disease modeling.[1,2]

Hemodynamic forces have been identified as one major driver of vascular development and remodeling.[3,4] By sensing the forces of blood flow, endothelial cells (ECs) lining the blood vessel wall regulate their morphology, phenotype, and cell behavior, and further modify the structure of the vascular wall and vascular networks to support tissue growth.[5–7] Extensive efforts have been made in understanding EC response to flow using flow chambers and microfluidic channels, [8,9] through which the EC response has been binned into one of two categories: laminar or disturbed. [6,10,11] Laminar flow, defined as the parallel flow in devices such as parallel plate flow chambers, cone and plate viscometers, and straight tubes, applies uniform shear stress on ECs, which promote ECs alignment along the direction of flow and EC quiescence and maturation.[12–14] Disturbed flow on the other hand has been described by distinct hemodynamic features like flow separation, flow reversal, or recirculation, and modeled in step flow devices or specific pathological large vessel models *in vitro.*[6,10] Locations of disturbed flow are often associated with hot-spots for atherosclerotic plaques in vivo, like in the aortic arch or at the bifurcations of vessels branching off the aorta.[15–17]

This dichotomous view of the endothelial response to flow has led to significant advances in our understanding of EC biology, mechanotransduction and vascular pathologies. [7,10,18] Perfect axial flows and highly disturbed flows, however, represent the two extremes of a wide spectrum of flow profiles found throughout the vasculature. They do not reflect the extensive range of flow characteristics in the blood vessels that bend and twist through 3D space with varying levels of curvature and torsion (i.e. the deviation of curvature from its osculating plane).[18–22] For example, an analysis of vessels in the human cerebral cortex found that more than 50% of arterioles and venules had high curvature ($k = 1/R$, $k > 0.1\ \mu m^{-1}$).[23]

Heterogeneous vascular remodeling[18,19,24,25] has been found in small vessels *in vivo* with low flow but high curvature and torsion.

The flow profile of curved vessels was first described by W.R. Dean, who found that curvature modifies the flow by introducing a secondary flow orthogonal to primary flow axis, known as Dean flow. To characterize this phenomena the Dean number (De) was defined, combining the Reynolds number ($Re = \frac{\rho UD}{\mu}$, U = velocity, D = diameter, ρ = density, and μ = viscosity) with measures of the vessel's curvature ($De = Re\sqrt{\frac{D}{2R_c}}$, D = diameter, R_c = Radius of curvature of the channel path). Additional research has extended Dean flows into 3D space and demonstrated theoretically that out of plane torsion modifies the secondary flow and also adds rotation into the primary flow at low Re ($Re \leq 1$).[26–28] In these curved vessels, ECs would experience not only the laminar shear force in the longitudinal direction, but also curvature dependent centrifugal and Coriolis forces and torsion dependent forces that can be at normal, binormal (circumferential) or tangential (longitudinal) directions to the axial flow.[29,30] It is not known how these complexities contribute to EC responses to flow, particularly in widespread small vessels.

This gap in the literature can be attributed to the difficulty of studying vessels with defined diameter, curvature and torsion. Small curved vessels *in vivo* are often hard to image and measure flow, highly variable in geometry, and difficult to isolate for the study of cellular structure, function and gene expression. In vitro, methods for engineering small vessels with 3D continuous curvature are limited. Microfluidic designs are typically confined to a single plane with zero torsion.[31] Recent advances in bioprinting have made it possible to fabricate constant curvature conduits with torsion in biocompatible materials, but small vessel diameters are difficult to achieve and printing artifacts (e.g., layer lines) alter the shape of flow.[32,33] A new method enabling the rapid fabrication of vessels with controllable diameter, curvature and torsion would help fill this gap in understanding of the heterogenous EC flow response and guide the design of vascularization in regenerative medicine.

Here we have addressed these challenges by developing a spiral microvessel system with robust endothelium along the lumen, and precisely controlled diameter, curvature and torsion in 3D space. We showed the spiral vessels supported rapid vascularization and homogeneous perfusion of thick (> 5 mm) engineered tumor models and cardiac constructs. We show for the first time that small vessels with constant curvature and torsion in laminar flow regimes induced distinct changes in endothelial cell phenotype and transcriptional profiles compared to straight vessels. Our results shed light on the role of vascular geometry in the heterogeneous vascular response to flow and show the promise of an easy-to-fabricate 3D platform for investigating the effect of curvature and torsion on vascular biology.

3.1.3 Methods

Fabrication of endothelialized spiral vessels in PDMS

Spiral polydimethylsulfoxone (PDMS) devices were formed by casting a mixture of Sylgard 184 (10:1 base:curing agent) around springs of varying pitch, wire diameter, and spiral diameter. The mixture was cured at 60 ºC for 2 – 3 hours and the spring was removed from the polymerized PDMS. Prior to seeding cells, PDMS spiral devices were exposed to oxygen plasma for ~90 s and then immediately incubated with a 0.1% gelatin solution at 37 ºC for 20 minutes. Human umbilical vein endothelial cells (HUVEC) were trypsinized and resuspended to 10-12 million cells/mL. Spiral vessels were seeded by perfusion of 20-40 µL of this suspension at 20 µL/min. Devices were rotated every 15 minutes for one hour to ensure even coverage of seeded cells on the vessel wall. Vessels were subject to constant flow perfusion between 4 and 12 hours post-seeding. Unless noted otherwise, PDMS vessels were cultured under 1 µL/min flow, driven by syringe pump (KD Scientific KDS 220) with EGM supplemented with 3.5% dextran.

Design and fabrication of spiral retractor system

An automated retraction device was designed to reproducibly create spiral features in crosslinked hydrogels. A custom 2-axis machine was fabricated from a combination of 3D-printed and machined components. Linear motion in ±Z and rotation about Z were controlled through two stepper motors connected to an Arduino microcontroller. The microcontroller was programmed to "unscrew" a spring from a crosslinked hydrogel when given the spring pitch (mm/turn) as an input. This controlled movement is independent of the other features of the spring (i.e. wire diameter, spring diameter). While a purely mechanical device can be fabricated to accomplish the same task, it would require a unique set of components for every spring pitch of interest.

A set of spiral vessel holders were also designed and milled out of polysulfone. Each holder consisted of a small rectangular reservoir (~10 mm x 5 mm x 5 mm) where the spiral vessel was formed in collagen gel. For visualization, two of the walls of this reservoir were formed by using PDMS to bond glass microscope coverslips to the polysulfone device. To connect spirals to a perfusion system, a hole was drilled in the side of each holder to provide a slip-fit interface for connecting 23-gauge hypodermic tubing.

Fabrication of endothelialized straight round vessels in PDMS

Straight round vessels in PDMS were formed by suspending lengths of 28-gauge stainless steel hypodermic tube in a custom-machined acrylic mold. PDMS was poured over this mold and cured as for spiral PDMS devices. The hypodermic tubing was removed from the cured PDMS, leaving round straight channels in PDMS with a single inlet per channel and an outlet that drained into the tissue culture dish. Prior to seeding cells, round straight PDMS devices were exposed to oxygen plasma for ~30 s and then immediately incubated with a 0.1% gelatin solution at 37 ºC for 20 minutes. HUVEC were seeded into this lumen via perfusion as described in spiral PDMS devices.

Fabrication of endothelialized spiral vessels in collagen

Collagen gels were prepared by mixing an acidic collagen stock solution (at 15 mg/mL) with 1N NaOH, 10X Medium M199, and endothelial growth media (Lonza) to reach neutralization and targeted concentration (6 mg/mL or 7.5 mg/mL). After homogenizing, the collagen mixture was degassed by placing under vacuum for 30-60 minutes. While the gel solution was under vacuum, spiral vessel holders were prepped by brief corona treatment (< 30 s) and subsequent coating of polyethylenimine (PEI, 1%, Sigma) with glutaraldehyde (0.1%, Sigma) crosslinking. After five washes with autoclaved water, vessel holders were dried and placed in the spiral retractor system where the spiral pattern was brought into contact with a 1-inch length of 23-gauge hypodermic tubing within the holder. The degassed gel mixture was then pipetted into the reservoir and allowed to crosslink at room temperature for 1 hour. After crosslinking, the spiral pattern was removed from the gel using the spiral retraction system and submerged in warm media. Each spiral vessel was seeded with cells following the same protocol as in PDMS vessels.

Fabrication of combination microvessel-spiral vessel devices in collagen

Planar vascular networks in collagen were formed by modification of a previously described protocol.[34] Briefly, microvessels are fabricated by sandwiching a bottom flat layer of collagen gel with an injection molded top layer of collagen gel bearing a microfabricated vessel pattern. To form combination vessels, the spiral pattern was introduced during the molding step for the top layer of collagen and the spiral vessel connected directly to the microfabricated pattern. Microvessels were otherwise assembled normally and devices were seeded by gravity perfusion of a cell suspension from the top of the spiral vessel. Devices were cultured under gravity driven flow (~6 mm H_2O pressure head) that was replenished every 12 hours.

Anastomosis of spiral vessels with self-assembled connective vascular tubes in collagen

The spiral microvessels were formed following the same general protocol as collagen spiral vessels described above, but with the addition of endothelial cells within the bulk matrix. Collagen gel was prepared and degassed, followed by the addition of HUVECs into the gel to reach a final concentration of 2.5 million cells/mL in 7.5 mg/mL collagen. The mixture was then added into spiral vessel holders for thermal gelation. Additional HUVECs were then seeded into the lumen of spiral vessels as described above in other devices. The culture was then maintained under gravity driven flow (~6 mm H_2O pressure head) and replenished every 12 hours.

Fabrication of tumor spiral vessels to support tumor angiogenesis in collagen

An 18-gauge needle was added to the center of the spiral pattern before gelation of collagen gel to form tumor spiral vessels. After gelation at 37 ºC for 30 min, both the spiral and the 18-gauge needle were retracted simultaneously, leaving a spiral vessel as well as an open center channel for the final collagen structure. A separate 6 mg/mL collagen gel was prepared with a suspension of KG1a cancer cells (final concentration 5 million cells/mL). This KG1a-collagen gel was then pipetted into the central space in the collagen spiral device and polymerized at 37 ºC for 30 minutes. After this second step of polymerization, the spiral vessel was seeded with

HUVEC as described previously and cultured under 1 μL/min flow with EGM supplemented with 3.5% dextran for up to 7 days.

Fabrication of thick cardiac tissue perfused with spiral vessels (cardiac spirals) in collagen

Cardiac spirals were formed using the same spiral and 18-gauge needle pattern as tumor spirals described as above. The collagen cell-gel mixture (6 mg/mL) for these devices consisted of human embryonic stem cell (hESC)-derived cardiomyocytes (20 million cells/mL), HS27a stromal cells (10 million cells/mL), and HUVEC (2 million cells/mL).[35] Transgenic RUES2 hESC expressing the fluorescent calcium reporter GCaMP3 were differentiated into cardiomyocytes by modulation of activin A, BMP4, and Wnt signaling using a previously reported protocol.[36] The void space in the center of these devices was left unfilled, but seeded with HUVEC in the process of seeding the spiral vessel lumen.

Computational fluid dynamic analysis in spiral vessels compared to straight vessels

The fluid flow characteristics in the three-dimensional straight tubes and spiral tubes were simulated with COMSOL Multiphysics software, package ver. 5.0. The Navier-Stokes equation was used as pre-defined in COMSOL and solved with the stationary solver for laminar flow. The fluid properties were defined as follows: viscosity of 3×10^{-3} Pa s (mimicking that of endothelial growth media with 3% 70kDa dextran), and density of 3×10^{-3} kg/m^3. The inlet boundary conditions are laminar flow with constant flow rate at Q = 1, 50, or 100 μL/min, corresponding to the average inlet velocity at 0.14, 7, and 14 mm/s, and the outlet boundary conditions are laminar flow with zero pressure. The channel walls were set to no-slip boundary condition. We decreased the length of the modeled channel (~ 40 mm, and 6.5 loops) to enhance computation speed. Approximately 3×10^5 mesh elements were used in each simulation, and the simulation results were demonstrated mesh-independent when change mesh size. The average secondary flow velocity was calculated as the velocity at the direction orthogonal to the primary flow direction. The primary flow, secondary flow velocity and shear rate were exhibited at the cross-sectional plane that is orthogonal to the primary flow direction.

Immunofluorescent staining and imaging

Spiral and straight vessels, after culture for designated time, were fixed by treatment with 4 % formaldehyde for 15 mins (for PDMS devices) or 60 mins (for collagen devices). Devices were permeabilized by incubation in PBS containing Triton X-100 (0.5 %) and bovine serum albumin (BSA, 2%) for 30 minutes. Unconjugated primary antibodies were added into the spirals (and onto collagen gels), incubated overnight at 4 ºC, followed by washing with PBS for three times 5 mins for each time), and incubation with secondary antibodies and Hoescht 33342 (40 µg/mL) for 1 hour at room temperature before a final round of washing. Devices were stained for factors including CD31 (Abcam ab28364, 1:30), VE-CAD (Abcam ab33168, 1:100), von Willebrand Factor (Abcam ab8822, 1:100), cTnT (Thermo Fisher MS-295-P1, 1:100), and F-actin (Thermo Fisher A12379, 1:100). Stained devices were imaged using a Nikon A1R confocal microscope or a Yokogawa W1 spinning disk confocal system.

RNA-Seq

For RNA-Seq studies, PDMS spirals, PDMS round straight channels, PDMS square straight channels, and collagen spiral devices were used. All PDMS devices were fabricated to have either a 400 µm lumen diameter or 400 µm square cross-section and equal total vessel length (~68 mm). All devices were perfused at either 1 µL/min (“Low”) or 50 µL/min (“High”) for 3 days. On day 3, vessels were perfused with RLT lysis buffer and the lysate collected. For PDMS devices, 350 μL RLT was perfused per device and RNA was isolated using a RNeasy Mini Kit (Qiagen). For collagen spirals, 175 μL RLT was perfused per device. Prior to RNA isolation, the lysate from two collagen spirals was pooled to form one sample replicate.

Isolated RNA samples were then processed for RNA sequencing (Illumina NGS, Paired End 50 cycles, Low-input library prep). RNA sequencing data was aligned using TopHat to hg38.[37] Aligned count data was normalized and evaluated using EdgeR[38] where genes with adjusted p-values and false discovery rates less than 0.05 and log(fold change) ≥ 0.585 were considered differentially expressed. Gene set enrichment analysis was performed using Enrichr[39] and clusterProfiler[40] to probe KEGG,[41] WikiPathways,[42] and Gene Ontology[43] gene-set libraries. Ingenuity Pathway Analysis (Qiagen) was also used to probe for upstream regulators of differentially expressed genes.

Single cell RNA-seq

For single cell RNA-seq (scRNA-seq) studies, spiral or straight vessels containing ECs were perfused under high flow conditions (50 μL/min). ECs were harvested from 3-4 vessels of each geometry by trypsinization and pooled. Cells were washed with PBS and re-suspended in 0.04% ultrapure BSA (ThermoFisher, Scientific) in PBS on ice. Approximately 3500 cells were loaded on the 10X Genomics Chromium platform in one lane per sample. The 10X Genomics Version 2 single cell 3’ kit was used to prepare single cell mRNA libraries. Sequencing was performed for pooled libraries from each sample on an Illumina NextSeq 500 using the 75 cycle, high output kit. The Cell Ranger 2.1.1 pipeline (10X Genomics) was used to determine cell barcodes and UMIs per cell, and to exclude low-quality cells, using default parameters. The Monocle (v.2.99.3) platform [44] was used for downstream analysis of scRNA-seq data, combining read-depth normalized data from spiral and straight vessel samples. Dimensionality reduction with Uniform Manifold Approximation (UMAP) [45] was used to project cells in three dimensions, using the top 20 principle components, with the reduceDimension function (reduction_method = 'UMAP', max_components = 3). Clustering was performed by louvain method with the clusterCells function, using default parameters with the exception of resolution set to 8e-4. The principalGraphTest and differentialGeneTest functions in Monocle were used to determine genes differentially expressed between clusters in the UMAP projection and between ECs in spiral versus straight vessel geometries, respectively, selecting genes based on specificity and expression level (for cluster-specific genes), and significance ($q<0.01$) (for genes differentially expressed between samples).

3.1.4 Results

Fabrication and endothelialization of spiral tubes in PDMS and collagen gels

We exploited subtractive molding techniques to fabricate spiral tubes in both polydimethylsiloxane (PDMS) and collagen hydrogels and tested the fabrication limit and fidelity. In PDMS, stainless-steel springs of various dimensions were molded in liquid phase PDMS (10:1 base:curing agent) and manually removed after crosslinking. Robust perfusable spiral tubes with constant curvature were generated in PDMS with diameter larger than 200 μm and pitch greater than 1 mm/turn. The fabrication of smaller spiral tubes in PDMS is less consistent due to the distortion of the channel structure during spring removal. In collagen hydrogels (6 – 7.5 mg/mL), an automatic 2-axis motion system was designed to retract the spring from the hydrogel after thermal gelation. Automatic retraction was critical to minimize distortion of the spiral pattern and maximize continuity of the luminal geometry in three dimensions in soft matrices (Figure 3.1.1A). Spiral tubes of a wide range of wire diameter (d_w = 120 – 400 μm), spiral diameter (d_s = 1 – 3 mm), and pitch ($p \geq 400$ μm) were formed in collagen hydrogels, corresponding to curvature κ in the range of 0.43 – 1.05 mm^{-1} and torsion τ in the range of 0.32

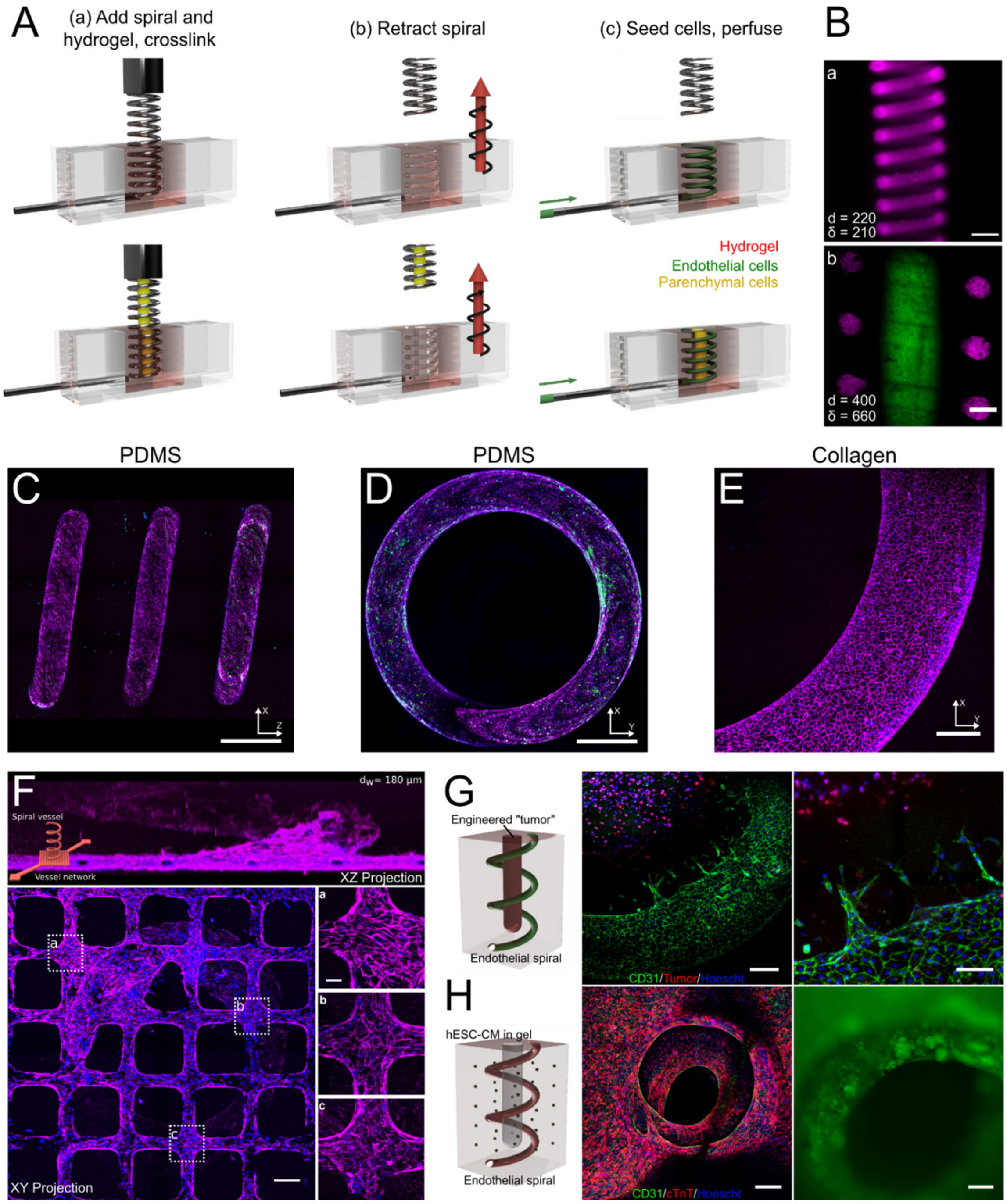

Figure 3.1.1 Spiral vessel fabrication and engineered tissue models. A. Schematic of spiral vessel fabrication strategy: Upper panels: a hydrogel is crosslinked around an off-the-shelf spring (a), the pattern is retracted from the gel via a 2-axis motion system (b) and vessels were seeded with cells by perfusion (c). Lower panels: an independent rod was introduced at the center of the spring to form additional lumen for independent access and cell seeding. **B**. a – Maximum intensity projection (MIP) of a confocal z-stack of a spiral vessel in collagen perfused with fluorescent beads. b – Optical section of a collagen spiral vessel (magenta) with an independently perfused center channel (green). Scale bar: 500 μm **C-E**. MIP of side (C) and top (D) views of an endothelialized spiral vessel in PDMS and top view of endothelialized collagen vessel (E). Scale bars: 750 μm, 600 μm, 150 μm. **F**. Integrated fabrication of spiral vessel (z directional flow) and planar microvessel (x and y directional flow) showing MIP of side and top views with magnified views of regions near (a) and distant from the connection of spiral to planar microvessels (b, c). Magenta, CD31; green, von Willebrand Factor; blue, nuclei. Scale bar: 200 μm, inset 50 μm **G**. Engineered vascularized tumor model with endothelial cells from the spiral vessel sprouting towards avascular tumor cells embedded in the center lumen of the spiral. Green, CD31; red, KG1a cancer cells; blue, nuclei. Scale bar: 200 μm (left), 100 μm (right) **H**. Vascularized cardiac chamber model. Green, CD31; red, cTnT; blue, nuclei. Scale bar: 500 μm.

– 0.72 mm^{-1} (Appendix A, Figure A1A). Fluorescent beads were perfused to visualize the 3D structure of the spiral lumen (Figure 3.1.1B(a), A1A, B, Movie A1), where loops of the spiral tubes were periodically spaced with distinct boundaries. Using off-the-shelf springs, we were able to achieve spacing between loops ($\delta = p - d_w$) as small as 210 µm. We further modified the spiral mold by adding a cylinder in the center of the spring to generate a second independently perfusable lumen in the hydrogel structure (Figure 3.1.1B(b)). We fabricated constructs with a central tube concentrically wrapped with a spiral tube and separated by a wall as thin as 200 µm.

Next, we perfused human umbilical vein endothelial cells (HUVEC) into the spiral tubes in either PDMS or collagen to allow for cell attachment followed by culture under flow. Both materials supported the growth of a robust endothelium under steady flow for at least one week (Q = 1 µL/min, Figure 3.1.1C-E). PDMS spiral vessels with a lumen diameter less than 200 µm often had sparse coverage of endothelial cells on the vessel surface after seeding and were not used in experimental conditions. Collagen spiral vessels better supported endothelialization and HUVECs were seeded and cultured under similar flow conditions for spiral vessels as small as 180 µm with high reproducibility (Figure A1C). Endothelial cells in PDMS vessels (lumen diameter > 200 µm) and all sized collagen vessels had robust junctions at cell-cell contacts, and localized expression of CD31 to the plasma membrane (Figure 3.1.1C-E). Altogether, we successfully generated spiral microvessels with constant curvature and torsion at high fidelity and reproducibility and with robust endothelialization and perfusion.

Spiral vessels enhanced 3D vascularization

The fabrication process for spiral vessels has the flexibility to integrate with existing vascularization approaches to further enhance tissue perfusion. By incorporating endothelial cells into the bulk matrix, the endothelium in spiral tubes readily anastomosed with self-assembled vessel networks and increased vascular density (Figure A1D). When combined with lithography and injection molding techniques,[34] we successfully connected a spiral vessel with a microfabricated rectilinear vessel so that the spiral outflow was connected to the perfusion of microvessels in an orthogonal direction to the spiral. This integration allows for the rotation of the spiral flow direction into another plane and mimics the architecture of the spiral artery to vascular bed connection found in vivo (Figure 3.1.1F). We observed a continuous endothelium in the spiral-microvessel connection (Figure 3.1.1F(a)). ECs in the planar microvessels near the spiral vessel outflow showed greater alignment with the direction of flow, likely due to higher flow stresses, (Figure 3.1.1F(a), average angle 13.5 ± 10.2) compared to cells in regions distant from the spiral-microvessel interface (Figure 3.1.1F(b,c) average angle 39.3 ± 23.7 and 58.13 ± 29.25 respectively). These findings show the high potential of spiral vessels as a new strategy to enhance perfusion and support thick tissue vascularization.

Using the concentric spiral platform in collagen gel, we further demonstrated the potential of spiral vessels in supporting 3D tissue function. By dispensing tumor cells (KG1a, a leukemia cell line, Methods) in a collagen gel (6 mg/mL) into the spatially defined center cylinder (1.3 mm diameter), we formed an artificial tumor surrounded by spiral vessels and monitored the sprouting of vessels from the spiral. Cultured under flow ($Q = 1$ µL/min) in normal growth media, spiral vessels ($d_w = 400$ µm, $d_s = 3.0$ mm, $p = 1$ mm) maintained patency throughout 7 days of culture, and sprouted consistently by day 7, but not at day 3 ($N = 4$ for each time point) (Figure 3.1.1G). These sprouts extended exclusively towards the tumor, with sprouts reaching as far as 220 µm from the vessel wall by day 7. No sprouts were observed when there were no tumor cells in the center.

We also created a thick vascularized cardiac chamber by using the same concentric model (1.3 mm diameter x 6 mm long chamber surrounded by spiral vessel). GCaMP3-transduced human embryonic stem cell derived cardiomyocytes (hESC-CM) and stromal cells (HS27a) were added into the bulk collagen matrix,[35] and endothelial cells (HUVEC) into both the bulk matrix and in the spiral lumen, while the center of the tissue was kept open (Figure 3.1.1H). By day 12 of culture, organized calcium waves were observed and appeared to propagate in 3 dimensions along the spiral vessel wall (Supplemental Movie S2). The conduction velocity in engineered cardiac tissues was 2.7 ± 0.97 cm/s as determined by analysis of the GCaMP3 signal (Figure A2).

These approaches show in proof-of-concept that the spiral vessel platform can be used to support 3D vascularization and perfusion in large tissues, to study the vascular-tissue interaction in a spatially and temporally controlled manner, and to model complex tissue functions.

Flow characteristics of spiral tubes

We next examined the flow characteristics in these spiral microvessels and compared them with straight vessels of the same caliber. We visualized the flow characteristics by perfusing fluorescent bead solutions in two parallel streams through straight and spiral PDMS vessels of the same diameter and length ($d_{vessel} = 400\ \mu m$, $d_{spiral} = 3$ mm, $p_{spiral} = 1$ mm, $\kappa_{spiral} = 0.46\ mm^{-1}$, $\tau_{spiral} = 0.31\ mm^{-1}$, and L = 6.5 cm) at three steady flow conditions (Q = 1, 50, and 100 µL/min, corresponding to Re = 0.01, 0.76, and 1.52 respectively). The 3-D flow images were taken under confocal fluorescence microscopy at set distances (L_v = 5, 30, and 55 mm in straight vessels, or loop ¾, 3¾ and 6¾ in spiral vessels) from the vessel inlet. Straight tubes displayed a classical parallel flow profile where the two streams of beads traveled to the outlet and maintained their position over the whole vessel length at both flow rates (Figure 3.1.2A, C). In spiral tubes the two beads streams remained distinct and parallel at low flow (Q = 1 µL/min) but

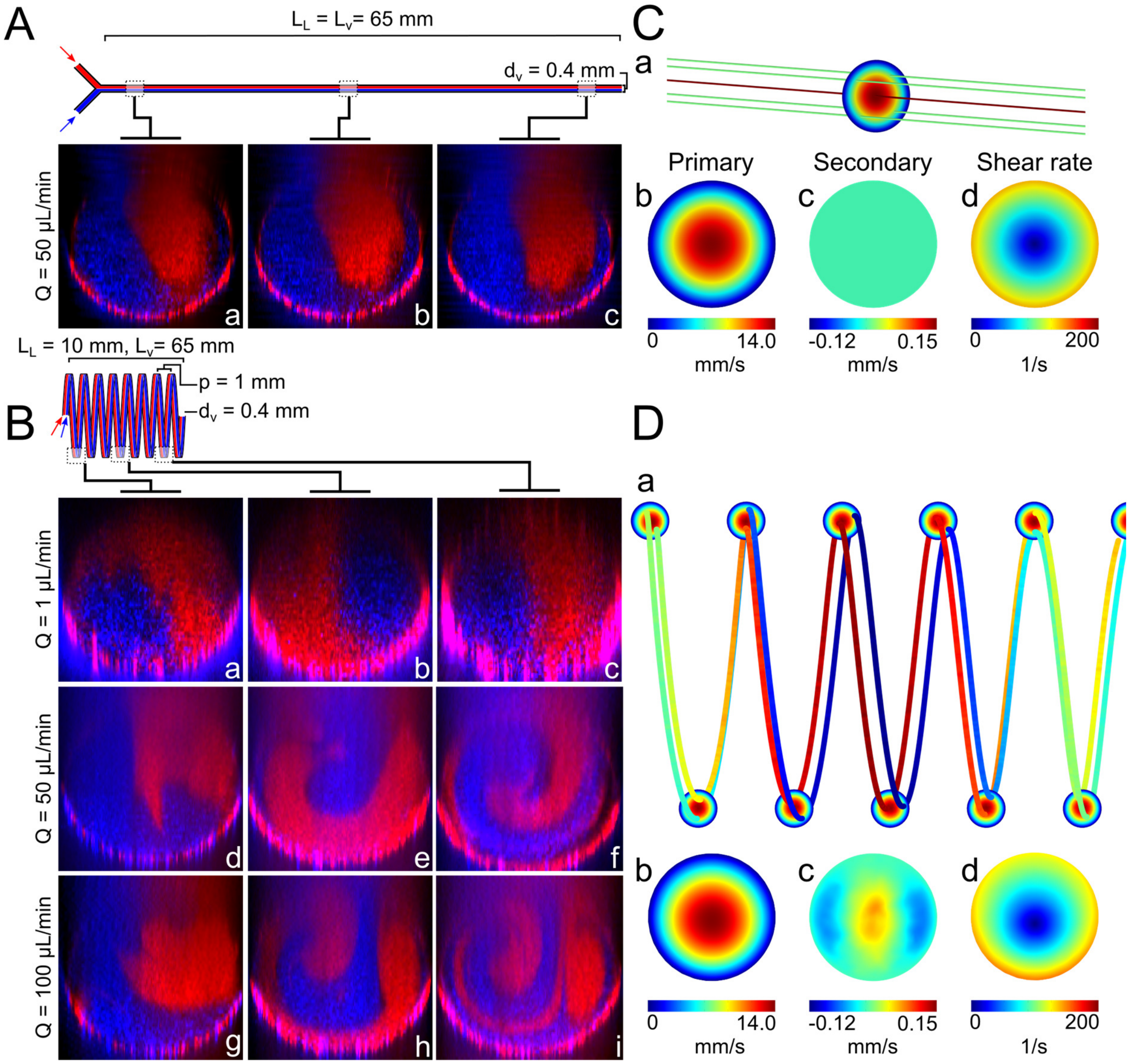

Figure 3.1.2 Flow in straight and spiral vessels. A-B. Confocal cross-sections of perfusion of two parallel streams of red and blue beads into a straight PDMS vessel (A) at a flow rate of Q = 50 µL/min and a spiral PDMS vessel (B) at three flow rates (Q = 1, 50, 100 µL/min) at 3 distances from the vessel inlet ($\Delta L_{v,a} \approx 5$ mm, $\Delta L_{v,b} \approx 30$ mm, $\Delta L_{v,c} \approx 55$ mm), corresponding to the ¾, 3¾ and 6¾ spiral loops. (L_L = Linear length, L_v = Vessel length, d_v = Vessel diameter, p = pitch). **C-D.** Computational fluid dynamics plots of straight (C) and spiral (D) vessels at Q = 50 µL/min for (a) streamlines (color expressed with primary velocity magnitude), (b) primary velocity magnitude, (c) secondary flow velocity orthogonal to cross-sectional plane, and (d) shear rate at the cross-sectional views.

rotated over the vessel length without obvious mixing in the bulk (Figure 3.1.2B(a-c)). The orientation of the two parallel streams inverted after approximately 4 loops from the inlet (Figure 3.1.2B(b)) and completed a full rotation at approximately loop 7 (Figure 3.1.2B(c)). At a higher flow rate (Q = 50 μL/min) in the same spiral geometry (De = 2.77), the two beads stream developed obvious bulk mixing with the leading edge of flow rotating 270 degree after 3 loops (Figure 3.1.2B(e)), and completed another full rotation by loop 7 (Figure 3.1.2B(f)). At even higher flow (Q = 100 μL/min), a stronger mixing effect was observed in the same spiral geometry (Figure 3.1.2B(g-i)), whereas the two streams remained parallel and unmixed in straight vessels under the same flow conditions.

Using numerical simulation with COMSOL, we confirmed these flow characteristics: 1) idealized parallel streamlines were present in fully-developed flow in straight vessels (Figure 3.1.2C(a)); 2) parallel streamlines in spiral vessels slightly rotate along circumferential direction at low flow (Q = 1 μL/min, Figure A3A); 3) streamline rotation was enhanced in spiral vessels and developed twists at higher flow (Q = 50 μL/min, Figure 3.1.2D(a)) and had clear twists at Q = 100 μL/min (Figure A3B). The spiral geometry did not induce a significant change in the primary flow compared to straight vessels, but did lead to the emergence of secondary flows with a peak magnitude of around 1% of the primary flow velocity (Q = 50 μL/min, Figure 3.1.2C(b,c), D(b,c)). This also led to the development of a shear stress gradient in 3D space and a change in the wall shear stress (WSS), with a maximum (10% increase over the straight tube) on the surface of the inner curvature and minimum on the outer bend, unlike in a straight tube where the WSS was constant across the lumen cross section with zero gradients (Figure 3.1.2C(d), D(d)). These data demonstrated that spiral vessels induced bulk flow mixing and heterogeneous hemodynamic forces on the endothelium lining the wall due to 3D curvature and torsion.

3D curvature alters endothelial morphology and mRNA expression under flow

To understand how the distinct hemodynamic features of flow in spiral vessels affected ECs, we cultured cells in both geometries under flow. In straight and spiral vessels ECs formed robust junctions and a stable endothelium in low (Q = 1 μL/min, WSS = 0.1 dyne/cm^2 in straight

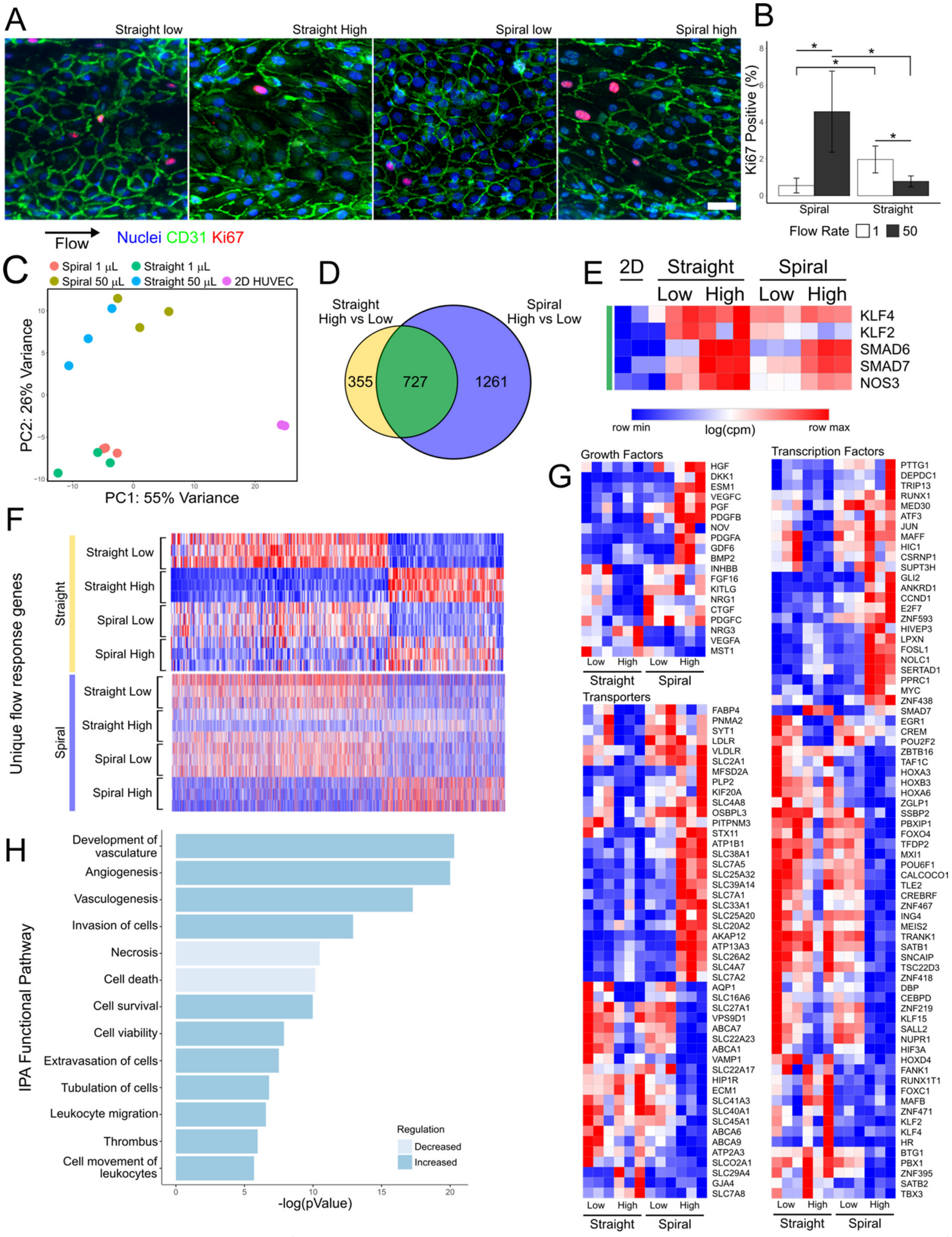

Figure 3.1.3 Endothelial response to flow in straight and spiral vessels. A. Maximum intensity projection (MIP) of EC cultured under flow (Q = 50 μL/min) for 24 hours. Blue, nuclei; green CD31; Ki67, red; scale bar = 50 μm. **B**. Quantification of the percentage of Ki67 positive nuclei by counting 100+ cells per vessel in N = 3 vessels at two flow conditions (Q = 1 and 50 μL/min). Error bars represent 95% confidence interval of the mean. * p < 0 .05 using a one-way ANOVA with Tukey's pairwise comparisons. **C**. Principle component analysis of RNA sequencing data from cells cultured at static and at two flow conditions in two vessel geometries (N = 3). **D**. Venn diagram showing the overlap of genes significantly changed by increasing flow in straight and spiral geometries. **E**. Heatmap of log counts per million (CPM) values of known flow-responsive genes. All genes are present in the overlapping region of (D, green). **F**. Heatmaps of the CPM values of significantly regulated transcripts belonging to the non-overlapping regions of (D). 355 genes uniquely regulated in straight high vs low (upper, yellow), and 1261 genes uniquely regulated in spiral high vs low (lower, blue). **G**. Heatmaps of the CPM values of selected growth factors, transporters, and transcription factors. **H**. IPA functional pathways identified by comparing spiral to straight vessels under high flow.

vessels) and high ($Q = 50$ µL/min, $WSS = 4.6$ dyne/cm^2 in straight vessels) flow conditions. The increased flow appeared to change the EC morphology and enhance EC alignment in the direction of flow (Figure 3.1.3A). Under low flow conditions ($Q = 1$ µL/min, Figure 3.1.3B) fewer Ki67$^+$ proliferating cells were observed in spiral vessels than in straight vessels. When exposed to higher flow, however, more proliferating cells were observed in the spiral geometry than the straight geometry suggesting distinct roles for geometry and flow on the endothelial cells.

We next examined the transcriptional changes in ECs in these conditions via RNA sequencing for ECs cultured under both flow conditions in straight and spiral vessels as well as under static conditions. Principle component analysis (PCA) of gene expression data showed clustering of individual groups, with the largest variance between static and all flow conditions (Figure 3.1.3C). Activation of classical flow dependent genes was confirmed in all flow conditions compared to static culture (Figure 3.1.3D, E). Among these genes, *KLF2* and *KLF4* appeared to only change with the onset of flow but were not sensitive to a further increase in flow whereas *SMAD6*, *SMAD7*, and *NOS3* increased further at higher flow conditions. Among the genes differentially expressed in straight vessels due to the increase of flow, 52% (533/1012) overlap with genes differentially expressed in the onset of flow (static vs. low flow condition) (Figure A4A, B). The genes unique to the increase of flow include upregulation of many genes previously reported to regulate vascular development and flow sensing,[46–48] such as Notch ligands JAG1, JAG2, Notch target *HEY2* and other transcription factors like *SNAI2*, transmembrane proteins *IL21R*, *EFNB2*, transporters *GJA5*, peptidases *MMP10*, *MMP1*, *MT1F*, growth factors and cytokines *NOG*, *DKK2*, *WNT4*, *CXCL12*, *TGFB1,* and other molecules such as *VCAN,* and *CYP1B1* (Figure A4C). GO enriched terms for this group of genes showed upregulation of cellular response to growth factors, vascular development, transmembrane receptor protein tyrosine kinase signaling pathway, blood vessel morphogenesis, cell migration and motility and others (Figure A4D).

Approximately 66% (722/1136) of differentially expressed genes in straight vessels overlap with those in spiral vessels in response to increased flow (Figure 3.3D). Almost all overlapping genes are changed in the same direction (99%), suggesting a conserved response to flow in both geometries (Figure A5A). *MARC2*, *PTX3* and *STX11* did not follow this trend and were upregulated in spiral vessels with increased flow, but downregulated in straight vessels. Interestingly *PTX3* has been reported as a biomarker for endothelial dysfunction in preeclampsia, which is a disease caused by spiral artery dysfunction.[49] Many genes downregulated in straight vessels by the increase of flow did not show changes in spiral vessels, such as growth factors *CTGF*, *FGF2*, *NRG1*, *FGF16*; transmembrane proteins *CAV1*, *UNC5A*, *KIT*, *SMAD4A*; transcription regulators *EGR1/2/3*, *MAF*, *MYRF*, *MZF1*; transporters such as *LDLR*, cytokines *TNFSF18*, *IL12A*, *CCL2*, *CCL16*, *CCL28* (Figure A5B). This suggests that the EC response to flow in spiral vessels is a combination of both canonical flow pathways and a distinct response involving a wide range of other transcripts.

Increased flow also led to an additional 1294 genes significantly changed in spiral vessels that were not in straight ones (Figure 3.1.3F). High flow in spiral vessels appeared to activate growth factors such as *DKK1*, *ESM1*, *BMP2*, *PDGFA*, *OSGIN2*, and *VEGFC*; many solute carrier (SLC) and ATP-binding cassette (ABC) superfamily transporters, transcription regulations *GLI2*, etc, cytokines *CXCL1*, peptidase *TLL1*, *ADAMTS1*, *ADAMTS9*, *TASP1*, etc, kinase *PODXL*, *EPHA5*, *HK2*, *PRKCA*, *CCT2*, *MAP2K1*, etc (Figure 3.1.3G, A6A). In addition, high flow in spiral vessels repressed growth factors such as *MST*, *NRG2*, *GDF3*, *GAS6*, *IGF2*; transmembrane receptors *CHRNA1*, *SELP*, *LRP1*, *ITGB3*, *ROBO3*; transporters including *MAL2*, *ATP2A3*, *RBP1*, *APOL1*, and several members of SLC and ABC super families; transcriptional regulators such as *NOTCH3*, *CITED4*, *CAND2*, *FOXO4*, *DACH1*, *EBF3*; cytokines *DKK3*, *CSF1*, *FLT3LG*; GPCR group *SIPR4*, *OPRL1*, *HTR2B*; and kinases *PDGFRB*, *CKB*, *SBK1* (Figure 3.1.3F, A6A). GO term analysis showed the upregulation of primarily ribosome biogenesis, which would be critical for cellular growth and proliferation (Figure A6B). These expression profiles show that spiral vessels share a common set of flow responsive elements with straight vessels but have an additional response that appeared to promote vascular growth.

PCA analysis showed the separation of straight and spiral geometries was enhanced under higher flow conditions (Figure 3.1.3E). Under low flow conditions (Re << 1, inertia effect is negligible) ECs in the two geometries were largely similar, with only a handful of significantly regulated transcripts (Figure A6A). These include *CYTL1*, which is known to upregulate proangiogenic function, but not proinflammatory pathways.[50] *HES2*, a downstream Notch pathway gene, *STK32B* (serine/threonine kinase 32B), and *CCND1*, a cell cycle regulation gene, were also upregulated in low flow spiral vessels. The upregulation of these genes was further enhanced in high flow conditions. In addition, many genes that regulate vascular development were upregulated when comparing spiral to straight vessels at high flow. For example, growth factors *HGF*, *DKK1*, *ESM1*, *PGF*, *PDGFA*, *GDF6*, *PDGFB*, *CTGF*, *VEGFC*, *BMP*2, *PDGFC*; Peptidases *ADAMTS1*, *ADAMTS9*, *MME*, *CTSS*; kinases *EPHA5*, *MPP4*, *PODXL*, SPRY2, *CDK7*, *MAP2K1*; transmembrane receptors *KIT*, *SELE*, *ULBP2*, *PLXNA2*, *LRP8*; transcriptional regulators *GLI2*, a hedgehog pathway mediator, *ATF3*, required for endothelial regeneration,[51] *FOSL1,* required for vascular formation*,*[52] and many solute carrier and ATP family transporters (Figure 3.1.3G). Ingenuity pathway analysis showed ECs in spiral vessels have activated upstream regulators including pro-survival factors *HGF*, *PGF*, *EGF*, *VEGF*, and *HIF-1a*. Upregulated functional pathways included vascular development, angiogenesis, vasculogenesis, cell invasion, and cell survival, whereas cell death and necrosis were decreased compared to the straight vessel in high flow conditions (Figure 3.1.3H, A7B). Spiral vessels also showed the activation of anti-apoptotic and proliferative pathways marked by cell cycle and mitotic genes. PDGF family members were relatively more abundant, as were molecules associated with IL-8 and HGF signaling (Figure A7B).

Taken together, the bulk RNAseq showed that spiral vessels maintain a normal flow response to certain extent, but curvature and torsion modified the response by upregulating markers for transporters, cycling, survival, and downregulating markers of cell death. These data suggest flow in spiral vessels promoted vascular growth or development rather than inducing a common inflammatory response to disturbed flow.

Single cell RNAseq reveals heterogeneity in transcriptional responses to flow based on vessel geometry

We hypothesized that endothelial cells exposed to flow within spiral vessels experienced a spatial variation in hemodynamic forces not present in straight vessels that would result in a heterogeneous transcriptional response to flow. To understand this heterogeneity at the single cell level, we sequenced the transcriptomes of over 2000 individual ECs pooled from three to four devices of each geometry cultured at high flow (Q = 50 µL/min). Dimensionality reduction by Uniform Manifold Approximation and Projection (UMAP) and cluster analysis was performed using Monocle [44,45,53]. Projection in the top two UMAP dimensions shows overlapping contributions of ECs from spiral and straight vessels that form mostly contiguous clusters with nearly uniform expression of pan-endothelial markers such as *CDH5* (VE-Cadherin) (Figure 3.1.4A, B). Expression of classical flow-dependent genes, including *KLF4* and *NOS3*, is distributed throughout the major clusters of ECs in this projection (Figure 3.1.4C). Interestingly, we identified variation in gene expression across the first UMAP dimension driven largely by cell cycle genes that have been shown to be regulated in part by flow. Specifically, a large cluster of cells to the right in UMAP space (cluster 3) express genes such as *MKI67* consistent with active

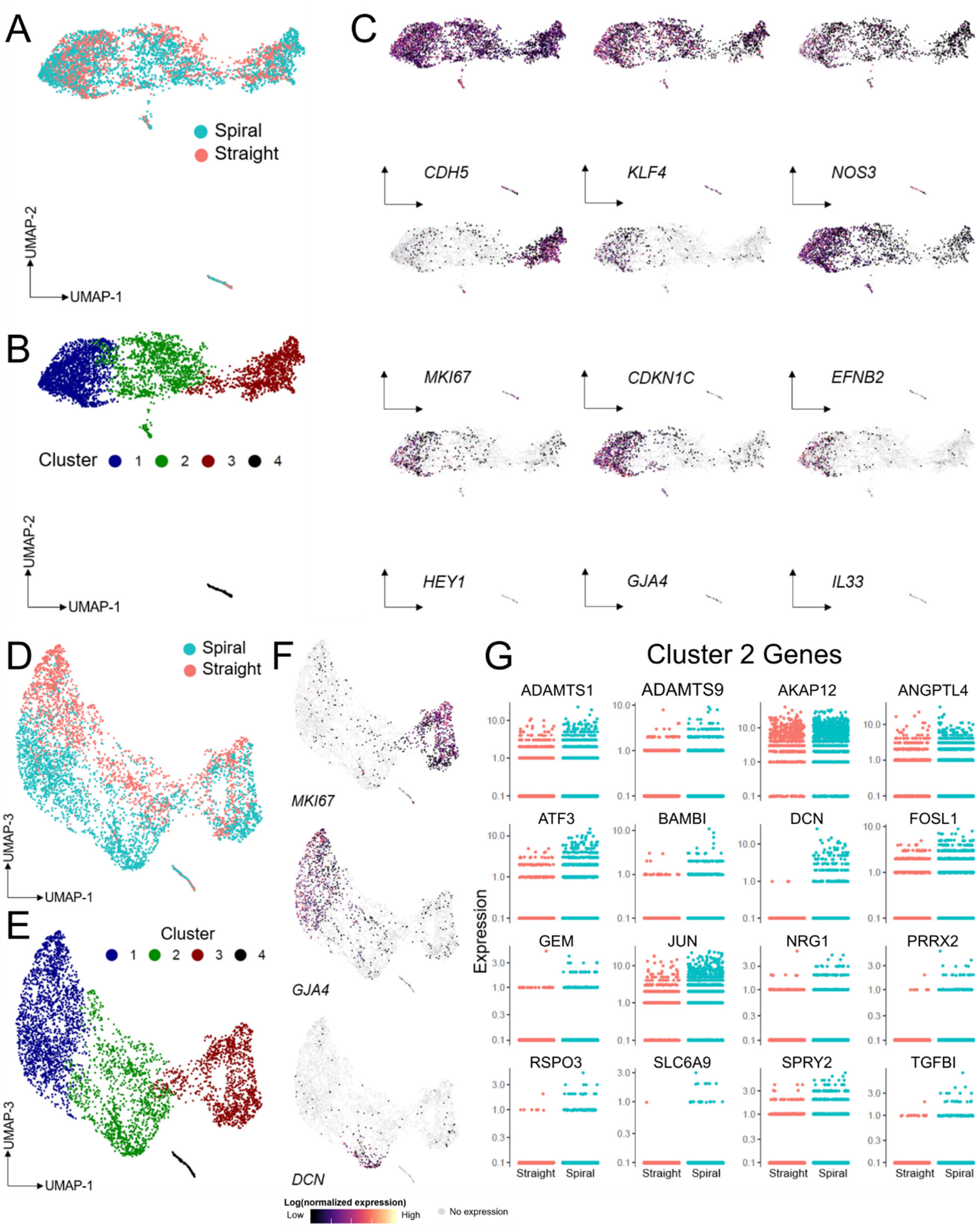

Figure 3.1.4 Single cell RNA sequencing comparison of cells cultured under high flow in spiral and straight vessels. Uniform manifold approximation and projection (UMAP) plots of spiral high flow and straight high flow cells (**A**), computationally derived clusters (**B**), and the distribution of endothelial and cell-cycling genes across cells (**C**). UMAP plots of the first and third UMAP dimensions (**D**), the corresponding location of clusters in this dimensional space (**E**) with examples of cluster specific genes (**F**), as well as a selection of genes identified as significantly differentially expressed (**G**).

cell cycle status, whereas cells clustered to the opposite pole (cluster 1) express genes implicated in cell cycle arrest and arterial phenotype shown to be regulated by the Notch pathway downstream of laminar shear stress (including *CDKN1C*, *EFNB2*, *HEY1*, *GJA4*, and *IL33*, Figure 3.1.4C).[54–56]

To evaluate heterogeneity in the transcriptional response of ECs resulting from vessel geometry, we next identified differentially expressed genes based on scRNA-seq data of EC from straight verses spiral vessels. Examination of the third UMAP dimension revealed separation in transcriptional space between EC from straight verses spiral vessels, with many of the identified differentially expressed genes polarized in this dimension (Figure 3.1.4D-F). Among the genes upregulated in EC from spiral vessels are many that were also identified as differentially expressed in bulk RNA-seq analysis, including *ATF3*, *SPRY2*, *IL8*, *JUN*, *AKAP12*, *ANGPTL4*, *FOSL1*, and *ADAMTS1*, and *ADAMTS9* (Figure 3.4G, A8A). Most of these genes are expressed in a common pattern, with increased expression in cells localized in UMAP space to the lower (spiral) portion of cluster 2. This suggests a distinct transcriptional program amongst the primarily spiral ECs in this region which may correspond with their transcriptional response to specific hemodynamic conditions unique to spiral vessels under high flow. In further support of this hypothesis, analysis of the scRNAseq data also identified differentially expressed genes not detected in bulk RNA-sequencing, including *DCN*, *SLC6A9*, *GEM, NRG1, RSPO3, BAMBI, TGFBI*, and *PRRX2*, that were highly specific to EC from spiral vessels localized in cluster 2 (Figure 3.1.4G, A8B). These data suggest that flow in spiral vessels induced a population of ECs with unique gene expression profiles that are not present in straight vessels, with potential roles in processes such as angiogenesis, vascular growth, and inflammatory and stress responses.

3.1.5 Discussion

3D vascular networks have been engineered to support complex tissues, but most designs have been geometrically limited to rectilinear structures with a constrained range of hemodynamic profiles.[34,57,58] Reproducing the structure of complex networks with continuous curvature was only made possible by recent advances in bioprinting,[32] and is still restricted by printable materials. Printing artifacts create discontinuity and stepwise changes in wall geometry that disturbs flow in vessels. Building perfusable and endothelialized vessels with continuous curvature and torsion as in vivo has not been achieved. Here, we developed a spiral vessel platform which allows for the systematic control of 3D vessel geometry (diameter, curvature, and torsion) and is easy to fabricate rapidly and reproducibly. In one step, this approach creates a versatile vascular conduit that spans several orders of magnitude. Vessel diameters approach 100 µm, span spiral diameters in the millimeters, and the total vessel length stretches easily into many centimeters. Under perfusion these vessels support a healthy endothelium with robust junctions and rich granules and appeared to guide the architecture and functional organization of parenchymal cells. This large vessel surface area can be tuned to fit into tissues of various shapes and sizes and can serve as the foundation of a highly vascularized tissue.

The precise control of 3D geometries in this spiral vessel platform provides opportunities to study the contribution of individual geometric parameters to blood flow and corresponding vascular response that are otherwise hard to dissect in vivo or in other in vitro models. In this work, we took the first step to compare the 3D flow in spiral and straight vessels of same diameter at the same flow rate, and the corresponding endothelial cell response. We showed 3D curvature had little change in the primary flow but led to bulk flow rotation in spiral vessels in a creeping flow regime ($Re < 0.1$ and $De < 0.1$) and mixing at a slightly higher flow rate ($Re < 1$, and $De < 2$). The spiral curvature led to changes of wall shear stress along circumferential direction and generated a stress gradient in 3-D space. This additional stress gradient, distinct from the pressure gradient driving axial flow, likely induced flow mixing in the high flow condition. By culturing ECs in spiral and straight vessels with the same vessel diameter and length, we were able to distinguish the effect of curvature from the conventionally recognized flow response in ECs to laminar flow using both bulk and single cell RNAseq.

Bulk RNAseq analysis revealed that, in addition to a common flow-responsive gene set towards anti-inflammatory, anti-adhesion, and vascular development pathways with straight vessels, ECs in spiral vessels express a distinct gene set associated with upregulated cell cycling, transporters, pro-inflammation, cellular growth and vascular morphogenesis. The combination of both features suggests that curvature and torsion in small vessels promote vascular growth even under laminar flow regimes.

Most studies on curvature have focused on large vessels and cells located in the inner or outer curves have shown altered phenotypes corresponding to the different shear stress levels in these regions.[15,17,29,59] Our spiral microvessels showed little change in the primary flow but introduced a weak secondary flow with no “disturbed flow” features when compared to the straight vessels at the same flow condition. Using single cell RNAseq, we did not identify two distinct cell groups in spiral vessels deviating from the straight vessels, rather, cell clusters overlap significantly in the two geometries, confirming that ECs in spiral vessels share significant gene regulation with straight vessels in response to laminar flow. In addition, there is a group of ECs in spiral vessels separated from the main flow-responsive clusters, suggesting a different EC response mechanism than wall shear stress. It is possible that the combined wall shear stress gradient and bulk flow mixing provide a new set of perturbations on ECs. This suggests that the twists and turns found throughout the vascular system contribute to a more heterogenous EC response to flow than is currently appreciated.

During development and tissue regeneration, curved vessels often appear. Our data indicate the transient appearance of complex vascular curvature may benefit vascular growth and remodeling. ECs in small curved vasculature may provide angiocrine or growth signals to surrounding tissue and promote tissue organization and regeneration. The spiral vessel system we developed here provides opportunity to systemically define and evaluate the role of heterogeneous vessel geometries in the EC response to flow. Future studies would be critical to understand how these transcriptional programs translate to EC behavior and modify vascular remodeling. This understanding will provide important insights into how heterogeneous vascular structures contribute to differential development and pathogenesis, as well as informing new engineering strategies to improve tissue vascularization and support tissue regeneration.

3.1.6 Conclusions

We have designed a platform to rapidly fabricate 3D constant curvature vessels for engineering vascularized tissues and for investigating the effect of Dean flows on endothelial cells. Spiral vessels can serve as the scaffolding for cardiac constructs, or as a model system for cancer vascularization. We demonstrated that the non-uniform flow in curved vessels caused a clear shift in RNA expression and believe that constant curvature spiral vessels represent a controllable platform to systematically investigate these effects.

3.2 Endothelial responses to curvature in engineered cerebral aneurysms

3.2.1 Abstract

Hemodynamic factors have long been associated with clinical outcomes in the treatment of cerebral aneurysms. Computational studies have provided valuable estimates of these conditions and correlated them with disease state, but they ultimately are not able to provide measurable information on the response of the endothelial cells integrating these cues. Here we bridge this gap by fabricating anatomic-scale idealized- and patient-specific aneurysms in which the endothelial response to aneurysm-specific hemodynamic conditions can be investigated. We show that vessel curvature induces changes in WSS and WSSG that are correlated with differences in cell morphology, cellular protein localization, and RNA levels. Cells in higher WSS are more aligned with flow and display strong Notch1-ECD polarization, while WSSG differences due to curvature were associated with less alignment and an attenuation of Notch1-ECD polarization in low WSS conditions. Gene expression information can be obtained from these models providing further insight into the response of endothelial cells to patient-specific hemodynamic features. These results highlight a new approach to connecting computational studies to the underlying endothelial biology that is thought to mediate disease.

3.2.2 Introduction

With spiral vessels we explored curvature and secondary flows in small diameter vessels that had not been well explored in the literature. In contrast to this, the effects of curvature and disturbed flows are widely appreciated in large vessels but modeling the effects of large vessel curvature on endothelial cells in vitro has remained challenging.[10] Interest in these vessels has been driven by vascular pathologies where the local hemodynamic conditions are predictors of disease or are clinically useful, as in the case of cerebral aneurysms.

In this field, research over the last two decades on the effect of local hemodynamics on the formation, progression, and rupture of cerebral aneurysms has attracted considerable research attention.[60] Computational fluid dynamics (CFD) studies of patient specific aneurysm geometries have correlated different hemodynamic patterns with aneurysm rupture[61] and as a result have spurred intense interest in the mechanisms that underlie this observation. Endothelial dysfunction is thought to contribute to aneurysm formation, progression, and rupture, and can develop as a consequence of certain hemodynamic stresses.[62] For example, in a retrospective analysis intra-aneurysm wall shear stress (WSS) and oscillatory shear index (OSI) have been shown to have significant value in discriminating between ruptured and unruptured aneurysm status.[63] These connections between aneurysm rupture and hemodynamic conditions, however, have not always been in agreement, with some studies indicating high WSS is associated with rupture and others indicating low WSS.[64] Sources for this error are thought to arise from the heterogeneity of aneurysm pathology, but they highlight the missing link in many CFD studies. While they provide insightful and significant quantification of aneurysm hemodynamics, they do not provide measurable information on the response of endothelial cells within the aneurysm.

The challenging problem of connecting the results of CFD studies to the biological response of endothelial cells has been approached through a variety of methods. In vitro models that replicate specific hemodynamic features, like high or low WSS,[65] wall shear stress gradients (WSSG),[66] or OSI,[67] have proven useful in investigating the response of endothelial cells to specific conditions. These kinds of studies in combination with animal models of disease[68,69] have informed a greater understanding the disease pathology, but they are ultimately limited by their inability to recapitulate the scale and complexity of normal human anatomy. Recently, advances in 3D printing have made it possible to produce anatomical scale copies of model and patient derived vascular geometries.[70,71] These models have enormous potential to bridge the gap between CFD studies and endothelial responses, but have not yet been applied to investigate the effects of geometrical and hemodynamic differences on endothelial cells.

Here, we explored the effect of vessel curvature and the resulting changes in aneurysm hemodynamics on the expression and distribution of endothelial markers associated with flow or inflammation. We fabricated idealized vessel geometries with either a straight or curved parent vessels and equal sized saccular aneurysms and showed that these engineered geometries could be cellularized, perfused at physiologic flow rates, and endothelial responses correlated with local hemodynamic conditions. We further demonstrated that this approach could be applied to geometries derived from patient-specific imaging data and used to identify transcriptional differences between vessel regions.

3.2.3 Methods

Model fabrication

CAD designs of idealized aneurysm models with and without curvature were 3D printed using a stereolithography printer (Form 2, Formlabs) to crosslink photoreactive resin (High Temp, Formlabs) at 0.025 mm layer height. 3D printed models were sanded and polished until transparent to remove printed layer lines. Smoothed 3D printed models were then embedded in polydimethylsiloxane (PDMS, Sylgard 184, 10:1 base:curing ratio, Dow Corning) using a machined acrylic mold that minimized the PDMS wall thickness and enabled high resolution fluorescent imaging. The PDMS was cured by baking at 65 °C for at least 3 hours before the 3D printed model was removed by cutting open the PDMS using a surgical scalpel. The PDMS vessel was then carefully closed using additional uncured PDMS to seal the device and form a perfusable PDMS vessel. Once sealed, PDMS vessels were sterilized by autoclaving. Patient specific aneurysm models were prepared in the same way, but 3D rotational angiography data was used as the source for the model geometry using a previously reported pipeline.[72]

Cell culture

All experiments were performed using human carotid artery endothelial cells (HCtAEC, Cell Applications) between passage 4 and 7. HCtAEC were cultured using Human MesoEndo Cell Growth Media (Cell Applications) on standard tissue culture polystyrene in a 37 °C incubator with 5 % CO_2.

Model preparation and seeding

To improve cell adhesion, sterilized PDMS vessels were plasma treated for 1 minute at ~100 watts (Plasma Prep II Etcher, SPI Supplies). Immediately after plasma treatment PDMS vessels were filled with a 5 µg/mL fibronectin solution (MilliporeSigma) and placed in a 37 °C cell culture incubator for 1 hour. After 1 hour the fibronectin solution was removed by aspirating. HCtAEC were trypsinized and resuspended at 1 million cells/mL in culture media and added to fibronectin coated PDMS vessels (~1 mL per vessel). Vessels were seeded at 37 °C for 15 minutes with the model being inverted at least once to ensure even cell coverage over the luminal surface. Vessels were then perfused with fresh media to clear any unattached cells and then returned to the incubator for at least 6 hours prior to the initiation of flow.

Perfusion

Seeded vessels were connected to a peristaltic pump (Masterflex L/S Digital Drive, Cole-Parmer) using platinum cured L/S 24 silicone tubing (Cole-Parmer) and custom-printed barbed connectors to connect the tubing to idealized aneurysm models. Endothelial growth media (Lonza) supplemented with 3.5 % dextran to mimic the viscosity of blood was used to as the media for perfusion. Media reservoirs were vented through a 0.22 µm filter to allow for gas exchange. Flow was started at 30 mL/min for 30 minutes to purge the vessels of any bubbles and to confirm vessels did not leak. The flow was then set to 150 mL/min and run continuously for 24 hours in an incubator. After 24 hours the vessels were removed from the flow loop and formaldehyde fixed (4% formaldehyde, 15 minutes). The flow waveform was recorded using an ultrasonic flow meter (Titan Atrato).

Immunostaining and Imaging.

Fixed vessels were permeabilized and blocked in phosphate buffered saline (PBS) containing 2% bovine serum albumin (BSA, MilliporeSigma) and 0.5% Triton X-100 (MilliporeSigma) for 30 minutes. Vessels were stained for CD31 (abcam ab28364, 1:30), von Willebrand Factor (vWF, abcam ab8822, 1:100), VCAM-1 (R&D Systems, BBA5, 1:50), and Notch1-Extracellular Domain (BD Biosciences, 566023, 1:100). For unconjugated primary antibodies, the antibody was diluted in blocking solution and incubated at 4 °C overnight. After washing, secondary antibodies (Goat anti-rabbit 568, Invitrogen A-11011, 1:100), Hoescht 33342 (40 µg/mL), and labeled primary antibodies were added in blocking solution and incubated for 1 hour at room temperature. Vessels were then washed and stored in PBS at 4 °C until imaging. 6 vessels for each geometry were imaged, with 3 stained for nuclei, CD31, Notch1-ECD, and F-actin and the remaining 3 stained for nuclei, VCAM-1, VWF, and F-actin.

For each device 20x fields were obtained at five predefined locations in the aneurysm model (Figure A9). These were aligned relative to the bottom surface of the aneurysm dome and included the dome, a region in the proximal neck of the dome, the distal neck of the dome, and proximal and distal regions of the parent vessel. Each vessel was imaged on a Nikon Eclipse Ti microscope equipped with a Yokogawa W1 spinning disk system using a 20x extra-long working distance objective (Nikon MRH08230). Z-stacks at each region were collected with a 2 µm step size.

Image analysis

Maximum intensity projections of Z-stacks were used to manually outline cells in each region in Fiji. At least 50 cells were identified in all fields. Cell outlines were then used to generate geometric descriptors for morphological analysis and comparison using the built-in measurement tools in Fiji. To determine the distribution of different labeled proteins we implemented an analysis pipeline in Fiji. Briefly, whole field images were broken down into images of individual cells as defined by cell traces. Each individual cell was evaluated independently by splitting the cell into equal length segments along a vector defined by the direction of flow. The fluorescent intensity in these segments was then compared to determine the segment with the greatest fluorescent intensity for that cell. This process was repeated for all cells in the field and exported. Morphological and segment intensity data was imported into R for processing and statistical analysis. Morphological data was compared between groups using a Student's t-test, while segment data was compared using a Chi-squared test of independence. P values of less than 0.05 were considered significant.

Gene expression analysis

Patient derived 3D-printed aneurysm models were divided into three regions for gene expression analysis: (1) the proximal parent vessel, (2) the aneurysm dome, and (3) the distal parent vessel. After 24 hours of perfusion each region was mechanically separated and independently perfused with RLT lysis buffer (Qiagen), and the lysate was collected. Total RNA from each zone was purified using RNAeasy Mini Kit (Qiagen) and RT-PCR was performed using a real-time PCR system (Applied Biosystems) with Fast SYBR Green Master Mix (Applied Biosystems). The abundance of several key vascular factors (VCAM-1, ADAMTS-1, MMP-9, GJA4, and NOS3) was determined relative to GAPDH. qPCR data were evaluated using R and Minitab 18. Data were analyzed in a repeated measures analysis of variance design and pairwise comparisons were performed using Tukey's method. P values < 0.05 were considered statistically significant.

3.2.4 Results

Curved and straight models were designed to provide different flow conditions in the aneurysm neck and sac (Figure 3.2.1A). 3D CAD models were successfully fabricated by 3D printing (Figure 3.2.1B) and converted into perfusable vascular phantoms by casting in PDMS (Figure 3.2.1C). Models fabricated in this way supported physiologic pressure and flow without leaking or deformation in the vascular structure. The devices were autoclaved, plasma treated, coated with fibronectin, and then seeded with HCtAECs before culturing under flow for 24 hours. Seeded

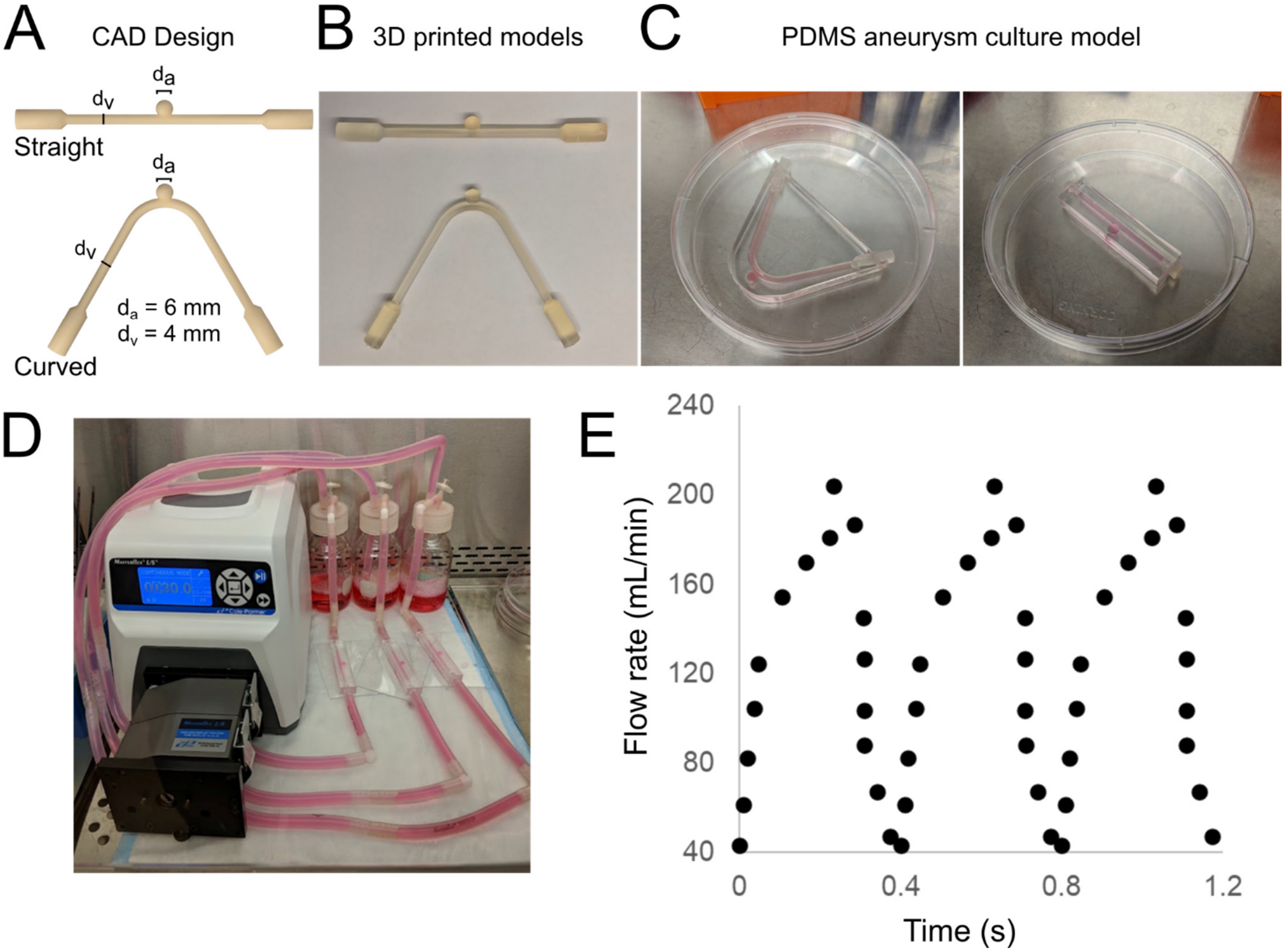

Figure 3.2.1 Model fabrication workflow. Straight and curved idealized vessels were designed with identical vessel and aneurysm diameter (A). Models were 3D printed and post-processed prior to embedding in PDMS (B). After removal of 3D printed models from PDMS, devices were suitable for culture (C). Seeded PDMS aneurysm models were cultured in independent flow loops using a peristaltic pump (D) with a pulsatile flow waveform (E).

vessels were cultured under in independent flow loops (Figure 3.2.1D) driven by a peristaltic pump that provided a pulsatile flow waveform (Figure 3.2.1E).

After 24 hours devices were fixed, stained, and imaged to examine morphological and protein localization differences in similar regions of different vessel geometries (Figure 3.2.2A, B). Cells displayed good junctional staining and maintained confluency over the flow period in regions of interest. Within the same vessel geometry cell area was highest in the proximal and distal parent vessel regions were the flow was primarily axial. Cell area was not significantly different in the three dome regions for the same geometry (Figure 3.2.2C). Cell perimeter followed a similar trend (Figure 3.2.2D), but cell shape index was consistent among all regions of individual geometries (Figure 3.2.2E). Although these trends were present in both geometries, the absolute

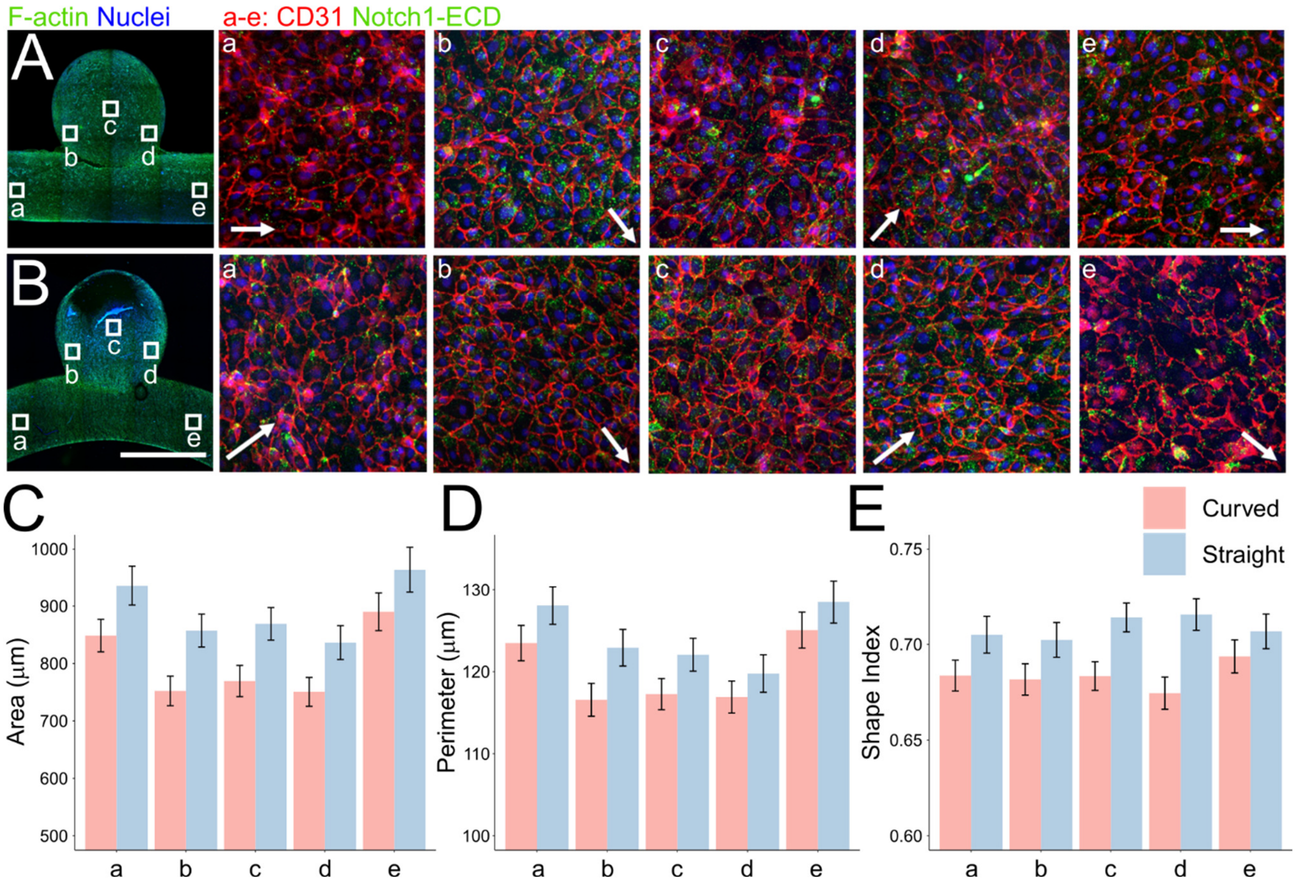

Figure 3.2.2 Endothelial morphology in aneurysm regions under flow. Straight (A) and curved (B) vessel geometries imaged at various regions near and within the aneurysm dome after 24 hours of flow. Morphological parameters including area (C), perimeter, and shape index (E). Error bars represent 95% confidence intervals. a: proximal, b: proximal dome, c: dome, d: distal dome, e: distal.

area, perimeter, and shape index were lower in curved vessels than in straight vessels. Cell orientation was also determined by assigning the major axis of an ellipse fit to the cell outline as the cell direction. Cells in the center of the aneurysm appeared relatively unorganized, while cells in the proximal and distal regions of the dome as well as the parent vessel were more aligned and clustered around a smaller range of angles (Figure A10).

We next wanted to consider the intracellular distribution of proteins in regions of the vessels where the hemodynamic conditions are different. To achieve this, we separated images of individual cells into equal length segments along the direction of flow and identified the segment with the most protein staining present (Figure 3.2.4A). From this we compiled frequency statistics to evaluate which segment of the cell contained the maximum signal most often. The extracellular domain of Notch-1 (Notch1-ECD) has been shown to polarize in the direction of flow and we evaluated its cellular distribution along the length of the cell in different vessel regions. In the proximal and distal regions of the parent vessel, the Notch1-ECD was strongly associated with

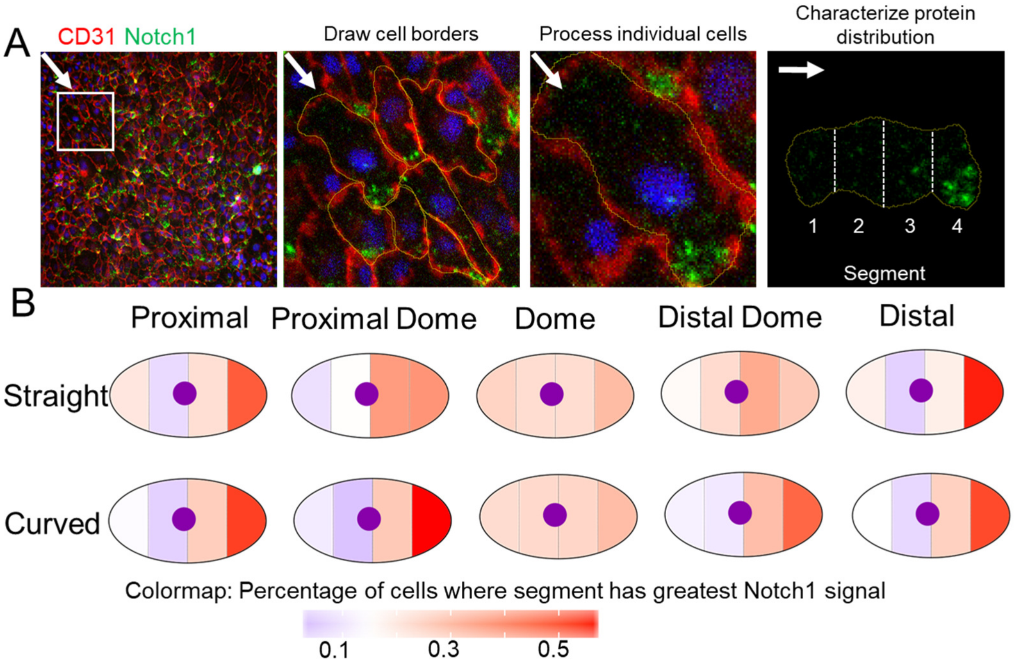

Figure 3.2.3 Notch1-ECD Distribution in idealized aneurysm regions. Approach to quantifying protein distribution in individual cells (A). Measured distribution of Notch1-ECD in endothelial cells in different aneurysm models (B).

the downstream segment of the cell. Within the aneurysm the distal and proximal neck regions appeared to maintain some polarization in the downstream half of the cell, whereas the distribution of Notch1-ECD in the center of the dome was uniform (Figure 3.2.4B).

The peak and time averaged values of wall shear stress (WSS, taWSS), wall shear stress gradient (WSSG, taWSSG), as well as the oscillatory shear index (OSI) were calculated through computational fluid dynamics simulations performed by the Aliseda group (Figure 3.2.5A, Figure A11A-D).[72] These showed that the highest shear forces were in the parent vessel regions for both geometries, with curved vessels under higher absolute loads. The shear forces were considerably lower and more comparable in all regions of the aneurysm dome for both vessel geometries. The WSSG followed a similar trend peaking in the parent vessel regions, but it was also significantly elevated at the distal neck of the aneurysm where flow is partially diverted into the dome. This effect is greater in the curved vessel than the straight vessel and is also associated with larger values of WSSG downstream in the distal parent vessel of curved geometries. OSI, which measures the degree of shear reversal from the time averaged direction during a pulsatile cycle, was greatest in aneurysm regions but reached a maximum in the distal dome of the curved geometry. In the parent vessel regions where OSI values were lowest and WSS levels were highest the greatest polarization of Notch1-ECD towards the downstream segment were observed (Figure 3.2.5B). Polarization in the proximal and distal dome regions was stronger in curved vessels than straight vessels, despite similar levels of WSS. Neither VCAM-1 (Figure 3.2.5C) nor VWF (Figure 3.2.5D) showed polarization in the direction of flow but did appear more frequently in the center segments of cells.

To further explore the possible applications of this fabrication technique we created patient specific PDMS models from clinical 3D rotational angiography data of a cerebral aneurysm. Angiography data was segmented and converted in 3D mesh files, 3D printed, and cast into PDMS (Figure 3.2.6A-C). We seeded these models and cultured them under flow for

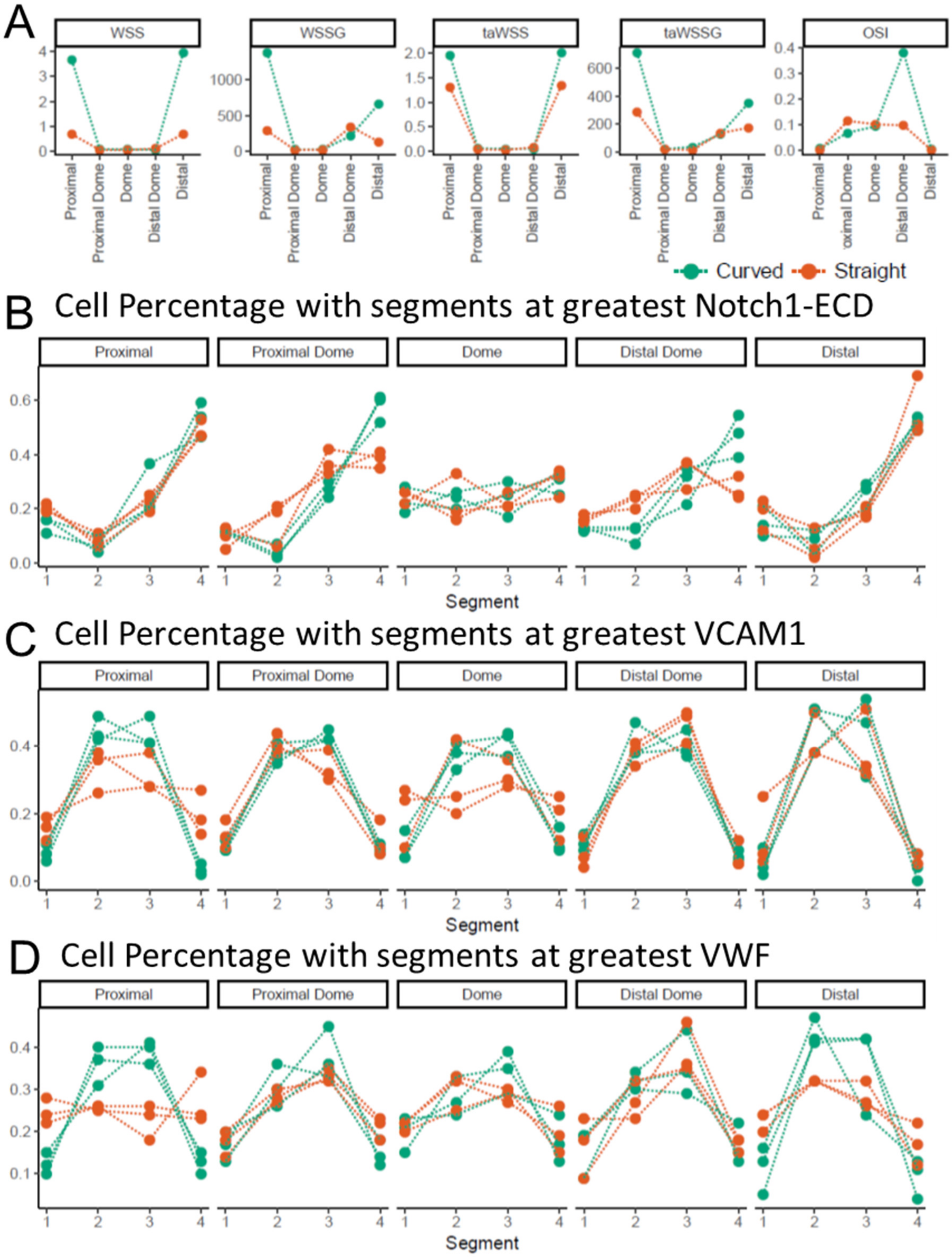

Figure 3.2.4 Hemodynamic features and protein distribution in idealized aneurysms. Hemodynamic features measured from CFD data in different aneurysm models (A). Distribution of Notch1-ECD (B), VCAM1 (C), and VWF (D) along the length of cell (1 = upstream pole, 4 = downstream pole). WSS: wall shear stress, WSSG: wall shear stress gradient, ta: time averaged, OSI: oscillatory shear index. Units for WSS and taWSS are in Pa, WSSG and taWSSG are in Pa/m.

hours, qualitatively observing flow induced alignment in parent vessel regions but not within the aneurysm dome (Figure 3.2.6D). To determine if transcriptional differences existed between ECs in different regions, we separated the PDMS molds into 3 segments (Proximal, Aneurysm, and Distal, Figure 3.2.6C) after 24 hours of perfusion and isolated RNA from each. qPCR showed cells in the distal region of the aneurysm had significantly reduced levels of *GJA4* compared to the proximal and dome regions (Figure 3.2.6E). Higher variability was observed in other genes tested and no statistically significant difference in expression were measured although a trend toward lower levels of *VCAM-1*, *NOS3*, and *ADAMTS1* in the aneurysm was present in 2/3 samples, which correlated with regions of unique hemodynamic conditions in fluid dynamics simulations performed by the Aliseda group (Figure A11E-G).

3.2.5 Discussion

A major challenge to translating CFD research on aneurysm hemodynamics into biological responses has been the fabrication of anatomically relevant models. Recent advances in 3D printing have enabled the straightforward fabrication of idealized and patient-derived aneurysm models and these have been used for additional hemodynamic studies (e.g. particle image velocimetry[73]), for surgical planning,[71] and recently for seeding endothelial cells.[74] In this work we extended this 3D printing approach and investigated the effect of vessel curvature on the endothelial response to flow in model aneurysms. We further demonstrated this paradigm can be used to correlate hemodynamic conditions in a patient specific model with the transcriptional response of endothelial cells under flow.

Anatomically sized idealized models supported cell seeding and perfusion with pulsatile and physiologically relevant shear stress and pressure levels. Endothelial cells in different aneurysm regions displayed different shapes and sizes, reflective of their distinct hemodynamic conditions. For both curvatures we observed smaller cells in regions of lower WSS in the aneurysm sac, following well established trends for endothelial cells.[7] Cells in curved

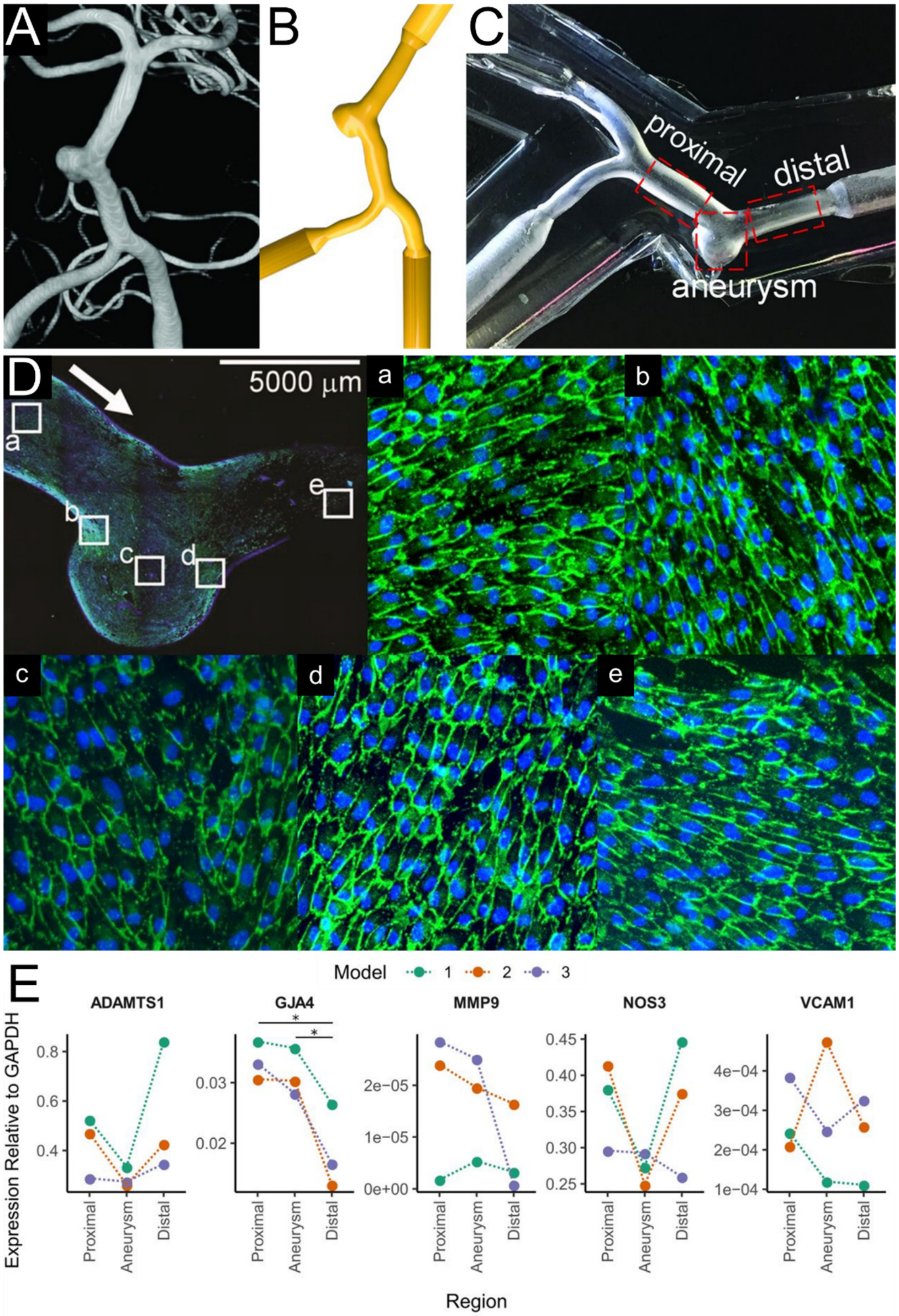

Figure 3.2.5 Fabrication, culture, and mRNA analysis of patient derived aneurysm model. Pipeline for fabrication of patient specific aneurysm models including 3D rotation angiogram (A), derived 3D model (B), and PDMS aneurysm mold (C) showing segments used for RNA isolation. Representative images of patient specific model seeding and cell orientation after 24 hours of flow (green = CD31, blue = nuclei) (D). RNA expression of several transcripts relative to GAPDH in proximal, aneurysm, and distal regions (E).

geometries were almost always significantly smaller than cells in similar regions of straight vessels. This difference in size may be related to the larger values of WSSG present in the proximal and distal parent regions of curved vessels. Large WSSGs have been reported to promote EC proliferation and inhibit alignment,[75] which could explain the differences in size through additional proliferation in these regions. Further support for this phenomenon is observed in the cell orientation data (Figure A10) where cells are significantly more aligned in the direction of flow in the distal region of curved vessels where the WSSG is considerably lower than in the proximal region. A similar shift in alignment is not observed in the straight vessel with comparably small WSSG.

Notch1 was recently recognized as a mechanosensor in endothelial cells and its extracellular domain is known to polarize towards the downstream pole under normal flow.[55] This relatively unique feature provides a visual marker of local endothelial shear sensing. We characterized the cellular distribution of the Notch1-ECD in cells in all regions of both models and found them to correlate well with WSS conditions. In the high WSS proximal and distal regions of both geometries Notch1-ECD was highly polarized towards the downstream end of the cell. In the center of the aneurysm sac Notch1-ECD appeared uniformly distributed, consistent with the near zero WSS in that region. This polarization was also present in both the proximal and distal aneurysm neck for curved vessels, but the effect appeared smaller for straight vessels in the proximal dome and almost absent in the distal dome. The WSS in the distal dome in both regions is less than 1 dyne/cm^2, but the WSSG is more than 50% larger in straight vessels, suggesting polarization may be altered by WSSG in low flow conditions. In the higher WSS regions of both geometries, large WSSG values did not interfere with Notch1-ECD polarization. Interestingly an oscillating flow direction (large OSI) in the distal dome of curved vessels did not prevent Notch1-ECD polarization. We also applied this approach to VCAM-1 and VWF, neither of which showed significant polarization or enrichment in different regions of the aneurysm dome. We did not observe increased VCAM-1 staining in the aneurysm dome as has been reported previously.[62,76] Other reports have indicated VCAM-1 levels in disturbed flow in in vitro systems can peak after several hours of flow and then return to baseline by 24 hours.[77] Investigating the expression at an earlier timepoint, or performing a more functional adhesion assay with peripheral blood mononuclear cells[78] would provide additional insight to the conditions within the aneurysm.

In addition to these idealized models, we also fabricated and culture a model derived from patient imaging data. With this patient-specific geometry we were able to perfuse and collect RNA from distinct aneurysm regions. From this RNA we observed a significant decrease in *GJA4* in the distal vessel segment where WSS and WSSG were highest. *GJA4* is downstream of NOTCH signaling and is typically activated by increased shear stress.[54] This relative decrease provides further evidence higher WSSG may interfere with normal WSS signaling pathways, but oscillatory flows like those present in the distal region are also known to disrupt *GJA4* expression.[79] While not significantly downregulated, we also observed decreases in *NOS3*, *ADAMTS1*, and *VCAM-1* in the low shear stress aneurysm dome, matching previous reports.[77,80,81] Some error in these observations is likely from small differences in sampling that occurred when the aneurysm was manually separated into different regions. The hemodynamic differences within the aneurysm do not match the sharp demarcations necessary for isolating the sample and more granular transcriptional analysis through recently developed spatial gene expression analysis tools would be particularly insightful.[82,83]

Models like those presented here represent a powerful proof of concept for bridging the gap between CFD and biological responses, but several limitations must be addressed to provide deeper insight into aneurysm pathophysiology. While endothelial cells are a major contributor to aneurysm pathology, the smooth muscle also plays a key role in aneurysm formation and rupture[84] and efforts should be made to include them in future models. It is not uncommon for aneurysms to significantly expand throughout the cardiac cycle, inducing strain on both endothelial and smooth muscle cells.[85] These kind of strain cues can significantly alter endothelial[86] and smooth muscle biology,[87] but the thick walled devices designed here do not mimic this force. Other fabrication strategies can produce thin walled devices,[74] although tuning the mechanical properties to match native vessels remains a challenge. The applied flow waveform is also a key variable that could more closely mimic native physiology. The peristaltic pump used in this study provides pulsatile flow, but the resulting waveform is dissimilar to the cardiac cycle and alters time-dependent hemodynamic features.

3.2.6 Conclusion

While considerable research has explored the computational fluid dynamics of cerebral aneurysms, methods for directly linking CFD results to biological responses in complex geometries remain in their infancy. By taking advantage of recent advances in 3D printing we showed that models of anatomic-scale idealized- and patient-specific aneurysms can be seeded with endothelial cells and cultured under flow to correlate CFD data with endothelial responses. We showed that differences in vessel curvature caused localized changes in hemodynamic features like WSS and WSSG that correlated with cell morphology, cellular protein localization, and RNA levels. These to-scale models that more completely replicate the hemodynamic conditions throughout an entire aneurysm represent a powerful new tool for understanding the complex biological processes underlying aneurysm formation, progression, and rupture. Advances that incorporate additional mechanical cues and relevant cell types will further this understanding and may ultimately help to better inform clinical decision-making and the development of novel therapeutic interventions.

3.3 References

1. Atala, A., Kasper, F. K. & Mikos, A. G. Engineering Complex Tissues. *Sci Transl Med* **4**, 160rv12 (2012).
2. Ogle, B. M. *et al.* Distilling complexity to advance cardiac tissue engineering. *Sci. Transl. Med.* **8**, 342ps13-342ps13 (2016).
3. Lucitti, J. L. *et al.* Vascular remodeling of the mouse yolk sac requires hemodynamic force. *Dev. Camb. Engl.* **134**, 3317–26 (2007).
4. Culver, J. C. & Dickinson, M. E. The effects of hemodynamic force on embryonic development. *Microcirculation* **17**, 164–178 (2010).
5. Gimbrone, M. A., Anderson, K. R. & Topper, J. N. The Critical Role of Mechanical Forces in Blood Vessel Development, Physiology and Pathology. *J. Vasc. Surg.* **29**, 1104–1151 (1999).
6. Hahn, C. & Schwartz, M. A. Mechanotransduction in vascular physiology and atherogenesis. *Nat. Rev. Mol. Cell Biol.* **10**, 53–62 (2009).
7. Baeyens, N., Bandyopadhyay, C., Coon, B. G., Yun, S. & Schwartz, M. A. Endothelial fluid shear stress sensing in vascular health and disease. *J. Clin. Invest.* **126**, 821–828 (2016).
8. Tzima, E. *et al.* A mechanosensory complex that mediates the endothelial cell response to fluid shear stress. *Nature* **437**, 426–431 (2005).
9. Song, J. W. *et al.* Computer-Controlled Microcirculatory Support System for Endothelial Cell Culture and Shearing. *Anal. Chem.* **77**, 3993–3999 (2005).
10. Chiu, J.-J. & Chien, S. Effects of Disturbed Flow on Vascular Endothelium: Pathophysiological Basis and Clinical Perspectives. *Physiol. Rev.* **91**, (2011).
11. Chien, S. Mechanotransduction and endothelial cell homeostasis: the wisdom of the cell. *Am. J. Physiol.-Heart Circ. Physiol.* **292**, H1209–H1224 (2007).
12. Lin, K. *et al.* Molecular mechanism of endothelial growth arrest by laminar shear stress. *Proc. Natl. Acad. Sci. U. S. A.* **97**, 9385–9389 (2000).
13. Merna, N. *et al.* Laminar shear stress modulates endothelial luminal surface stiffness in a tissue-specific manner. *Microcirculation* **25**, 10 (2018).
14. Traub, O. & Berk, B. C. Laminar shear stress - Mechanisms by which endothelial cells transduce an atheroprotective force. *Arterioscler. Thromb. Vasc. Biol.* **18**, 677–685 (1998).
15. Davies, P. F. Hemodynamic shear stress and the endothelium in cardiovascular pathophysiology. *Nat. Rev. Cardiol.* **6**, 16–26 (2009).
16. Asakura, T. & Karino, T. Flow patterns and spatial distribution of atherosclerotic lesions in human coronary arteries. *Circ. Res.* **66**, 1045–1066 (1990).
17. Vincent, P. E., Plata, A. M., Hunt, A. A. E., Weinberg, P. D. & Sherwin, S. J. Blood flow in the rabbit aortic arch and descending thoracic aorta. *J. R. Soc. Interface* **8**, 1708–1719 (2011).
18. Chong, D. C., Yu, Z. X., Brighton, H. E., Bear, J. E. & Bautch, V. L. Tortuous Microvessels Contribute to Wound Healing via Sprouting Angiogenesis. *Arterioscler. Thromb. Vasc. Biol.* **37**, 1903-+ (2017).
19. Helisch, A. & Schaper, W. Arteriogenesis - The development and growth of collateral arteries. *Microcirculation* **10**, 83–97 (2003).
20. Ghaffari, S., Leask, R. L. & Jones, E. A. V. Flow dynamics control the location of sprouting and direct elongation during developmental angiogenesis. *Development* **142**, 4151–4157 (2015).
21. Han, H.-C. Twisted Blood Vessels: Symptoms, Etiology and Biomechanical Mechanisms. *J. Vasc. Res.* **49**, 185–197 (2012).
22. Pijnenborg, R., Vercruysse, L. & Hanssens, M. The uterine spiral arteries in human pregnancy: facts and controversies. *Placenta* **27**, 939–958 (2006).
23. Lorthois, S., Lauwers, F. & Cassot, F. Tortuosity and other vessel attributes for arterioles and venules of the human cerebral cortex. *Microvasc. Res.* **91**, 99–109 (2014).

24. Folkman, J. Angiogenesis. in *Annual Review of Medicine* vol. 57 1–18 (2006).

25. Geudens, I. & Gerhardt, H. Coordinating cell behaviour during blood vessel formation. *Dev. Camb. Engl.* **138**, 4569–4583 (2011).

26. Wang, C. Y. On the low-Reynolds-number flow in a helical pipe. *J. Fluid Mech.* **108**, 185–194 (1981).

27. Germano, M. On the effect of torsion on a helical pipe flow. *J. Fluid Mech.* **125**, 1–8 (1982).

28. Gammack, D. & Hydon, P. E. Flow in pipes with non-uniform curvature and torsion. *J. Fluid Mech.* **433**, 357–382 (2001).

29. Alastruey, J., Siggers, J. H., Peiffer, V., Doorly, D. J. & Sherwin, S. J. Reducing the data: Analysis of the role of vascular geometry on blood flow patterns in curved vessels. *Phys. Fluids* **24**, (2012).

30. Krenning, G., Barauna, V. G., Krieger, J. E., Harmsen, M. C. & Moonen, J. R. Endothelial Plasticity: Shifting Phenotypes through Force Feedback. *Stem Cells Int* **2016**, 9762959 (2016).

31. Nivedita, N., Ligrani, P. & Papautsky, I. Dean Flow Dynamics in Low-Aspect Ratio Spiral Microchannels. *Sci Rep* **7**, 44072 (2017).

32. Grigoryan, B. *et al.* Multivascular networks and functional intravascular topologies within biocompatible hydrogels. *Science* **364**, 458–464 (2019).

33. Applegate, M. B. *et al.* Laser-based three-dimensional multiscale micropatterning of biocompatible hydrogels for customized tissue engineering scaffolds. *Proc. Natl. Acad. Sci. U. S. A.* **112**, 12052–7 (2015).

34. Zheng, Y. *et al.* In vitro microvessels for the study of angiogenesis and thrombosis. *Proc. Natl. Acad. Sci. U. S. A.* **109**, 9342–7 (2012).

35. Roberts, M. A. *et al.* Stromal Cells in Dense Collagen Promote Cardiomyocyte and Microvascular Patterning in Engineered Human Heart Tissue. *Tissue Eng. Part A* **22**, 633–644 (2016).

36. Shiba, Y. *et al.* Human ES-cell-derived cardiomyocytes electrically couple and suppress arrhythmias in injured hearts. *Nature* **489**, 322–5 (2012).

37. Trapnell, C., Pachter, L. & Salzberg, S. L. TopHat: discovering splice junctions with RNA-Seq. *Bioinformatics* **25**, 1105–1111 (2009).

38. Robinson, M. D., McCarthy, D. J. & Smyth, G. K. edgeR: a Bioconductor package for differential expression analysis of digital gene expression data. *Bioinforma. Oxf. Engl.* **26**, 139–140 (2010).

39. Chen, E. Y. *et al.* Enrichr: interactive and collaborative HTML5 gene list enrichment analysis tool. *BMC Bioinformatics* **14**, 128 (2013).

40. Yu, G., Wang, L.-G., Han, Y. & He, Q.-Y. clusterProfiler: an R Package for Comparing Biological Themes Among Gene Clusters. *OMICS J. Integr. Biol.* **16**, 284–287 (2012).

41. Kanehisa, M., Furumichi, M., Tanabe, M., Sato, Y. & Morishima, K. KEGG: new perspectives on genomes, pathways, diseases and drugs. *Nucleic Acids Res.* **45**, D353–D361 (2017).

42. Slenter, D. N. *et al.* WikiPathways: a multifaceted pathway database bridging metabolomics to other omics research. *Nucleic Acids Res.* **46**, D661–D667 (2018).

43. Young, M. D., Wakefield, M. J., Smyth, G. K. & Oshlack, A. Gene ontology analysis for RNA-seq: accounting for selection bias. *Genome Biol.* **11**, R14 (2010).

44. Qiu, X. *et al.* Reversed graph embedding resolves complex single-cell trajectories. *Nat. Methods* **14**, 979–982 (2017).

45. Becht, E. *et al.* Dimensionality reduction for visualizing single-cell data using UMAP. *Nat. Biotechnol.* (2018) doi:10.1038/nbt.4314.

46. Nakajima, H. & Mochizuki, N. Flow pattern-dependent endothelial cell responses through transcriptional regulation. *Cell Cycle* **16**, 1893–1901 (2017).

47. De Val, S. & Black, B. L. Transcriptional control of endothelial cell development. *Dev Cell* **16**, 180–95 (2009).
48. Simons, M. & Eichmann, A. Molecular Controls of Arterial Morphogenesis. *Circ Res* **116**, 1712–1724 (2015).
49. Cozzi, V. *et al.* PTX3 as a potential endothelial dysfunction biomarker for severity of preeclampsia and IUGR. *Placenta* **33**, 1039–44 (2012).
50. Schneller Doris *et al.* Cytokine-Like 1 Is a Novel Proangiogenic Factor Secreted by and Mediating Functions of Endothelial Progenitor Cells. *Circ. Res.* **124**, 243–255 (2019).
51. McDonald, A. I. *et al.* Endothelial Regeneration of Large Vessels Is a Biphasic Process Driven by Local Cells with Distinct Proliferative Capacities. *Cell Stem Cell* **23**, 210-225.e6 (2018).
52. Evellin, S. *et al.* FOSL1 controls the assembly of endothelial cells into capillary tubes by direct repression of αv and β3 integrin transcription. *Mol. Cell. Biol.* **33**, 1198–1209 (2013).
53. Trapnell, C. *et al.* The dynamics and regulators of cell fate decisions are revealed by pseudotemporal ordering of single cells. *Nat. Biotechnol.* **32**, 381–386 (2014).
54. Fang, J. S. *et al.* Shear-induced Notch-Cx37-p27 axis arrests endothelial cell cycle to enable arterial specification. *Nat. Commun.* **8**, 2149 (2017).
55. Mack, J. J. *et al.* NOTCH1 is a mechanosensor in adult arteries. *Nat. Commun.* **8**, 1620 (2017).
56. Sundlisaeter, E. *et al.* The alarmin IL-33 is a notch target in quiescent endothelial cells. *Am. J. Pathol.* **181**, 1099–1111 (2012).
57. Zhang, B. *et al.* Biodegradable scaffold with built-in vasculature for organ-on-a-chip engineering and direct surgical anastomosis. *Nat. Mater.* **15**, 669–678 (2016).
58. Miller, J. S. *et al.* Rapid casting of patterned vascular networks for perfusable engineered three-dimensional tissues. *Nat. Mater.* **11**, 768–74 (2012).
59. Hoefer, I. E., den Adel, B. & Daemen, M. J. A. P. Biomechanical factors as triggers of vascular growth. *Cardiovasc. Res.* **99**, 276–283 (2013).
60. Sforza, D. M., Putman, C. M. & Cebral, J. R. Hemodynamics of Cerebral Aneurysms. *Annu. Rev. Fluid Mech.* **41**, 91–107 (2009).
61. Cebral, J. R. *et al.* Characterization of Cerebral Aneurysms for Assessing Risk of Rupture By Using Patient-Specific Computational Hemodynamics Models. *Am. J. Neuroradiol.* **26**, 2550–2559 (2005).
62. Sheinberg, D. *et al.* Endothelial dysfunction in cerebral aneurysms. *Neurosurg. Focus* **47**, E3 (2019).
63. Xiang, J. *et al.* Hemodynamic-Morphologic Discriminants for Intracranial Aneurysm Rupture. *Stroke J. Cereb. Circ.* **42**, 144–152 (2011).
64. Meng, H., Tutino, V. M., Xiang, J. & Siddiqui, A. High WSS or Low WSS? Complex Interactions of Hemodynamics with Intracranial Aneurysm Initiation, Growth, and Rupture: Toward a Unifying Hypothesis. *Am. J. Neuroradiol.* **35**, 1254–1262 (2014).
65. Dolan, J. M., Sim, F. J., Meng, H. & Kolega, J. Endothelial cells express a unique transcriptional profile under very high wall shear stress known to induce expansive arterial remodeling. *Am. J. Physiol. Cell Physiol.* **302**, C1109-1118 (2012).
66. Dolan, J. M., Kolega, J. & Meng, H. High wall shear stress and spatial gradients in vascular pathology: a review. *Ann Biomed Eng* **41**, 1411–27 (2013).
67. Amaya, R., Cancel, L. M. & Tarbell, J. M. Interaction between the Stress Phase Angle (SPA) and the Oscillatory Shear Index (OSI) Affects Endothelial Cell Gene Expression. *PLOS ONE* **11**, e0166569 (2016).
68. Aoki, T. *et al.* Sustained expression of MCP-1 by low wall shear stress loading concomitant with turbulent flow on endothelial cells of intracranial aneurysm. *Acta Neuropathol. Commun.* **4**, 1–14 (2016).

69. Wang, Y. *et al.* Mouse models of intracranial aneurysm. *Brain Pathol. Zurich Switz.* **25**, 237–247 (2015).
70. Chivukula, V. K. *et al.* Reconstructing patient-specific cerebral aneurysm vasculature for in vitro investigations and treatment efficacy assessments. *J. Clin. Neurosci. Off. J. Neurosurg. Soc. Australas.* **61**, 153–159 (2019).
71. Liu, Y. *et al.* Fabrication of cerebral aneurysm simulator with a desktop 3D printer. *Sci. Rep.* **7**, (2017).
72. Levitt, M. R. *et al.* Computational fluid dynamics of cerebral aneurysm coiling using high-resolution and high-energy synchrotron X-ray microtomography: comparison with the homogeneous porous medium approach. *J. NeuroInterventional Surg.* **9**, 00–00 (2017).
73. Ho, W. H., Tshimanga, I. J., Ngoepe, M. N., Jermy, M. C. & Geoghegan, P. H. Evaluation of a Desktop 3D Printed Rigid Refractive-Indexed-Matched Flow Phantom for PIV Measurements on Cerebral Aneurysms. *Cardiovasc. Eng. Technol.* **11**, 14–23 (2020).
74. Kaneko, N. *et al.* A patient-specific intracranial aneurysm model with endothelial lining: a novel in vitro approach to bridge the gap between biology and flow dynamics. *J. NeuroInterventional Surg.* **10**, 306–309 (2018).
75. Dolan, J. M., Meng, H., Singh, S., Paluch, R. & Kolega, J. High Fluid Shear Stress and Spatial Shear Stress Gradients Affect Endothelial Proliferation, Survival, and Alignment. *Ann. Biomed. Eng.* **39**, 1620–1631 (2011).
76. Mannino, R. G. *et al.* “Do-it-yourself in vitro vasculature that recapitulates in vivo geometries for investigating endothelial-blood cell interactions”. *Sci. Rep.* **5**, 1–12 (2015).
77. O’Keeffe, L. M., Muir, G., Piterina, A. V. & McGloughlin, T. Vascular Cell Adhesion Molecule-1 Expression in Endothelial Cells Exposed to Physiological Coronary Wall Shear Stresses. *J. Biomech. Eng.* **131**, (2009).
78. Kallmann, B. A. *et al.* Cytokine-induced modulation of cellular adhesion to human cerebral endothelial cells is mediated by soluble vascular cell adhesion molecule-1. *Brain* **123**, 687–697 (2000).
79. Pfenniger, A. *et al.* Shear stress modulates the expression of the atheroprotective protein Cx37 in endothelial cells. *J. Mol. Cell. Cardiol.* **53**, 299–309 (2012).
80. Boo, Y. C. *et al.* Shear stress stimulates phosphorylation of endothelial nitric-oxide synthase at Ser1179 by Akt-independent mechanisms: role of protein kinase A. *J. Biol. Chem.* **277**, 3388–3396 (2002).
81. Hohberg, M. *et al.* Expression of ADAMTS1 in endothelial cells is induced by shear stress and suppressed in sprouting capillaries. *J. Cell. Physiol.* **226**, 350–361 (2011).
82. Moffitt, J. R. *et al.* High-performance multiplexed fluorescence in situ hybridization in culture and tissue with matrix imprinting and clearing. *Proc. Natl. Acad. Sci.* **113**, 14456–14461 (2016).
83. Ganguli, A. *et al.* Pixelated spatial gene expression analysis from tissue. *Nat. Commun.* **9**, 1–9 (2018).
84. Starke, R. M. *et al.* Vascular smooth muscle cells in cerebral aneurysm pathogenesis. *Transl. Stroke Res.* **5**, 338–346 (2014).
85. Sanchez, M. *et al.* Intracranial Aneurysmal Pulsatility as a New Individual Criterion for Rupture Risk Evaluation: Biomechanical and Numeric Approach (IRRAs Project). *Am. J. Neuroradiol.* **35**, 1765–1771 (2014).
86. Moretti, M., Prina-Mello, A., Reid, A. J., Barron, V. & Prendergast, P. J. Endothelial cell alignment on cyclically-stretched silicone surfaces. *J. Mater. Sci. Mater. Med.* **15**, 1159–1164 (2004).
87. Halka, A. T. *et al.* The effects of stretch on vascular smooth muscle cell phenotype in vitro. *Cardiovasc. Pathol.* **17**, 98–102 (2008).

4. Chapter 4: The endothelial response to pressure

Abstract

Blood flow in the vasculature is a key driver of endothelial cell function, but a fundamental understanding of how the different hemodynamic forces interact to form a coherent endothelial response remains elusive. In particular, the role of pressure in flow sensing and vascular remodeling, despite its association with vascular diseases like hypertension, is poorly understood. Here we develop in vitro model systems to probe the effect of pressure conditions on the endothelial cell shear response as well as vascular remodeling in 3D. First, using hemodynamic conditions associated with pulmonary arterial hypertension we show that pressure conditions can alter the morphology and density of endothelial cells and that the transcriptional profiles of cells also shift under different pressure loads. High pressure conditions interfere with shear induced flow alignment and can result in increased cell density reminiscent of disease. RNA-sequencing results show that different pressure loads are associated with unique transcriptional transitions at different shear stress levels. By extending our model to a 3D system we also show that pressure conditions associated with early vascular development can bias the vascular remodeling of self-assembled vascular networks. We observe that high pressure conditions are associated with vascular regression and pruning, while low pressure conditions promote the vessel density and interconnectivity. Taken together our results highlight the need for an integrative and holistic view of endothelial cell mechanotransduction that incorporates pressure induced effects.

4.1 Pressure and shear interactions in endothelial cells

4.1.1 Introduction

One of the unique features of the spiral vessels developed in the previous chapter was their relatively long length (> 6 cm). As a result of this length and their comparatively small diameter, a not insignificant drop in transmural pressure developed from the inlet to the outlet. We noticed cells in the inlet and outlet regions appeared morphologically different when we changed the flow rate, despite there being no difference in shear stress between the two locations. With higher levels of shear stress the difference in pressure from the inlet to the outlet grew larger and the cells in the inlet (cells under higher pressure) were generally smaller and were less aligned with the direction of flow than cells in the low-pressure outlet (Appendix B). Motivated by this observation we were interested in exploring what effect pressure had on the endothelial response to flow.

Under normal conditions in the vasculature endothelial cells are subject to shear stress in the direction of blood flow, mechanical stretch circumferentially around the blood vessel, and hydrostatic pressure normal to the endothelial surface. Shear forces have been the dominant variable in EC mechanobiology studies,[1] with additional research into cyclic mechanical stretch,[2] but considerably less research attention devoted pressure loads. As a result, the effect of pressure on ECs is less well understood than shear stress and even less is known about how shear and pressure forces interact to guide signaling in ECs.

Work over several decades has shown that endothelial cells respond to changes in hydrostatic pressure loading. Long term culture of ECs in elevated pressure has been shown to induce basic fibroblast growth factor release[3] and can increase cell stiffness by promoting cortical actin density.[4] Human umbilical vein endothelial cells (HUVEC) exposed to as little as 4 cm H_2O of hydrostatic pressure were more proliferative than those under standard culture conditions (~0.2 cm H_2O) after just 24 hours and this effect could be blocked using α_v integrin antagonists.[5] Others have shown that physiologic levels of pressure can make EC monolayers more resistant to calcium-depletion induced damage to intercellular junctions.[6] ECs also respond to changes in acute pressure loading. Within 1 hour of applying a 100 mmHg load to cells, EC cortical stiffness significantly increases through myosin activation mediated by mechanosensitive ion channels.[4] Importantly, however, almost no published work has explored if these responses to hydrostatic pressure are maintained or altered when shear stress is applied simultaneously.

Interest in the effect of different pressure conditions on endothelial cells is driven not only by a desire to more fully define the mechanisms of endothelial mechanosensing, but also to explore its role in pathology. High blood pressure is one of the largest drivers of cardiovascular disease and it is prevalent in an increasingly large fraction of the global population,[7] yet the direct consequences of this altered load on the endothelium remain poorly understood. In pulmonary arterial hypertension (PAH), endothelial cells and endothelial dysfunction are thought to be major contributors to the development and progression of disease.[8] PAH is defined by a resting mean pulmonary artery pressure of more than 25 mmHg and can ultimately lead to right heart failure.[9] The increase in pressure is thought to arise from the loss of small pulmonary arteries, which contributes to an increase in vascular resistance and concomitant increase in pressure. The damaged pulmonary endothelium is then unable to repair itself through normal vascular remodeling and angiogenic pathways, and further endothelial dysfunction can follow.[8] The role of the hemodynamic increase in pressure on endothelial cell transcription and ultimately function is not well understood.

From these observations we sought to determine the effect of different physiologic pressure conditions on human pulmonary endothelial cells that were also challenged with applied shear stress. To investigate this question, we designed a microfluidic system to control the both pressure and shear conditions on endothelial cells while also enabling the collection of these cell populations for RNA sequencing. We showed that pressure conditions can alter the shape and alignment of endothelial cells under perfusion and characterized the transcriptional response of ECs to physiological pressures across multiple shear stress levels. Insight from these observations provides a fuller picture of how endothelial cells integrate multiple mechanical cues and how pathological pressure conditions shape endothelial transcription.

4.1.2 Methods

Microfluidic channel design and fabrication

In order to vary the pressure and flow conditions the experimental perfusion setup was designed as a combination of multiple microfluidic channels where one device would serve as a channel for culturing cells and additional downstream channels would act as resistors that increase pressure in the culture channel. For cell culture, a single channel (w = 500 μm, h = 100 μm, L = 20 mm) with higher aspect ratio was designed to minimize edge effects and provide space for the culture of ~5000 cells. Resistance channels (w = 100 μm, h = 100 μm) were designed to provide 20 mmHg or 60 mmHg of resistance at flow rates corresponding to a shear stress of 5, 10, and 20 dyne/cm^2 in the culture channels. Shear stress for rectangular channels was estimated by equation (1):

$$\tau = \frac{6Q\mu}{h^2 w} \tag{1}$$

Where Q is the volumetric flow rate, μ is the viscosity, h is the channel height, and w is the channel width. The pressure drop in all channels was estimated by equation (2):

$$\Delta P = \frac{16\pi^2 \mu Q J L}{(hw)^2} \tag{2}$$

Where L is the length of the channel and J is the polar moment of inertia for a rectangular cross-section:

$$J = \frac{hw(h^2 + w^2)}{12} \tag{3}$$

Microfluidic channels following these guidelines were designed using LayoutEditor (juspertor GmbH) and fabricated in silicon using standard lithography techniques. Briefly, chrome masks of various channel designs were exposed on a DWL 66+ (Hiedelberg GmbH) and chromium etched. Silicon wafers were spin coated with AZ9260 (Microchem, thickness ≈ 6 μm), exposed using a contact aligner and chrome masks (ABM), and developed with AZ400K (Microchem). Patterned wafers were then subject to deep reactive ion etching (SPTS Rapier DRIE) before the resist was stripped (EKC, Dupont) and the final channel dimensions were measured optically (Keyence VK-X150K) and physically (KLA Tencor P15 Contact Profilometer).

To transfer the finished patterns to PDMS, silicon wafers were then silanized with trichloro(3,3,3-trifluoropropyl) silane (Sigma) and a 10:1 mixture of PDMS base and curing agent (Sylgard 184, Dow) was poured over the wafer. PDMS was cured at 65 °C for at least 3 hours before separating into individual channels and punching inlet and outlet holes with a 2 mm biopsy punch (Integra Miltex). Patterned PDMS channels were then bonded to either cover glass (Thorlabs #1.5) or plain glass slides (Fisher Scientific) using air plasma (Power = 75 W, Plasma Etch) and annealed at 65 °C for at least 1 hour.

Resistor pressure validation

To validate the hemodynamic properties of fabricated channels we constructed a flow circuit driven by a syringe pump (KD Scientific). Syringes were connected in series to a microfluidic flow sensor (Elveflow MFS-80), a bare PDMS culture channel, a microfluidic pressure sensor

(Elveflow MPS-1), and bare PDMS resistors of different lengths. Perfusion media (EGM2 + 3.5% dextran) was loaded into syringes and run through the flow circuit. Steady-state values for flow rate and pressure were recorded using an Elveflow controller (Elveflow OBS).

Channel Seeding and Culture

Prior to cell culture, channels were sterilized by 30 minutes of UV exposure. Channels for cell culture were coated with human fibronectin (5 µg/mL) for 1 hour at 37 °C in a cell culture incubator. Channels were then rinsed with fresh culture medium (EGM2, Lonza) and seeded with human umbilical vein endothelial cells (HUVEC, Lonza), or human pulmonary artery endothelial cells (HPAEC, Lonza) by perfusion of 10 µL of a 4 million cells/mL suspension. Cells were seeded for 1 hour at 37 °C before rinsing channels with fresh media to remove unattached cells. Attached cells in the inlet and outlet reservoir were then removed by scraping the glass surface of these regions with a gel loading pipette tip attached to a vacuum aspirator, leaving cells present only in the channel cross-section. An empty filtered P1000 pipette tip was placed on the outlet and a filtered P1000 pipette tip filled with 400 µL of culture medium was placed on the inlet and allowed to equilibrate overnight in an incubator.

Channel Perfusion

The medium for perfusion consisted of normal culture medium supplemented with 3.5% dextran to more closely mimic the viscosity of blood (~3.5 cP). Perfusion media was degassed by placing under vacuum for 30 minutes, used to fill syringes (10 mL syringes for 5 dyne/cm^2 flow, 30 mL syringes for 10 and 20 dyne/cm^2 flow) and then placed on a syringe pump (KD Scientific). Syringes were connected in series to culture channels with 1/32” ID PTFE tubing (Elveflow) and then to resistor channels with 1/32” ID Tygon tubing (Cole-Parmer) and finally 50 mL conical tube collection reservoirs with 1/16” ID Tygon tubing (Cole-Parmer). The flow rate was set to match the shear stress of the experiment and channels were perfused for 24 hours. Parameters for flow and resistor values are listed in Table 4.1.1.

Table 4.1.1 Parameters for channel perfusion

Shear Stress ($dyne/cm^2$)	**Flow Rate (µL/min)**	**20 mmHg Resistor Length (mm)**	**60 mmHg Resistor Length (mm)**
5	8.96	22	72
10	17.92	11.5	36
20	35.84	5	17.5

Immunofluorescent staining and imaging

For imaging, culture channels were disconnected from the syringe pump at 24 hours and immediately perfused with 250 µL of 4% paraformaldehyde for 10 minutes prior to washing with PBS (3 x 5 min). For staining channels were first blocked and permeabilized with solutions of 2% BSA and 0.5% Triton X-100 in PBS for 30 minutes. Channels were incubated with primary antibodies for 1 hour at room temperature or overnight at 4 °C and washed with PBS. Secondary antibodies, conjugated primary antibodies, as well as actin and nuclear stains were added for 1 hour at room temperature before washing with PBS. Stained channels were imaged with a widefield microscope (Nikon Eclipse Ti2) as well as a line scanning confocal system (Nikon A1R). Primary antibodies included: VECAD/CD144 (1:100, Abcam ab33168), AQP-1 (1:100, Santa Cruz sc-25287), GJA4 (1:100, Abcam ab181701), DLL4 (1:100, Novus NB600-892), Ki67 (1:100, Abcam ab16667), Notch1-ICD (1:100, Cell Signaling 3608S). Secondary antibodies, conjugated primary antibodies, and other stains included: Notch1-ECD (1:100, BD 566023), DLL1 (1:50, Biolegend 346403), VECAD/CD144 (1:100, eBioscience 17-1449-42), Alexa Fluor goat anti-rabbit 647 (1:100, Thermo Fisher A-21235), Alexa Fluor goat anti-mouse

568 (1:100, Thermo Fisher A-11004), Alexa Fluor Phalloidin 488, 568, and 647 (1:100, Thermo Fisher Scientific, 488:A12379, 568:A12380, 647:A22287), and Hoescht 33342.

Image analysis

Images of channels were processed using Fiji [10]. For cell morphology analysis, maximum intensity projections of Z-stacks of cells adhered to the glass surface were used to draw cell borders from junctional or actin stains. From these outlines, cell size, perimeter, angle, and shape descriptors were calculated and exported as csv files for analysis in R. The orientation of a cell was determined using the fit ellipse function to identify its major and minor axis and the cell angle was defined as the angle between the flow direction (0 degrees) and the cell's major axis. A minimum of 3 40x fields of view were analyzed for each channel, with at least 50 cells identified across the 3 fields. Nuclear counts were obtained from the same sets of images by thresholding out the Hoescht signal from the background and utilizing the "Analyze Particles" function in Fiji to generate counts. Ki67 positive nuclei were manually counted and used to determine the percentage of Ki67 positive nuclei. Individual cell parameters (e.g. area, angle, etc.) were compared based on pressure condition using an unpaired two-sided Wilcoxon Rank Sum test and considered significantly different when $p < 0.05$. To compare nuclei counts and the ratio of Ki67 positive nuclei, the values from the 3 fields of each channel were first averaged to generate a single value for each channel replicate ($n = 3$ channels). The channel replicates were then compared using an unpaired two-sided Student's t-test and considered significant when $p < 0.05$.

RNA Isolation and RNA-Seq

After 24 hours of flow channels were disconnected from the syringe pump and a representative brightfield image was taken. 350 μL of lysis buffer (RLT + 1% β-mercaptoethanol, Qiagen) was then perfused through each channel and RNA was isolated using a RNeasy Micro kit (Qiagen) with DNase treatment. Isolated RNA was then submitted to the Fred Hutchinson Genomics Resource for quality control, library preparation, and sequencing. RNA quality was evaluated using an Agilent Tapestation where all samples had RINe scores ≥ 9.7. Libraries were prepared from RNA samples using SMART-Seq v4 Ultra Low Input (Takara) and Nextera XT DNA Library Preparation (Illumina) kits. Samples were then sequenced on an Illumina NovaSeq 6000 (paired end, 50 bp).

RNA-Seq Data Analysis

RNA-Seq reads were aligned to hg38 using STAR[11] and counts were generated using the featureCounts function of the subRead package.[12] Quality control was performed using RSeQC [13] and differential expression analysis was performed using edgeR (3.28.1). [14] Genes were considered differentially expressed if the P value and FDR were ≤ 0.05 and the absolute value of the log fold change was ≥ 0.585. Gene ontology analysis and gene set enrichment analysis were performed using clusterProfiler[15] and Hallmark pathways were identified using the Molecular Signatures Database[16] with a P value and FDR cutoff of 0.05.

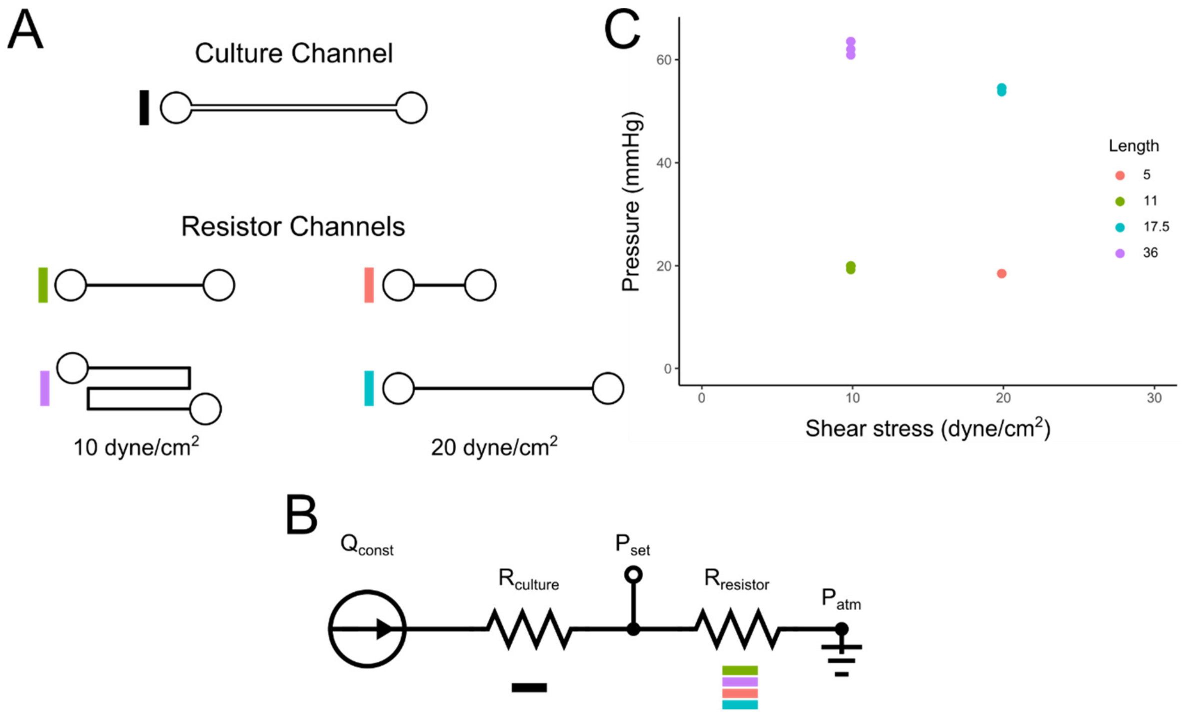

Figure 4.1.1 Microfluidic device design and validation. (A) Design of culture and resistor microfluidic channels and system schematic (B) for culture under constant flow. The flow rate (Q) is constant for a given shear stress condition and the setpoint pressure (P_{set}) was determined by the resistor channel used. The outlet for all experiments was open to the atmosphere ($P = P_{atm}$). Culture channels have a 112 µm x 500 µm cross-section and resistor channels have a 112 µm x 100 µm cross-section. (C) Measured pressure drop across resistor channels for a given shear stress condition in the culture channel.

4.1.3 Results

Channel validation

Etched silicon wafers were measured to have a channel depth of 112 µm and widths of 500 µm for culture channels and 100 µm for resistor channels by contact profilometry. The flow rate required to produce a wall shear stress of 5, 10, or 20 dyne/cm^2 was calculated using equation (1). Bonded PDMS channels (Figure 4.1.1A) connected to a syringe pump and various length resistor channels (Figure 4.1.1B) were perfused with 37 °C EGM2 supplemented with 3.5% dextran and pressure measurements were taken at flow rates corresponding to 10 and 20 dyne/cm^2 shear stress. Measured pressure values were within 5% of target values except for the 17.5 mm resistor, which was ~10% (54.5 mmHg) below the target 60 mmHg level at 20 dyne/cm^2 (Figure 4.1.1C).

Cell morphology varies under pressure conditions

Under low shear stress conditions, cells cultured under low and high pressure displayed different morphologies and orientations (Figure 4.1.2A, B). Under low pressure, cells were significantly larger (Figure 4.1.2C) and fewer nuclei were present per field (Figure 2D) than in high pressure conditions. Cells under low pressure were also significantly more aligned (Figure 4.1.2E), with cells primarily pointed and elongated in direction of fluid flow in the channel (Figure 4.1.2F). In contrast, cells under high pressure were significantly rounder (smaller aspect ratio) with a less clearly defined orientation that spanned a wider range of angles than cells in low pressure. Despite being under the same shear conditions, these cells often appeared to align orthogonal to the direction of flow (Figure 4.1.2A, D). While the number of nuclei was significantly higher in 60 mmHg conditions, the number of strongly Ki67 positive nuclei was greater in low pressure (9.3% ± 1.8 vs 2.9% ± 0.8) channels. The percentage of nuclei with detectable Ki67 staining was much greater and was not significantly different between groups (0 mmHg = 62.9 ± 4.5%, 60 mmHg = 63.6 ± 2.9%).

RNA Sequencing of channel under flow and pressure

To explore the transcriptional changes in endothelial cells under different hemodynamic conditions we performed RNA sequencing on channels under 5 and 10 dyne/cm^2 flow under three pressure conditions (Low = 0 mmHg, Med = 20 mmHg, High = 60 mmHg). To understand the baseline effect of culturing cells in channels we also included cells cultured in PDMS channels or in PDMS wells (~8 mm diameter) under a minimal hydrostatic load (~5 mm H_2O) with no bulk flow. Including all samples, principle component analysis showed separation of static samples from all samples under flow (Figure 4.1.3A) along the first principle component, but flow and pressure samples were tightly grouped. Reducing the dataset to only samples

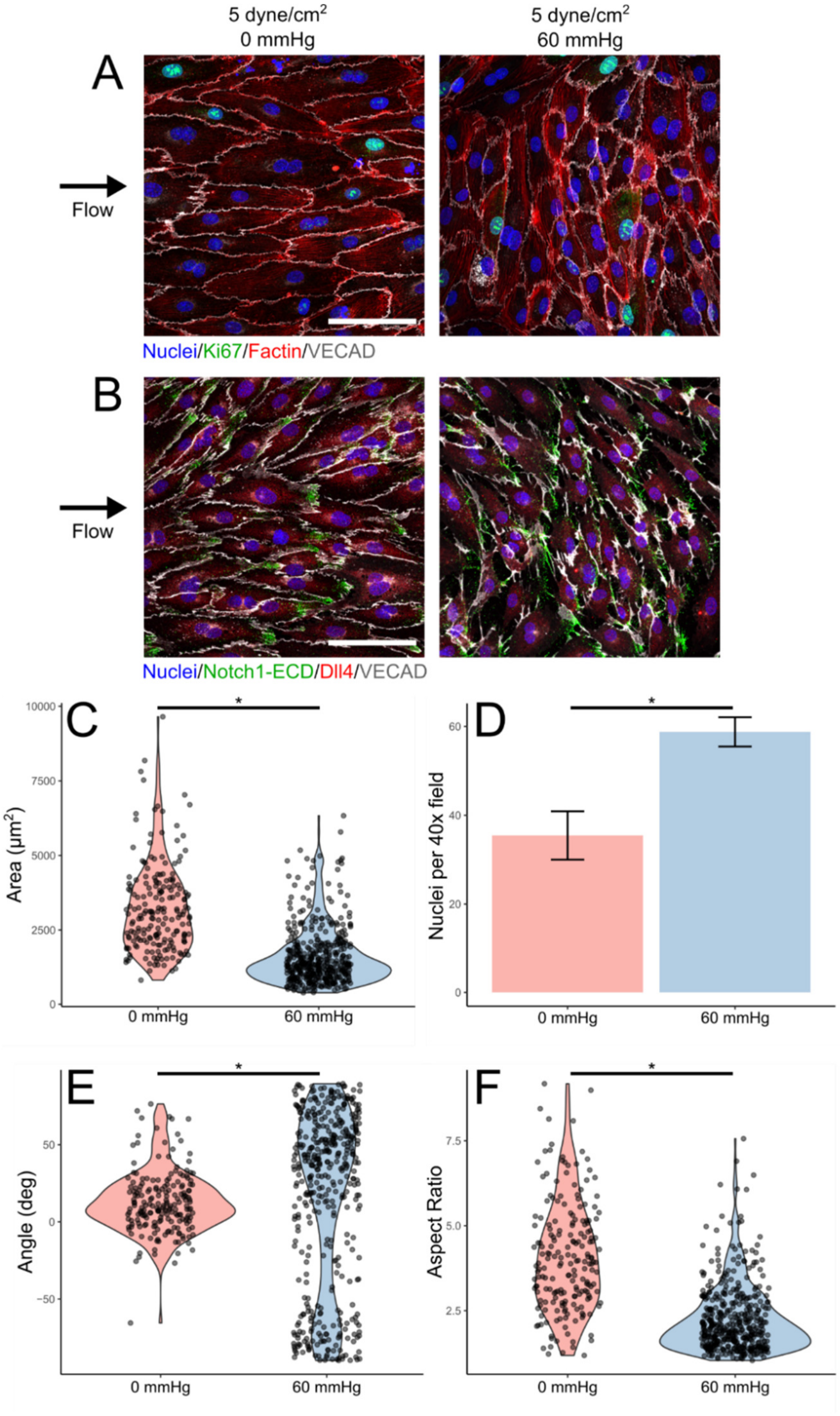

Figure 4.1.2. (A) Representative images of cells after 24 hours of 5 dyne/cm2 shear stress with 0 or 60 mmHg of pressure stained for nuclei (blue), Ki67 (green), F-actin (red), and VECAD (white). (B) Representative images of Notch1-ECD (green) and Dll4 (red) distribution in cells after 24 hours of flow. Violin plots of cell area (C), angle (E, flow direction = 0°), and aspect ratio (F, length of major axis/length of minor axis). Dots represent individual cells from 3 independent channels (> 50 cells per channel). Number of nuclei per 40x field of view (D) in different pressure conditions (n = 3 channels). Error bars represent 95% confidence interval. * $p < 0.05$ when compared by Wilcoxon Rank-Sum test or Student’s t-test. Scale bars = 100 µm.

under perfusion showed clustering of samples by flow rate along principle component 2 (Figure 4.1.3B), with a small trend of high-pressure groups more aligning along principle component 1. Similar trends appeared when the samples were subject to hierarchical clustering (Figure 4.1.3C), where the first branch separated perfused from unperfused samples. Further branches distinguished channel control samples from channel controls samples but did not cleanly cluster samples by shear stress or pressure conditions. Low- and High-pressure samples were more similar under 5 dyne/cm^2 conditions, but Medium pressure samples occupied a separate branch more similar to higher shear stress samples. Perfused samples at all pressure conditions showed upregulation of conventional markers of shear stress relative to statically cultured controls (Figure 4.1.3D). Differential expression analysis also revealed additional genes that had not been reported as shear responsive but increased with shear stress level (Figure 4.1.3E).

The confinement of endothelial cells led to significant expression changes when comparing channel and well controls, with 1927 genes differentially expressed between these two groups. Gene ontology (GO) analysis of these terms suggested channel confinement activated hypoxic programs, including significant changes to hypoxia associated genes like *ANGPTL4*, *HMOX1* and *HMOX2*, *CYP1A1*, *AQP1*. These were also associated with significant changes in genes associated with metabolism, with GO terms for alcohol, lipid, steroid, cholesterol, and other metabolic processes enriched in the list of significantly regulated transcripts.

The onset of flow lead to significant changes in relative to static controls in all pressure groups, but once at a given shear stress level the effect of changes in pressure were less well defined. Comparisons of the three pressure groups at 5 dyne/cm^2 flow showed Medium vs. High pressure groups had many more differentially expressed transcripts (1405 genes) than other combinations (Figure 4.1.4A, B), with the Low-pressure samples appearing to span these two

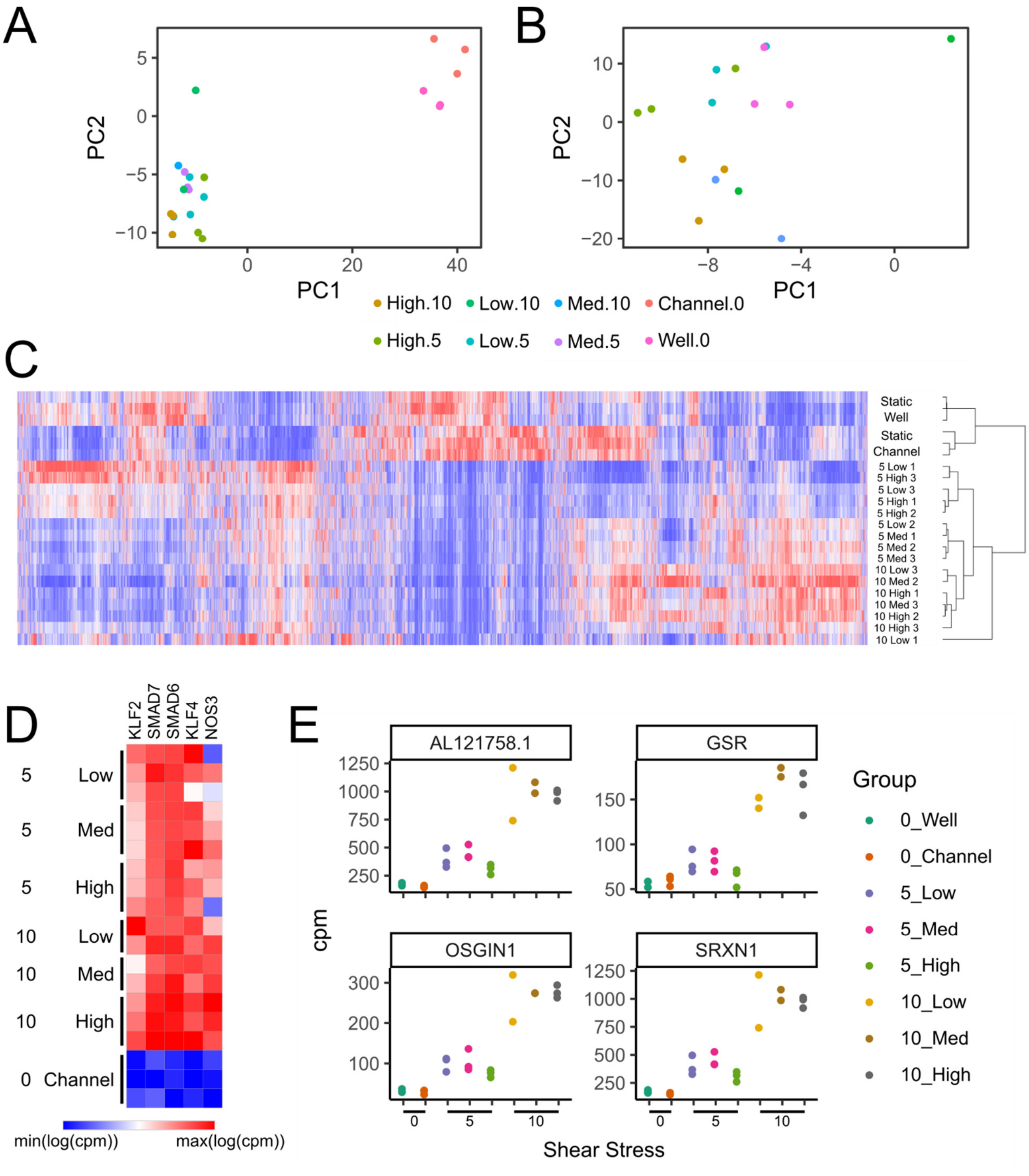

Figure 4.1.3 RNA sequencing sample trends. Principle component analysis of all samples (A) and samples under flow only (B). RNA-seq transcriptome heatmap with hierarchical clustering by sample type (C). Heatmap of representative endothelial flow-responsive genes (D). Additional unique flow responsive genes identified by RNA-seq with proportional response to shear stress conditions (E).

populations (PC1 in Figure 4.1.3B). No significantly regulated genes at this flow rate overlapped in all pressure varying comparisons. In the Medium vs High pressure comparison at 5 dyne/cm^2, GO analysis of upregulated and downregulated genes revealed several overrepresented GO biological process terms. Upregulated genes in this comparison were associated with a variety of protein membrane targeting pathways, including many genes coding for proteins of the 40S and 60S ribosomal subunits (Figure 4.1.4E). GO terms based on significantly downregulated genes included additional membrane targeting pathways as well as those for GTPase signal transduction and cell morphogenesis. At higher shear stress levels the differences between pressure conditions were less pronounced, with no differentially expressed genes identified between Medium and High pressure conditions at 10 dyne/cm^2 (Figure 4.1.4C). Low pressure samples at this shear stress level were more distinct from the Medium (76 genes) and High (255 genes) pressure conditions (Figure 4.1.4D), with some overlap in these comparisons (31 genes). Neither these overlapping genes, nor the genes in the Low vs Medium group were associated with any significant enrichment of specific GO terms. The Low vs High pressure comparison was associated with no enriched biological process terms but did contain several cell component terms related to cell-substrate junctions (e.g. *ITGA2*, *ACTN2*, *FERMT1*) and intermediate filaments (e.g. *KRT81*, *KRT19*, *KRT8*, *KRT15*, *KRT18*). By grouping cells by pressure condition only we identified an additional small subset of genes that were differentially expressed across pressure conditions (Figure 4.1.4F). This list included genes with endothelial ties including HES4,[17] SNAI2,[18] VLDLR,[19] and MBD2.[20]

We were also interested in exploring if pressure conditions alter the response to changes in shear stress in endothelial cells. For this we compared the differentially expressed genes in 5 vs 10 dyne/cm^2 shear stress under different pressure condition to understand if these transitions were altered by pressure (Figure 4.1.5A). Raising the shear stress from 5 to 10 dyne/cm2 resulted in the fewest differentially expressed genes in the transition at Low pressure

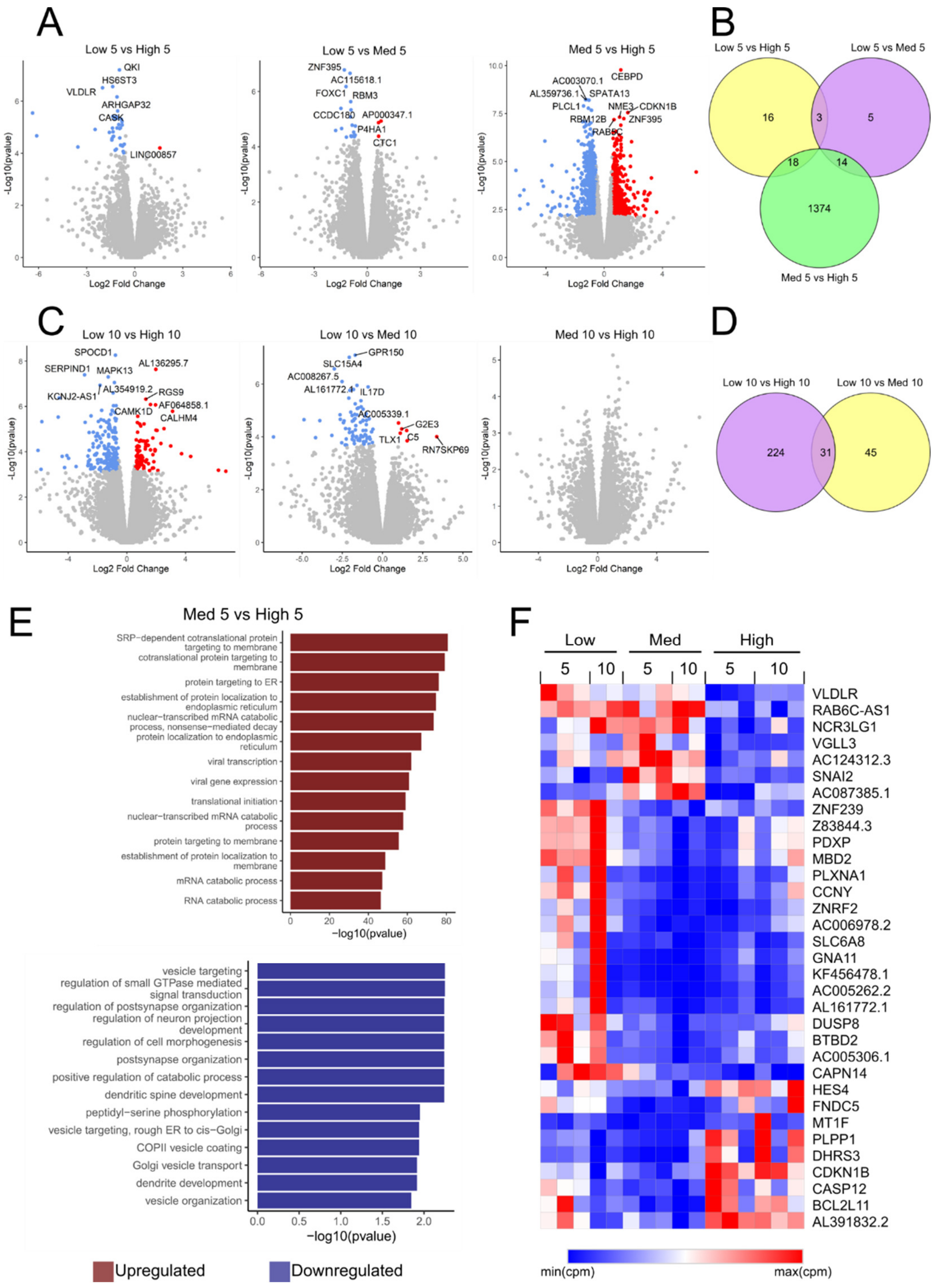

Figure 4.1.4 EC expression changes under variable pressure but constant shear stress. Volcano plots (A) and Venn diagram (B) of differentially expressed genes under different pressure conditions at 5 dyne/cm^2 shear stress. Volcano plots (C) and Venn diagram (D) of differentially expressed genes under different pressure conditions at 10 dyne/cm^2 shear stress. GO biological process terms associated with significantly upregulated and downregulated genes when comparing medium and high pressure conditions at 5 dyne/cm^2 shear stress (E). Genes identified as significantly altered by high pressure conditions when shear stress is not considered (F).

(205 genes) while almost ten times as many differentially expressed genes were present in High pressure (1977 genes, Figure 4.1.5B). Among these comparisons there was a small set of genes consistent to the flow transition in all pressure conditions (Figure 4.1.5C). These included genes that were differentially expressed by the initiation of flow, genes that progressively increased with increasing flow (e.g. *TRIM16*/*TRIM16L*, *GPR17*, *OSGIN1*, *SRXN1,* etc.) and others that dropped under moderate flow but were activated by higher flow. This list was associated with GO biological process terms for oxidative stress response. The flow transition under Low and Medium pressure did not have significant GO terms except for upregulated Medium pressure genes, which were associated with proliferative terms like regulation of nuclear division and chromosome segregation. In the High pressure transition many more genes were uniquely differentially expressed. In this set, GO analysis for upregulated genes included biological process terms for GTPase and RAS signal transduction as well as cytoskeletal organization (Figure 4.1.5D). Downregulated terms were related to mitochondrial processes and membrane targeting and other processes.

4.1.4 Discussion

While the effect of the component forces of blood flow (shear stress, hydrostatic pressure, mechanical stretch) on endothelial cells in normal physiology have been studied independently, relatively little work has investigated the transcriptional response of endothelial cells to combinations of these forces in vitro. Here we challenged human pulmonary artery endothelial cells with shear stress and normal and pathologic pressure conditions and investigated their morphologic and transcriptional response.

Under 5 dyne/cm^2 shear stress we found that pressure conditions could dramatically alter the shape and orientation of HPAEC. Under Low pressure conditions ECs responded as expected, forming defined intercellular junctions, elongating and flattening in the direction of flow,[21] and displaying clustering of the Notch1-ECD at the downstream pole of the cell.[22] At the

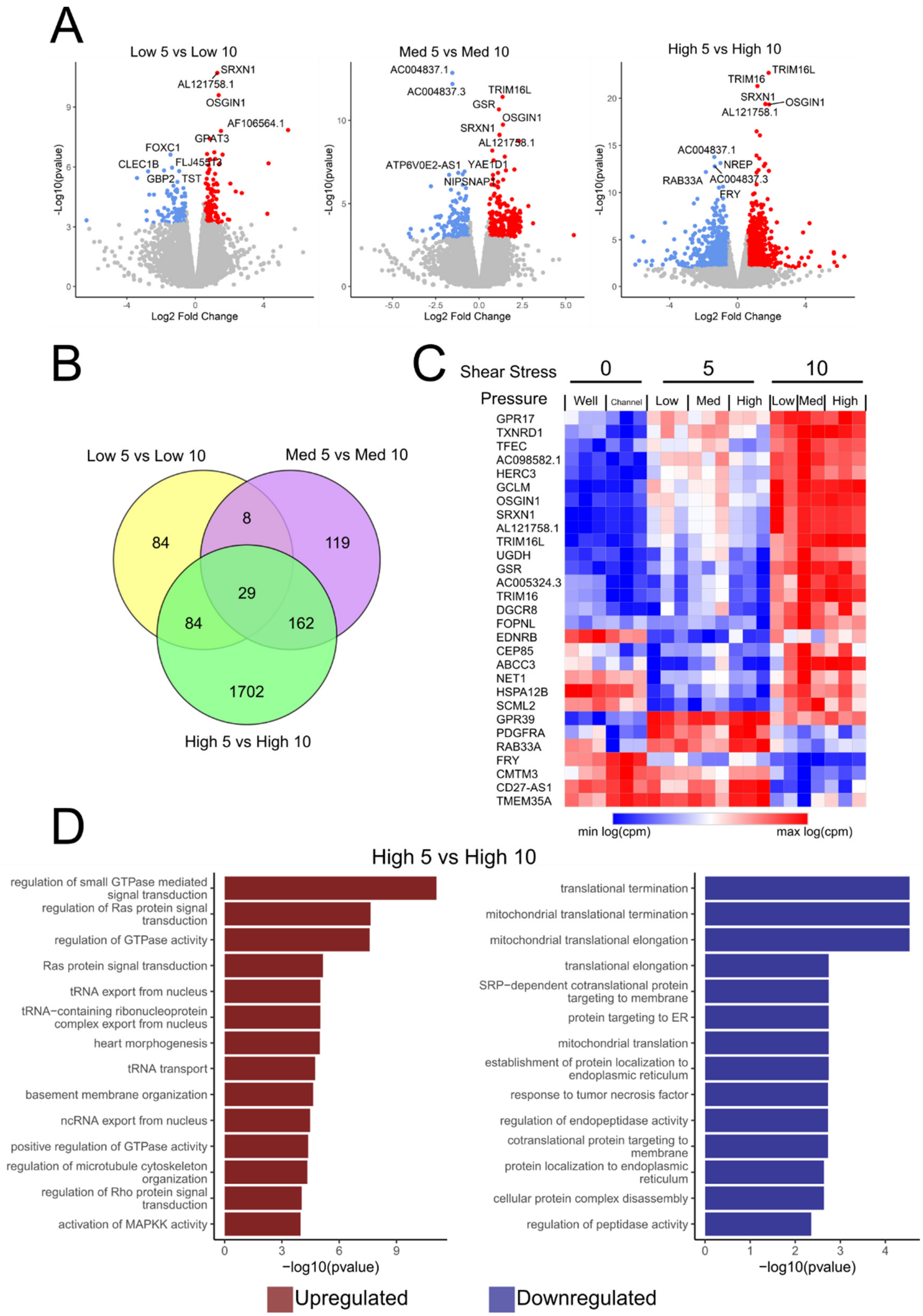

Figure 4.1.5 EC response to changes in shear stress under different pressure conditions. Volcano plots (A) and Venn diagram (B) of differentially expressed genes when shear stress is raised from 5 to 10 dyne/cm^2 under different pressure conditions. Heatmap of genes that are differentially regulated in all comparisons (C). GO terms for differentially expressed genes in the transition from 5 to 10 dyne/cm^2 under high pressure (D).

same shear stress but higher pressure, ECs reversed these morphologic trends appearing smaller and oriented perpendicular to the direction of flow. Unlike previous reports where the polarization of Notch1-ECD was strongly associated with the orientation of the cell in the direction of flow,[23] High pressure conditions instead led to Notch1-ECD accumulation on the downstream edge of the cell's short axis. This observation provides additional support for an integrative view of endothelial mechanosensing[24] as it provides evidence that pressure signaling mechanisms can dominate over shear-sensing pathways in certain physiologic conditions. Work performed with exclusively hydrostatic loads has indicated that pressure sensing occurs through ion channels, with strong evidence for the epithelial sodium channel (ENaC) acting as a major mechanosensor.[4] Inhibition of ENaC while cells are under flow and pressure with amiloride[25] would provide valuable insight into this interaction.

In these flow conditions we also noticed a significant difference in endothelial cell number suggesting more proliferation had occurred over the perfusion period in high pressure conditions. Counterintuitively, when we stained these cells for the proliferative marker Ki67, a larger fraction of cells was strongly positive in the Low pressure condition than the High pressure condition. The greater density of cells in High pressure would suggest that interrogating cells at an earlier timepoint or utilizing a BrdU assay[26] as a measure of proliferation would show a different pattern than what is observed at 24 hours. The contact inhibition of proliferation in endothelial cells[27] would also support this view that proliferation slowed after an initial burst in density in High pressure conditions. This endothelial overgrowth also correlates with the existence of plexiform lesions formed by proliferative endothelial cells that are a characteristic feature of pulmonary hypertension.[28]

In the RNA sequencing data, we observed clear differences between static conditions and all perfused groups with the upregulation of hallmark shear-sensitive factors like KLF2, SMAD6, SMAD7, and NOS3.[29] When comparing groups under the same shear stress, but different pressure the results were more difficult to interpret. At 5 dyne/cm^2 High and Medium pressure conditions appeared distinct from one another with differences characterized by GO terms like GTPase signal transduction, and changes to protein membrane targeting genes. The Low pressure condition, however, seemed to sit between these two groups, with few significantly regulated genes between either Medium or High pressure conditions. When the shear stress was raised to 10 dyne/cm^2 the differences between the Medium and High pressure groups disappeared. This observation may also support an integrative view of mechanosensing as the effect of raising the shear force while maintaining the pressure levels at a constant value would be to minimize the contribution of pressure and make Medium and High pressure conditions more similar to one another. By comparing the difference between these two groups and the Low pressure condition at 10 dyne/cm^2 we did observe this effect as there was appreciable overlap in these differentially regulated genes (~40% of Low vs Medium genes). When we regrouped and compared samples under perfusion only by pressure condition, we found a smaller set of genes that had several associations with endothelial pathways. Of these *SNAI2* was particularly interesting as it is recognized as a regulator of pulmonary hypertension severity in animal models[30] and contributes to the endothelial-to-mesenchymal transition prevalent in PAH.[31]

We also investigated the changes that occur when the shear stress is raised from 5 to 10 dyne/cm^2 under different pressure conditions. Among the three pressure levels there was a small conserved set of genes that were associated with GO terms for oxidative stress which has known shear sensitive links.[32] When comparing the gene set differences by pressure condition, however, many more genes were differentially expressed when the flow was raised in High pressure conditions. The genes unique to this High pressure group showed enrichment for Rho, Rac, and small GTPase GO terms. These are particularly interesting due to the importance of Rho GTPases in endothelial biology, where they have been shown to regulate EC cell shape, barrier integrity,[33] and a variety of vascular developmental processes.[34] Many of these genes are downregulated in High pressure at 5 dyne/cm^2 including *GPR17*, *RASA3*, and *RASGRF2*. The incorporation of permeability measurements like trans-endothelial electrical resistance would provide insight into the effect of these on endothelial barrier function as it has been reported that pressures around 10 mmHg increase[6,35] permeability, while pressures around 100 mmHg decrease[4] permeability. Our observation that Rho signaling terms appear to vary with pressure condition could help explain this reported difference.

Taken together the morphological and transcriptional differences between ECs challenged with different pressure conditions while under shear stress are complex. Immunofluorescent imaging showed that cells had significantly different morphologies and appeared to have undergone considerable expansion while under High pressure. RNA-sequencing data, however, did not reflect these differences with enrichment of cytoskeletal or cell-cycling markers. It is possible that the 24-hour time point was too late to observe many of these changes and future studies are needed to probe the acute response (e.g. within 6 hours of flow initiation) to different hemodynamic conditions. The use of rectangular channels also contributes to cellular heterogeneity and a noisier transcriptional signal because the shear conditions for cells near the channel corners are significantly lower than the center of the channel.[36] The use of circular channels would eliminate this source of error, but culturing sufficient cells in appropriately sized vessels remains a technical challenge.

These limitations also reflect the relationship of these results to endothelial cells in PAH. While differences in cell density and the differential regulation of factors like *SNAI2* draw parallels to PAH, our results do not suggest that pressure conditions alone are sufficient to recapitulate the EC dysfunction seen in PAH. Instead these results may provide a solid foundation from which to compare the pressure response of healthy pulmonary ECs and patient derived PAH cells. Recent work has shown that mutations to *BMPR2* which are common in familial PAH[37] can alter the response of pulmonary ECs to flow,[38] suggesting their hemodynamic and pressure response should be further explored. The response of different diseased pulmonary populations is also a key point to consider as microvascular and arterial ECs have been observed to have different shear responses in animal models of PAH.[39]

A final limiting factor in the interpretation of these results is the lack of physiologic stretch present in the system. Previous research has shown that endothelial cells subject to physiologic strain align perpendicular to the direction of strain.[40] In a cylindrical blood under circumferential stretch this response would act to reinforce shear-induced alignment in the direction of flow. Because pressure and stretch are directly linked, increases in hydrostatic load that might tend to align cells circumferentially as seen in this study are likely attenuated by increases in stretch that drive flow-directional alignment in normal physiology. How these three loads are integrated remains undefined, but this research suggests that the relative magnitude of each force is essential when considering the ultimate cohesive endothelial response.

4.1.5 Conclusion

Endothelial cells experience a range of hemodynamic forces, but their response to combined pressure and shear loads is poorly understood. Here we developed a platform to expose endothelial cells to controlled shear and pressure conditions and showed that pressure can modify the morphologic and transcriptional response under different shear stress conditions. These results highlight the importance of non-shear forces on endothelial cells and suggest a more integrated view of mechanotransduction may provide new insights into EC biology.

4.2 Pressure Driven Vascular Remodeling

4.2.1 Introduction

While the microfluidic devices we have previously used to investigate pressure allow for excellent control of flow and pressure within a channel, they do so in a silicone and glass environment. The consequence of this is that endothelial cells under study are unable to remodel the microenvironment and unable to undergo angiogenesis and other processes that occur in 3D tissues. To understand the role of pressure in these 3D processes we next sought to investigate the effects of pressure on vascular remodeling.

A functional vasculature is an essential component in the development of engineered tissues. Without it, oxygen and nutrient diffusion limit the size of viable tissue.[41] In development, these limits are overcome as biophysical forces help guide the formation of dense hierarchical vascular networks. For example, interruptions to normal flow can prevent the conversion of the uniform vascular bed in the mouse yolk sac on embryonic day 8.5 to a hierarchical vascular tree on E9.5.[42] It's well accepted that hemodynamic forces[43,44] and a variety of other factors play key roles in shaping the vasculature *in vivo*.[45–47] While considerable attention has been given to the process of vascular development in the embryo,[43,48,49] little of this process is reproducible in vitro. The characteristic vascular remodeling of a capillary plexus that leads to a branching, hierarchical, vascular network has yet to be shown outside of the body. Hemodynamic forces like pressure gradients, shear stress, and interstitial flow, however, have been shown in several in vitro systems to regulate cellular alignment,[50,51] morphogenesis,[52] and angiogenesis.[53] Nonetheless, a fundamental understanding of the role of hemodynamic forces in vascular remodeling remains elusive and is partially attributed to the absence of in vitro models that undergo vascular remodeling. While considerable research has contributed to an understanding of the effect of shear forces, little is known about how pressure influences vascular remodeling in 3D matrices. Pressure, which varies in these in vivo networks may be an important cue to endothelial cells in the process of vascular remodeling.

To investigate the effect of pressure on remodeling, we developed an in vitro engineered vascular bed model. The vascular bed system consists of two perfusable endothelialized vessels with independent control of flow and pressure embedded in a collagen gel. One vessel is maintained at high pressure and the other at low pressure. Between these two vessels a self-assembled plexus is formed that can undergo remodeling based on pressure conditions. We showed that pressure gradients applied to 3D tissues can dramatically alter the structure of engineered vascular networks. These networks appear to regress where pressure is high and expand where pressure is low. These results suggest that the pressure may play a role in vascular patterning and remodeling and may contribute to the development of vascular hierarchy.

4.2.2 Methods

Cell culture

Human umbilical vein endothelial cells (HUVEC, Lonza) were cultured on gelatin coated (0.1%) tissue coated polystyrene (TCPS) in Endothelial Growth Media (EGM, Lonza). HUVEC were used between passages 4-6 for all experiments. GFP tagged HS27a were cultured directly on TCPS in RPMI 1640 (Invitrogen) supplemented with 10% Fetal Bovine Serum, 1% Pen/Strep, 2 mM L-glutamine, and 1mM Sodium Pyruvate.

“H” pattern device fabrication

For pressure studies molds were milled from poly(methyl methacrylate) (PMMA) such that they formed a raised H-shaped feature in a well. These molds were then used for casting polydimethylsiloxane (PDMS, Sylgard 184 Dow Corning). PDMS was made by mixing the base and curing agent in a 10:1 ratio and degassing the solution in a vacuum chamber. Degassed PDMS was then poured into the molds and cured for 3 hours at 65 °C. Once cured, the PDMS device containing a recessed “H” pattern was removed from the mold and the center “H” was removed using a 4 mm biopsy punch. Four 25 mm lengths of 23-gauge stainless steel hypodermic tubing (McMaster-Carr) were then inserted into the PDMS “H” device and this tubing and a glass coverslip were sealed using PDMS. After curing, the device was inverted and a small PDMS reservoir was also attached using PDMS and allowed to cure. The assembled device was loaded into a customized hard coat anodized aluminum holder and autoclaved (Figure 1B).

<u>“H” pattern construct assembly and culture</u>

Autoclaved “H” pattern devices were Corona treated for ~30 seconds before coating with 1% polyethylenimine (Sigma) for 10 minutes. Devices were rinsed three times with water before treating with 0.1% glutaraldehyde (Sigma) for 20 minutes. Devices were rinsed again three times with water and allowed to dry. Two acupuncture needles (Seirin, 250 μm diameter) were then threaded through the aligned hypodermic tubing. Type 1 rat tail collagen was mixed with sodium hydroxide, EGM, M199 10x supplement (10%), and cells to a final concentration of 6 mg/mL collagen. For all trials, HUVEC in the bulk were seeded at 2.5 million cells/mL. If included, HS27a cells were seeded in the bulk at 250,000 cells/mL. Prepared collagen gels were loaded into dry “H” pattern devices and allowed to gel at 37 °C for 30 minutes on day 0. After 30 minutes, vasculogenesis media consisting of EGM supplemented with vascular endothelial growth factor (VEGF, R&D Systems, 40 ng/mL) and phorbol 12-myristate 13-acetate

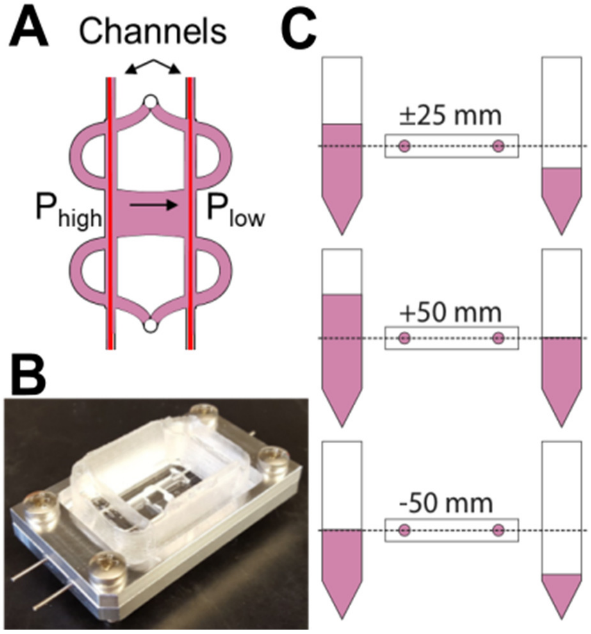

Figure 4.2.1 H pattern pressure gradient device and culture setup. (**A**) H pattern devices consist of two parallel channels embedded in a collagen matrix. A hydrostatic pressure is applied to each channel to create a pressure gradient across the center of the device. (**B**) An aluminum holder ensures device inlets are aligned and a media reservoir is attached to the device top. (**C**) A 50 mm H_2O pressure drop was applied in three ways, (top) +25 mm H_2O at the high-pressure (HP) channel and -25 mm H_2O at the low pressure (LP) channel, (middle) +50 mm H_2O HP and +0 mm H_2O LP, and (bottom)

(PMA, Sigma, 50 ng/mL) was added to the PDMS reservoir attached to the device. Acupuncture needles were manually removed, forming two channels per device (Figure 4.2.1A, B). A HUVEC suspension (5-10 million cells/mL) was perfused through each lumen and allowed to adhere overnight before media was perfused through the channels to clear unattached cells. Devices were cultured under static conditions for four days, with media changes daily. On day 4, each channel of the device was connected in a closed loop to a single 10 mL syringe. By varying the height of the media column in each syringe, a pressure was applied to the respective channel and a pressure gradient developed between the two channels in the device. The pressure gradient in each syringe was restored daily and maintained until day 7. On day 7 devices were fixed in 4% formaldehyde for 30 minutes.

In all experiments, one vessel is maintained at high pressure and the other at low pressure. For all experiments, the pressure drop between the two vessels is held constant at 50 mm H2O (~3.7 mm Hg), but the absolute pressure is varied (Figure 4.2.1C). In "+25/-25 mm H2O" devices, the high-pressure channel is maintained at +25 mm H2O and the negative pressure channel at -25 mm H2O. In "+50/0 mm H2O" devices the high-pressure channel is maintained at +50 mm H2O, and the outlet is open to the atmosphere. In “0/-50 mm H2O” devices the situation is reversed, where the high-pressure channel is maintained at atmospheric pressure and the negative pressure channel is set to -50 mm H2O. These conditions distinguish between the effect of interstitial flow and of applied pressure by varying their location in the respective devices.

Immunofluorescent staining and confocal imaging

Fixed devices were first blocked in a solution of phosphate buffered saline (PBS) containing Triton X-100 (0.5%, Sigma) and bovine serum albumin (BSA, 2%, Sigma). Devices were then incubated with Hoescht (1:250, ThermoFisher) and Phalloidin 568 (1:100, Life Technologies) for 1 hour to stain for nuclei and F-actin respectively. Devices were washed with PBS and imaged using a Nikon A1 confocal microscope.

Image analysis

Z-stack confocal images of devices were first processed using ImageJ to threshold and convert F-actin staining to binary image stacks. Images were then imported into MATLAB (Mathworks), where two custom scripts determined the cell density (automated nuclei counting) and calculated the vessel density, average volume per unique vessel, and the number of unique vessels per volume. To determine vessel volume, optical sections were first processed to identify F-actin positive regions. If F-actin staining formed a closed loop, the inside of the loop was filled and counted towards the total vessel volume. We determined the total number of unique vessels using a nearest neighbor approach to determine if a given F-actin positive voxel was continuous with, or distinct from other F-actin positive voxels. The total volume of each

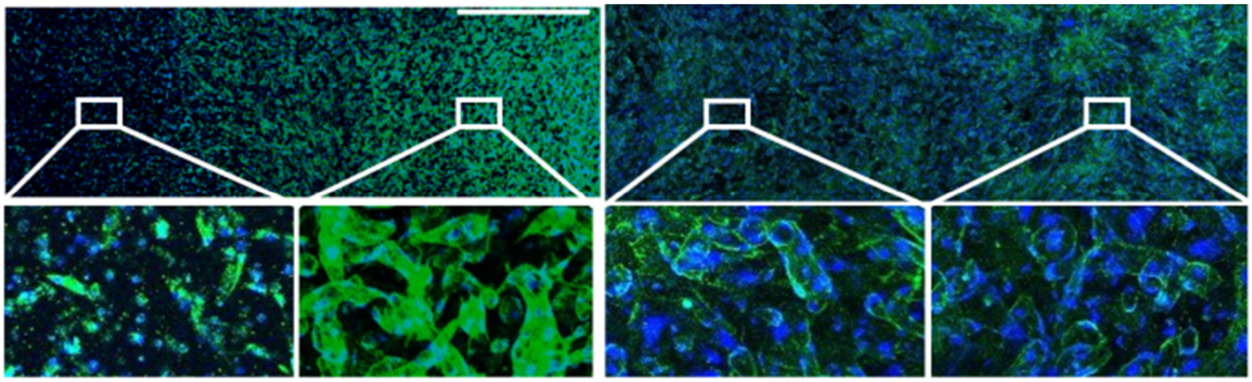

Figure 4.2.2 Vascular remodeling of a vascular network with applied pressure. Self-assembled human umbilical vein endothelial cell networks were cultured with an applied pressure drop (left, 50 mm H_2O, high pressure to low pressure from left to right) or under static conditions (right) for 3 days following 4 days of plexus self-assembly. Vessel density varied with pressure when a pressure drop was applied, but was uniform in the static case. Green = F-actin, Blue = Nuclei. Scale bar = 1000 μm for A and B.

unique vessel was then used as an estimate of connectivity, where a highly connected vasculature should have few unique vessels, each with a large volume.

4.2.3 Results

We sought to understand if changes in pressure applied to a self-assembled vascular network could also induce changes in the hierarchy and organization of the networks. We designed and fabricated a system to apply pressure gradients to self-assembled endothelial networks in dense collagen gels using two parent vessels as the pressure input (Figure 4.2.1). Between the two vessels a self-assembled plexus is formed by endothelial cells in the matrix over four days of static culture. using this system showed that an applied pressure drop of 50 mm H_2O across a 5 mm plexus over 3 days caused remodeling of the self-assembled plexus to be biased towards the low pressure region with higher cellular density, vascular connectivity, and vascular density. Devices with no applied pressure gradient, in contrast, do not show a bias in the distribution of these features (Figure 4.2.2).

We applied a constant 50 mm H_2O pressure difference across networks, but varied the absolute pressure imposed at the high and low channels. Regardless of the absolute pressure used cell density, vascular density, and average vessel volume followed a consistent trend. Cell density was increased on the low-pressure side of the device relative to the high-pressure side (Figure 4.2.3A). Vessel density was also increased when comparing low to high pressure areas (Figure 4.2.3B), with low pressure vessel density often more than double high-pressure density. In addition to the cell and vessel density increases, the average volume of independent vessels is increased in low pressure regions (Figure 4.2.3C, D) and was often considerably higher in the lowest absolute pressure condition. Together, these data suggest that low pressure regions are more densely vascularized and interconnected than their high pressure counterparts. The incorporation of a stromal population (HS27a) did not change this trend for any of these metrics.

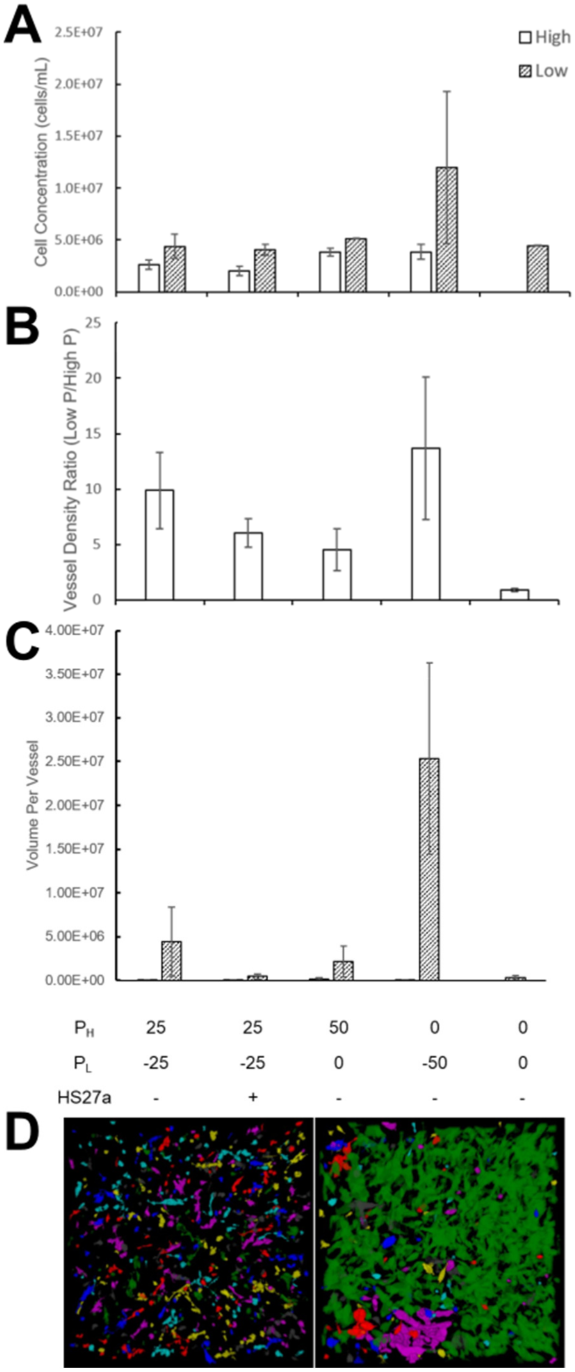

Figure 4.2.3 Vessel density and connectivity are increased in low pressure regions of devices. In all devices, cell concentration was increased in low pressure compared to high pressure (A) and the ratio of low pressure to high pressure vessel density was greater than 1 (B). This difference was significant for ±25 mm devices but statistical conclusions could not be made for other groups. Vessel connectivity was also significantly higher in low pressure regions (C). (D) Representative images of high pressure (left) and low pressure (right) connectivity for ±25 mm H_2O device. For both images, connected vessels share the same color.

4.2.4 Discussion

To determine if pressure could induce changes in vascular remodeling, we applied pressure gradients to self-assembled vascular networks.

Results from this system show that an applied pressure drop of 50 mm H_2O across a 5 mm plexus caused biased remodeling of a self-assembled plexus towards the low-pressure region. In this area, we observe higher cellular density, vascular connectivity, and vascular density. Previous reports have suggested that the lower pressure venous circulation may be more a more active site of angiogenesis.[55,56] Negative pressure wound closure devices are commonly used clinically and are known to improve neovascularization and vascular alignment in healing tissue.[57] The magnitude of the applied pressure is much larger for these devices (-50 - 125 mmHg), but a similar effect is observed. In agreement with this, our negative pressure condition (0/-50 mm H_2O applied pressure) enhanced the cell density, vessel density, and average volume per vessel in low pressure areas compared to both high and low-pressure zones in other pressure conditions.

To determine if a stromal population would alter the endothelial response to pressure cues, we incorporated the HS27a fibroblast line into cultures. The presence of HS27a may have reduced both the vessel density as well as the volume per vessel compared to the no HS27a condition, but these differences were not statistically significant. A reduction in volume could be explained by contraction of the vessel wall (i.e. decreased lumen diameter) or additional vascular pruning by recruited HS27a behaving like perivascular cells.[58] Pericytes and smooth muscle cells are known to help stabilize blood vessels,[59] and their incorporation may help stabilize vessels in high pressure zones and reduce pruning in these conditions.

To our knowledge this is the first demonstration of pressure driving vascular remodeling. Interstitial flow has been shown to promote endothelial proliferation,[60] but in each of these experiments interstitial flow is similar in both the high and low pressure regions (before remodeling) suggesting the applied pressure drives this effect. Hydrodynamic forces may remodel the vessel plexus through modulation of Notch signaling, Focal adhesion kinase (FAK) signaling, and matrix proteolytic activities. Notch signaling is known to be a regulator of embryonic vascular remodeling,[61,62] arterio-venous specification,[63] and perivascular cell recruitment[64] and loss of function of Notch1 as well as Notch ligands (Dll1, Dll4, Jag1) results in no embryonic vascular remodeling and embryonic lethality near E9.5.[61] Hydrodynamic flow is also known to stimulate the synthesis of matrix metalloproteases, which induces matrix degradation and vascular remodeling.[65] In addition, trans-endothelial pressure has been shown to induce phosphorylation of focal adhesion kinase (FAK), resulting in phenotypic changes, cytoskeletal remodeling, and further angiogenesis.[56] Evaluation of these signaling pathways, in addition to assessing for changes in vascular geometry and hierarchical structure during the vascular remodeling process would provide valuable insight. These could be accomplished in future studies by evaluating changes in mRNA expression and protein production by endothelial cell pathways for Notch and FAK, as well as for matrix degradation and remodeling by MMPs and ADAMs through qPCR, western blot, ELISA, and zymography. Further understanding of the drivers of this process will help determine the hydrodynamic factors needed to direct the development of an organized vascular network from a naïve plexus.

4.2.5 Conclusions

The role of hemodynamic cues in vascular remodeling and the development of hierarchical vascular networks is not well understood. We examined pressure conditions as a possible cue to control this process and found that local pressure conditions significantly altered the structure of self-assembled vascular networks. This effect was sensitive to the absolute pressure used, suggesting that the results we observed were due to pressure conditions and not due to interstitial flows through the collagen gels. Further research is needed to elucidate the mechanism controlling this pressure response, but control over this process may ultimately contribute to the generation of densely vascularized tissues through perturbation of local hydrostatic conditions.

4.3 References

1. Baeyens, N., Bandyopadhyay, C., Coon, B. G., Yun, S. & Schwartz, M. A. Endothelial fluid shear stress sensing in vascular health and disease. *J. Clin. Invest.* **126**, 821–828 (2016).
2. Jufri, N. F., Mohamedali, A., Avolio, A. & Baker, M. S. Mechanical stretch: physiological and pathological implications for human vascular endothelial cells. *Vasc. Cell* **7**, (2015).
3. Acevedo, A. D., Bowser, S. S., Gerritsen, M. E. & Bizios, R. Morphological and proliferative responses of endothelial cells to hydrostatic pressure: role of fibroblast growth factor. *J. Cell. Physiol.* **157**, 603–614 (1993).
4. Prystopiuk, V. *et al.* A two-phase response of endothelial cells to hydrostatic pressure. *J Cell Sci* **131**, jcs206920 (2018).
5. Schwartz, E. A., Bizios, R., Medow, M. S. & Gerritsen, M. E. Exposure of Human Vascular Endothelial Cells to Sustained Hydrostatic Pressure Stimulates Proliferation : Involvement of the V Integrins. *Circ. Res.* **84**, 315–322 (1999).
6. Müller-Marschhausen, K., Waschke, J. & Drenckhahn, D. Physiological hydrostatic pressure protects endothelial monolayer integrity. *Am. J. Physiol. Cell Physiol.* **294**, C324-332 (2008).
7. Mills, K. T., Stefanescu, A. & He, J. The global epidemiology of hypertension. *Nat. Rev. Nephrol.* **16**, 223–237 (2020).
8. Ranchoux, B. *et al.* Endothelial dysfunction in pulmonary arterial hypertension: an evolving landscape (2017 Grover Conference Series). *Pulm. Circ.* **8**, (2017).
9. Thenappan, T., Ormiston, M. L., Ryan, J. J. & Archer, S. L. Pulmonary arterial hypertension: pathogenesis and clinical management. *The BMJ* **360**, (2018).
10. Schindelin, J. *et al.* Fiji: an open-source platform for biological-image analysis. *Nat. Methods* **9**, 676–682 (2012).
11. Dobin, A. *et al.* STAR: ultrafast universal RNA-seq aligner. *Bioinformatics* **29**, 15–21 (2013).
12. Liao, Y., Smyth, G. K. & Shi, W. featureCounts: an efficient general purpose program for assigning sequence reads to genomic features. *Bioinforma. Oxf. Engl.* **30**, 923–930 (2014).
13. Wang, L., Wang, S. & Li, W. RSeQC: quality control of RNA-seq experiments. *Bioinforma. Oxf. Engl.* **28**, 2184–2185 (2012).
14. Robinson, M. D., McCarthy, D. J. & Smyth, G. K. edgeR: a Bioconductor package for differential expression analysis of digital gene expression data. *Bioinforma. Oxf. Engl.* **26**, 139–140 (2010).
15. Yu, G., Wang, L.-G., Han, Y. & He, Q.-Y. clusterProfiler: an R Package for Comparing Biological Themes Among Gene Clusters. *OMICS J. Integr. Biol.* **16**, 284–287 (2012).
16. Liberzon, A. *et al.* The Molecular Signatures Database Hallmark Gene Set Collection. *Cell Syst.* **1**, 417–425 (2015).
17. Hasan, S. S. *et al.* Endothelial Notch signalling limits angiogenesis via control of artery formation. *Nat. Cell Biol.* **19**, 928–940 (2017).
18. Zhou, W., Gross, K. M. & Kuperwasser, C. Molecular regulation of Snai2 in development and disease. *J. Cell Sci.* **132**, (2019).
19. Wyne, K. L., Pathak, K., Seabra, M. C. & Hobbs, H. H. Expression of the VLDL receptor in endothelial cells. *Arterioscler. Thromb. Vasc. Biol.* **16**, 407–415 (1996).
20. Rao, X. *et al.* Loss of Methyl-CpG–Binding Domain Protein 2 Enhances Endothelial Angiogenesis and Protects Mice Against Hind-Limb Ischemic Injury. *Circulation* **123**, 2964–2974 (2011).
21. Chistiakov, D. A., Orekhov, A. N. & Bobryshev, Y. V. Effects of shear stress on endothelial cells: go with the flow. *Acta Physiol. Oxf. Engl.* **219**, 382–408 (2017).
22. Mack, J. J. & Iruela-Arispe, M. L. NOTCH regulation of the endothelial cell phenotype. *Curr. Opin. Hematol.* **25**, 212–218 (2018).

23. Mack, J. J. *et al.* NOTCH1 is a mechanosensor in adult arteries. *Nat. Commun.* **8**, (2017).
24. Givens, C. & Tzima, E. Endothelial Mechanosignaling: Does One Sensor Fit All? *Antioxid. Redox Signal.* **25**, 373–388 (2016).
25. Jeggle Pia *et al.* Epithelial Sodium Channel Stiffens the Vascular Endothelium In Vitro and in Liddle Mice. *Hypertension* **61**, 1053–1059 (2013).
26. Ezaki, T. *et al.* Time Course of Endothelial Cell Proliferation and Microvascular Remodeling in Chronic Inflammation. *Am. J. Pathol.* **158**, 2043–2055 (2001).
27. Noseda, M. *et al.* Notch Activation Induces Endothelial Cell Cycle Arrest and Participates in Contact Inhibition: Role of p21Cip1 Repression. *Mol. Cell. Biol.* **24**, 8813–8822 (2004).
28. Jonigk, D. *et al.* Plexiform Lesions in Pulmonary Arterial Hypertension. *Am. J. Pathol.* **179**, 167–179 (2011).
29. Ajami, N. E. *et al.* Systems biology analysis of longitudinal functional response of endothelial cells to shear stress. *Proc. Natl. Acad. Sci. U. S. A.* **114**, 10990–10995 (2017).
30. Ruffenach, G. *et al.* Histological hallmarks and role of Slug/PIP axis in pulmonary hypertension secondary to pulmonary fibrosis. *EMBO Mol. Med.* **11**, e10061 (2019).
31. Hopper, R. K. *et al.* In Pulmonary Arterial Hypertension, Reduced BMPR2 Promotes Endothelial-to-Mesenchymal Transition via HMGA1 and its Target Slug. *Circulation* **133**, 1783–1794 (2016).
32. Hwang Juliana *et al.* Pulsatile Versus Oscillatory Shear Stress Regulates NADPH Oxidase Subunit Expression. *Circ. Res.* **93**, 1225–1232 (2003).
33. Beckers, C. M. L., van Hinsbergh, V. W. M. & van Nieuw Amerongen, G. P. Driving Rho GTPase activity in endothelial cells regulates barrier integrity. *Thromb. Haemost.* **103**, 40–55 (2010).
34. Barlow, H. R. & Cleaver, O. Building Blood Vessels—One Rho GTPase at a Time. *Cells* **8**, (2019).
35. Suttorp, N. *et al.* Bacterial exotoxins and endothelial permeability for water and albumin in vitro. *Am. J. Physiol.-Cell Physiol.* **255**, C368–C376 (1988).
36. Rosa, P. M., Gopalakrishnan, N., Ibrahim, H., Haug, M. & Halaas, Ø. The intercell dynamics of T cells and dendritic cells in a lymph node-on-a-chip flow device. *Lab. Chip* **16**, 3728–3740 (2016).
37. Fessel, J. P., Loyd, J. E. & Austin, E. D. The genetics of pulmonary arterial hypertension in the post-BMPR2 era. *Pulm. Circ.* **1**, 305–319 (2011).
38. D'Amico, R. W. *et al.* Pulmonary Vascular Platform Models the Effects of Flow and Pressure on Endothelial Dysfunction in BMPR2 Associated Pulmonary Arterial Hypertension. *Int. J. Mol. Sci.* **19**, (2018).
39. Szulcek, R. *et al.* Delayed Microvascular Shear Adaptation in Pulmonary Arterial Hypertension. Role of Platelet Endothelial Cell Adhesion Molecule-1 Cleavage. *Am. J. Respir. Crit. Care Med.* **193**, 1410–1420 (2016).
40. Moretti, M., Prina-Mello, A., Reid, A. J., Barron, V. & Prendergast, P. J. Endothelial cell alignment on cyclically-stretched silicone surfaces. *J. Mater. Sci. Mater. Med.* **15**, 1159–1164 (2004).
41. Lovett, M., Lee, K., Edwards, A. & Kaplan, D. L. Vascularization strategies for tissue engineering. *Tissue Eng. Part B Rev.* **15**, 353–70 (2009).
42. Lucitti, J. L. *et al.* Vascular remodeling of the mouse yolk sac requires hemodynamic force. *Dev. Camb. Engl.* **134**, 3317–26 (2007).
43. Lucitti, J. L. *et al.* Vascular remodeling of the mouse yolk sac requires hemodynamic force. *Dev. Camb. Engl.* **134**, 3317–26 (2007).
44. Udan, R. S., Vadakkan, T. J. & Dickinson, M. E. Dynamic responses of endothelial cells to changes in blood flow during vascular remodeling of the mouse yolk sac. *Dev. Camb. Engl.* **140**, 4041–50 (2013).

45. Stratman, A. N., Davis, M. J. & Davis, G. E. VEGF and FGF prime vascular tube morphogenesis and sprouting directed by hematopoietic stem cell cytokines. *Blood* **117**, 3709–3719 (2011).
46. Baeyens, N. *et al.* Vascular remodeling is governed by a VEGFR3-dependent fluid shear stress set point. *eLife* **4**, e04645 (2015).
47. Fischer, A., Schumacher, N., Maier, M., Sendtner, M. & Gessler, M. The Notch target genes Hey1 and Hey2 are required for embryonic vascular development. *Genes Dev.* **18**, 901–911 (2004).
48. Baldwin, H. S. Early embryonic vascular development. *Cardiovasc. Res.* **31 Spec No**, E34–E45 (1996).
49. Eichmann, A. *et al.* Vascular development: From precursor cells to branched arterial and venous networks. *Int. J. Dev. Biol.* **49**, 259–267 (2005).
50. Ng, C. P. & Swartz, M. A. Fibroblast alignment under interstitial fluid flow using a novel 3-D tissue culture model. *Am. J. Physiol. Heart Circ. Physiol.* **284**, H1771-7 (2003).
51. Polacheck, W. J., Charest, J. L. & Kamm, R. D. Interstitial flow influences direction of tumor cell migration through competing mechanisms. *Proc. Natl. Acad. Sci. U. S. A.* **108**, 11115–20 (2011).
52. Helm, C.-L. E., Fleury, M. E., Zisch, A. H., Boschetti, F. & Swartz, M. A. Synergy between interstitial flow and VEGF directs capillary morphogenesis in vitro through a gradient amplification mechanism. *Proc. Natl. Acad. Sci.* **102**, 15779–15784 (2005).
53. Vickerman, V. & Kamm, R. D. Mechanism of a flow-gated angiogenesis switch: early signaling events at cell-matrix and cell-cell junctions. *Integr. Biol. Quant. Biosci. Nano Macro* **4**, 863–74 (2012).
54. Fisher, A. B., Chien, S., Barakat, A. I. & Nerem, R. M. Endothelial cellular response to altered shear stress. *Am. J. Physiol.-Lung Cell. Mol. Physiol.* **281**, L529–L533 (2001).
55. Ausprunk, D. H. & Folkman, J. Migration and proliferation of endothelial cells in preformed and newly formed blood vessels during tumor angiogenesis. *Microvasc. Res.* **14**, 53–65 (1977).
56. Vickerman, V. & Kamm, R. D. Mechanism of a flow-gated angiogenesis switch: early signaling events at cell-matrix and cell-cell junctions. *Integr. Biol. Quant. Biosci. Nano Macro* **4**, 863–74 (2012).
57. Erba, P. *et al.* Angiogenesis in wounds treated by microdeformational wound therapy. *Ann. Surg.* **253**, 402–9 (2011).
58. Bergers, G. & Song, S. The role of pericytes in blood-vessel formation and maintenance. *Neuro-Oncol.* **7**, 452–64 (2005).
59. Avolio, E., Alvino, V. V., Ghorbel, M. T. & Campagnolo, P. Perivascular cells and tissue engineering: Current applications and untapped potential. *Pharmacol. Ther.* **171**, 83–92 (2017).
60. Hernández Vera, R. *et al.* Interstitial fluid flow intensity modulates endothelial sprouting in restricted Src-activated cell clusters during capillary morphogenesis. *Tissue Eng. Part A* **15**, 175–85 (2009).
61. Hofmann, J. J. & Iruela-Arispe, M. L. Notch signaling in blood vessels: Who is talking to whom about what? *Circ. Res.* **100**, 1556–1568 (2007).
62. Fischer, A., Schumacher, N., Maier, M., Sendtner, M. & Gessler, M. The Notch target genes Hey1 and Hey2 are required for embryonic vascular development. *Genes Dev.* **18**, 901–911 (2004).
63. Swift, M. R. & Weinstein, B. M. Arterial-venous specification during development. *Circ. Res.* **104**, 576–88 (2009).
64. Kofler, N. M., Cuervo, H., Uh, M. K., Murtomäki, A. & Kitajewski, J. Combined deficiency of Notch1 and Notch3 causes pericyte dysfunction, models CADASIL, and results in arteriovenous malformations. *Sci. Rep.* **5**, 16449 (2015).

65. Ota, R. *et al.* Roles of matrix metalloproteinases in flow-induced outward vascular remodeling. *J. Cereb. Blood Flow Metab. Off. J. Int. Soc. Cereb. Blood Flow Metab.* **29**, 1547–58 (2009).
66. Arakawa, C. K., Badeau, B. A., Zheng, Y. & DeForest, C. A. Multicellular Vascularized Engineered Tissues through User-Programmable Biomaterial Photodegradation. *Adv. Mater.* **29**, n/a-n/a (2017).

5. Hemodynamic Conditioning of Engineered Cardiovascular Tissues

5.1 Abstract

The development of the heart is an intricate process that involves the transformation of a linear heart tube into a complex four chambered organ. The formation of a perfusable vascular network and the initiation of flow are some of the earliest milestone events in this process, but comparatively little is known about the impact of these early hemodynamic forces on cardiomyocyte morphogenesis. In this work we developed a novel scale model of the linear heart tube to enable studies on the effect of developmentally relevant hemodynamic forces on cardiac tissues. Using a collagen gel casting approach, we combined endothelial cells, stromal cells, and stem-cell derived cardiomyocytes into engineered tube structures. We demonstrate that these tissues can support the application of biomimetic shear and pressure conditions using a customized perfusion device that enables real-time monitoring of intraluminal pressure. We show that these engineered cardiac tubes spontaneously beat and generate measurable pressure waveforms. When challenged with increasing preload through increased hemodynamic load we also observed a Frank-Starling like increase in the pressure produced by the tissue. This novel platform represents a promising tool to interrogate the effect of hemodynamic conditions on developing cardiac tissues.

5.2 Introduction

From the earliest stages of development, endothelial cells and cardiomyocytes are intimately linked. As the heart begins to form, endothelial-like endocardial cells and myocardial cells are thought to branch off from a common precursor.[1] The heart tube takes shape and the onset of beating and flow mark a milestone event in embryonic development. Under these new conditions the nascent vascular system undergoes dramatic reorganization[2] and the heart begins a complex process of looping that transforms it into a 4-chambered organ.[3] The forces of flow are known to be important throughout this transformation, and aberrant flow is thought to be an early contributor to congenital heart disease.[4,5] In tissue engineering, the production of mature myocardial tissue from immature PSC-derived cardiomyocytes is a goal that remains elusive. Many attempts have been made to improve the functionality of engineered heart tissues by mimicking the mechanical forces present in early development, but adult-like myocardium has not been produced *in vitro*.[6,7] Of the forces present in development, the mechanical stress and strain experienced by the myocardium has been an area of particular interest in engineering heart tissue. In contrast, the cooperative role of endothelial cells that are also subject to the forces of myocardial contraction as well as hemodynamic loads has received less attention.

Communication between endothelial cells and cardiomyocytes through several pathways is necessary for normal development.[8] Endothelial specific Neurofibromatosis type 1 (NF1) knockout causes fatal cardiac defects early in mouse development.[9] Neuregulin-1 (Nrg-1) produced by the endocardium can stimulate cardiomyocyte growth and is necessary for myocardial trabeculation.[10,11] In vitro, the more active Nrg-1β isoform has been shown to improve the maturation of mouse iPSC-derived cardiomyocytes.[12] Moreover, a recent report shows that endothelial production of the Nrg-1β isoform is dependent on flow conditions.[13] Similarly, PDGF-β production is flow sensitive in endothelial cells and loss-of-function mutants show developmental abnormalities in the myocardium. In adult tissues, the conversation between the myocardium and endocardium continues. Nitric oxide (NO) and Endothelin-1 (ET-1) both influence the dynamics of myocardial contraction[14,15] and the production of both are flow-sensitive in endothelial cells.[16,17] In vitro systems which incorporate endothelial cells exposed to fluid flow or utilize hemodynamic forces to induce mechanical stress on the tissue are relatively recent and not well characterized. These models use primary cells from non-human sources,[18,19] do not include endothelial cells,[19,20] and do not have distinct endothelial and myocardial compartments like the developing heart tube.

Given the importance of endothelial cell-cardiomyocyte crosstalk during development and in adult life, we sought to develop a model to enable the exploration of the effect of flow-sensitive cues from the endothelium on the maturation of PSC-derived cardiomyocytes (hPSC-CM). It is unknown if engineered heart tissues exposed to biomimetic pressure and flow will develop a more mature phenotype than tissues which experience only mechanical stimulation. We designed and fabricated engineered heart tube models which have distinct endothelial and myocardial compartments and could support hemodynamic conditions reflective of early heart tube development. This platform consists of a simplified model of the human heart tube at approximately 2:1 scale in which different flow and pressure regimes can be explored to understand their respective contributions to tissue development. In this system a 640 µm diameter tube (wall thickness ~200 µm) is formed from PSC-CM and stromal cells in a collagen hydrogel, and the inner lumen is seeded with endothelial cells. Hemodynamic conditions within the tube can be controlled by altering the volumetric flow rate through the channel as well as the fluidic resistance of the outflow. In this way, the effects of shear stress and pressure can be independently evaluated. By dramatically increasing the outflow resistance the effect of shear stress can be minimized as flow will instead lead to stretching of the tube radially while some flow is also driven transluminally. By using a pressure controller to drive flow, cycles of stretching and relaxation can be pre-programmed. In the same system the opposite hemodynamic case can also be investigated by minimizing the outflow resistance. In this case the shear stress can be modulated over a wide range while the pressure inside the channel is kept to a minimum. Configurations between these two extremes can also be investigated to determine if cooperative effects between pressure and shear signaling also exist. This model will allow investigation of whether the combinatorial effect of cyclic strain and shear stress will improve the structural and functional characteristic of engineered heart tissues over cyclic strain alone.

5.3 Materials and Methods

Design of collagen tube molding system

To create cellularized collagen tubes a molding system was designed using Fusion 360. This consisted of two identical perfusion blocks where collagen tubes would be mounted and tubing connected for perfusion, and two molding blocks (top and bottom) into which liquid collagen was injected and polymerized (Figure 5.1A). Each of these components were machined in polysulfone using a Taig CNC mill so that devices could withstand repeated autoclave cycles without deformation. Perfusion blocks featured 1-inch lengths of 23-gauge hypodermic tubing (640 μm outer diameter) mounted into push fit holes drilled into the block body. Molding blocks were designed as two mating pieces where a hemispherical groove was machined in each so that when both pieces were pressed together a cylindrical void space was formed. By fitting the molding blocks over the exposed hypodermic tubing of the perfusion blocks a tubular void space was formed in which liquid collagen could be added. The diameter of the hypodermic tubing set the inner diameter of the collagen tube while the diameter of the cylinder formed by the two molding blocks dictated the outer diameter. Molding blocks were machined in a variety of sizes to produce collagen tubes with a wall thickness of 100, 200, 250, or 400 μm. Prior to use in cell culture, all components were autoclaved.

Cell culture

C2C12 mouse myoblasts (ATCC) used for collagen tube structural testing and validation were cultured in DMEM supplemented with 10% FBS. For cardiomyocyte containing constructs transgenic RUES2 human embryonic stem cells expressing the fluorescent calcium reporter GCaMP3 were differentiated into cardiomyocytes by modulation of activin A, BMP4, and Wnt signaling using a previously reported protocol.[21] Differentiated cardiomyocytes were cultured in RPMI 1640 supplemented with B27 (Thermo Fisher). HS27a stromal cells were cultured in RPMI 1640 supplemented with 10% FBS, 1% penicillin and streptomycin, 2 mM L-glutamine, and 1 mM sodium pyruvate. Human umbilical vein endothelial cells (HUVEC) were cultured in endothelial growth media (EGM, Lonza).

Fabrication of engineered tubes (ET)

Polysulfone molds and perfusion blocks were autoclaved and then assembled in a biosafety cabinet. 250 µm acupuncture needles were inserted into the 23-gauge hypodermic tubing to ensure the inner lumen of the collagen tube remained patent after collagen gelation. Collagen gels were prepared by mixing an acidic collagen stock solution (15 mg/mL) with 1N NaOH, 10X Medium M199 (Thermo Fisher), and EGM to reach neutralization and a target concentration of 10 mg/mL. After homogenizing this mixture, the collagen was degassed by placing under vacuum for 30-60 minutes while on ice. This 10 mg/mL solution was then mixed with resuspended cells to reach a final collagen concentration of 1.25 mg/mL, 3 mg/mL, or 6 mg/mL. For compaction and burst pressure testing, gels were made with 30 million C2C12 cells/mL. For all other studies, gels were prepared with hPSC-CM (20 million cells/mL), HS27a stromal cells (10 million cells/mL), and HUVEC (2 million cells/mL).[22] The liquid collagen and cell solution was then pipetted into polysulfone molds (~50 µL per tube) and thermally crosslinked by incubating at 37 ºC for 45 minutes.

After crosslinking the molds were flooded with culture media (3:1 RMPI+B27:EGM for cardiac constructs) and carefully separated to leave a thin walled engineered tube (ET) bound to the hypodermic tubing of the perfusion blocks. ETs were cultured overnight to stabilize the structure of the gel. The following day the hypodermic tubing was carefully retracted until ETs bridged the two perfusion blocks with 5 - 10 mm of the center of the ET unsupported. The acupuncture needle was then removed, revealing an open and perfusable lumen.

Collagen tube perfusion

Perfusion was started two to four days following ET formation. First, the ends of the ETs were gently fixed in place on the hypodermic tubing using #6-0 silk suture to prevent leaking. Silicone tubing (.025” ID) was then run from 10 mL syringes mounted on a syringe pump (KD Scientific) to one of the two free ends of hypodermic tubing per ET. To increase pressure in some ETs a 10 mm length of 30-gauge hypodermic tubing was attached to the outlet, raising the outflow resistance. ETs were cultured for up to 12 days under continuous perfusion.

Burst pressure testing

To measure the burst pressure of ETs, we modified the perfusion setup to include a pressure sensor (Honeywell ABPDJJT001PGAA5) in series with the ET. The pressure sensor was connected to a microcontroller (Arduino Uno) and computer for data logging. The acquisition frequency for the pressure sensor was ~60 Hz. Burst pressure was evaluated by completely occluding the ET outflow and running the attached syringe pump at a constant rate until a steady state was reached or until bursting occurred.

ET pressure measurements

To measure the pressure generated by ETs during culture the same setup was used as in burst pressure testing, but the outlet was left open and perfusable. Pressure waveforms were recorded at multiple flow rates and were taken with ETs inside of an incubator at 37 ºC using fresh media.

Immunostaining and imaging

Movies of live ET contractions were acquired in brightfield and in green channels (using GCaMP3 signal) using a Nikon Ti2 microscope with an ORCA-Flash4.0 sensor or a Nikon Ti microscope with a Canon EOS 80D DSLR camera.

For immunostaining, ETs were unmounted from the perfusion apparatus and transferred to a 24 well plate containing 4% paraformaldehyde. ETs were fixed for 30 minutes prior to washing with PBS (3 x 5 min). For staining, ETs were first blocked and permeabilized with solutions of 2% BSA and 0.5% Triton X-100 in PBS for 30 minutes. ETs were incubated with primary antibodies for 1 hour at room temperature or overnight at 4 °C and washed with PBS. Secondary antibodies, as well as actin and nuclear stains were added for 1 hour at room temperature before washing with PBS. Stained ETs were imaged with Yokogawa W1 spinning disk system mounted to a Nikon Ti inverted microscope. Primary antibodies included: CD31 (1:30, Abcam ab28364) and cTnT (1:100, Invitrogen MA5-12960). Secondary antibodies, and other stains included: Alexa Fluor goat anti-rabbit 647 (1:100, Thermo Fisher A-21235), Alexa

Fluor goat anti-mouse 568 (1:100, Thermo Fisher A-11004), Alexa Fluor Phalloidin 568 (1:100, Thermo Fisher, A12380), and Hoescht 33342.

Image analysis

The wall thickness of C2C12 ETs was measured using still images of ET-hypodermic tubing interface where there was clear contrast between the two structures. For beating frequency analysis of cardiomyocyte ETs the GCaMP3 signal was plotted over time in a region of interest in the center of the ET using Fiji.[23] Frequency and contraction amplitude was determined by peak identification in R and frequency data was also estimated through computing the Discrete Fourier Transform of the intensity waveform. The extent of contraction was evaluated by measuring the 2D area of the center of the ET over time. This was accomplished by thresholding out the brighter center region of the ET and measuring the size of this region over the time series.

5.4 Results

We designed a small-scale injection molding platform to fabricate cellularized collagen tubes with controlled wall thickness. Each injection molding device was fabricated from polysulfone and consisted of four components (Figure 5.1A) that could be easily assembled in a biosafety cabinet following autoclaving. For all ETs the inner diameter was fixed at 640 μm, but wall thicknesses of 100, 200, 250, and 400 μm were also used. The fabrication of ETs with a wall thickness less than 200 μm was inconsistent and difficult to reproduce because of the manufacturing tolerances required. For example, to achieve a 100 μm thick ET wall the hypodermic tubing must be mounted within 0.5° of normal to the surface of the perfusion block and aligned with another two components with little to no additional error. ETs with a wall

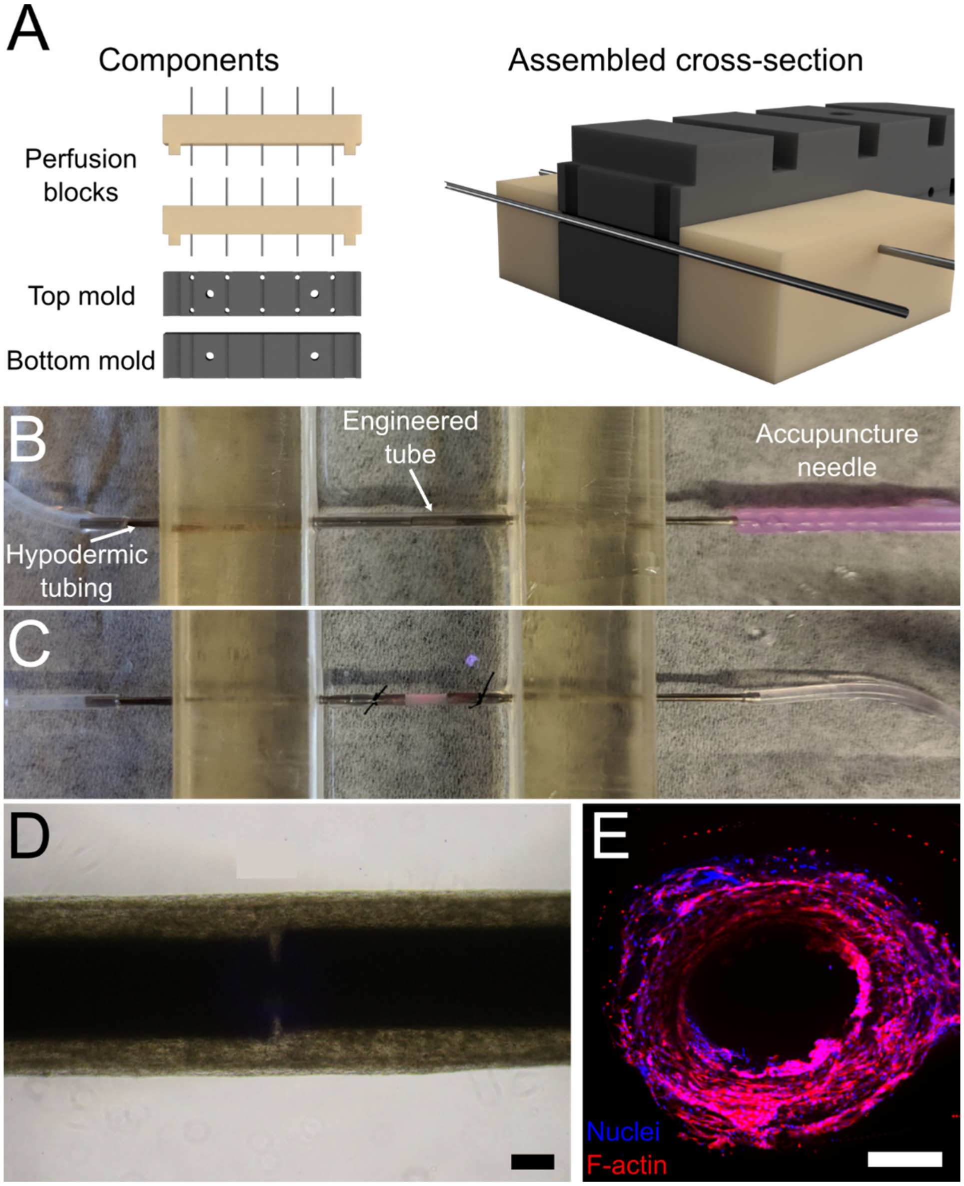

Figure 5.1 Engineered Tube Fabrication and Culture. (A) ET fabrication components showing inlet, outlet, and bottom mold. (B) After removing top and bottom mold, a thin layer of collagen coats hypodermic tubing. (C) After removing the acupuncture needle, retracting the hypodermic tubing and fixing the ET in place, fluorescent beads can be perfused through the lumen. (D) Representative image of ET 24 hours after crosslinking. (E) Representative image of C2C12 ET after 5 days of culture showing dense and compacted cells surrounding an open lumen. Scale = 500 µm.

thickness greater than 200 µm were produced by adding cell and collagen gel solutions into molds (~50 µL per tube, 5 tubes per mold) and thermally crosslinking. Removal of the molding components yielded a thin walled ET mounted on hypodermic tubing (Figure 5.1B). After retracting the hypodermic tubing and ligating in place, the ET could be perfused (Figure 5.1C). Shortly after casting cells in gel into an ET, the cells compacted around the metal tubing (Figure 5.1D) and maintained this geometry after the center of the ET was advanced off the metal tubing and left unsupported for several days (Figure 5.1E).

To validate the fabrication strategy, we utilized a mouse myoblast cell line (C2C12). Cell-gel mixtures of C2C12 (30 million cells/mL) in 6 mg/mL collagen were seeded into the molding platform and crosslinked. Once removed, ETs were submerged in medium and cultured without perfusion for up to 6 days. Over this time, cells rapidly compacted the collagen matrix and reduced the wall thickness of the tissue from ~225 μm to less than 100 μm (Figure 5.2A). Cellular alignment is an important parameter in the function of engineered muscle constructs.[24] To understand the extent to which cells can align through tissue compaction alone, we fixed engineered C2C12 tissues after 12 days of culture and stained for F-actin (Figure 5.2B). In these constructs we observed both aligned and disorganized cellular morphologies. The wall thickness of tissues was maintained around 100 μm but could be as small as 50 μm in certain regions (Figure 5.2B, bottom). To understand the hemodynamic limits of the ETs we also performed burst pressure testing in ETs of different wall thickness (Figure 5.2C). Day 4 C2C12 ETs were sutured in place on hypodermic tubing and the outflow was plugged while a syringe pump was used to drive a constant flow into the tube (Figure 5.2C). For both thick walled (500 μm, Figure 5.2D) and thin walled (250 μm, Figure 5.2E) constructs the burst pressure was more than the 50 mmHg maximum of the pressure sensor. The flow rate necessary to cause tissue failure was also dependent on the tissue wall thickness. Because the collagen gels are porous and the cells do not form a water-impermeable barrier in the ET, transmural flow developed across the ET wall. This transmural flow allowed ETs to reach a steady state pressure despite blocking axial flow through the ET lumen (e.g. Figure 5.2E, first two peaks). The evaluation of burst pressure therefore required repeated measurements at the same volumetric flow rate to

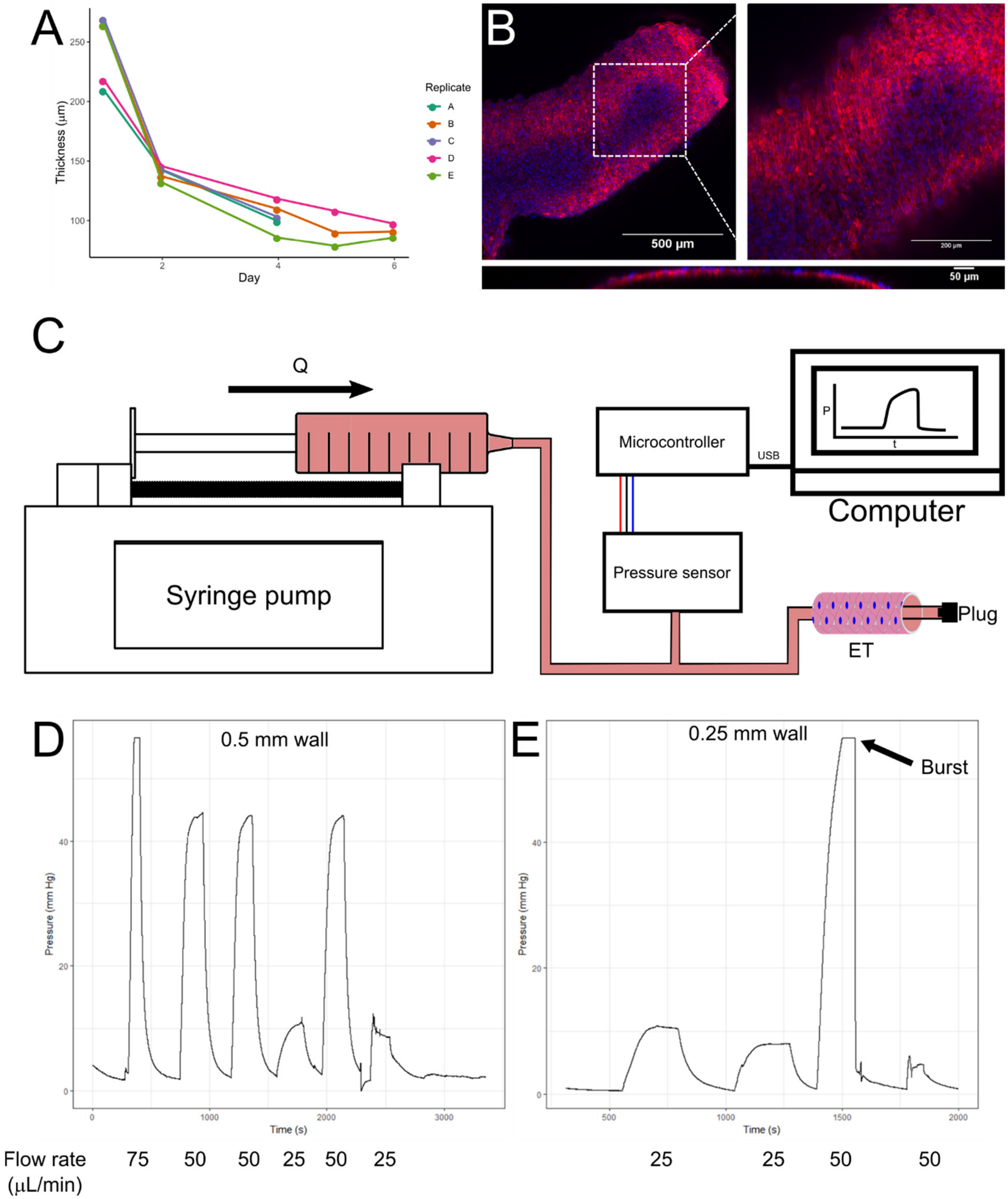

Figure 5.2 Engineered tubes rapidly compact and support physiologic pressures. (A) The wall thickness of C2C12 ETs rapidly declines over time in culture, approaching early physiologic dimensions. (B) . After 12 days of culture C2C12 ETs compact and align circumferentially (red = F-actin, blue = nuclei). (C) Schematic of perfusion and pressure measurement setup used for burst pressure measurements. (D) Representative pressure trace of 500 µm wall thickness ET under multiple flow rates. (E) Representative pressure trace of 250 µm wall thickness ET, showing failure at > 50 mmHg.

determine if an elevated steady state was reached or if failure had occurred (Figure 5.2E, final two peaks).

We next sought to incorporate human embryonic stem cell derived cardiomyocytes, stromal cells, and endothelial cells into cardiac ETs (cETs) (Figure 5.3A). We initially explored both 1.25 mg/mL and 6 mg/mL collagen concentrations as the base for cET mixtures to compare basal tissue structure and geometry. In culture the distribution GCaMP3 signal from hPSC-CM in cETs appeared uniform in 1.25 mg/mL gels while 6 mg/mL gels were more irregular and clustered in appearance (Figure 5.3B). Staining of fixed tissues confirmed these observations, with cTnT positive hPSC-CM appearing as rounded and independent cells without clear sarcomere structure in 6 mg/mL gels and cellular organization (Figure 5.3C). 1.25 mg/mL cETs in contrast had elongated cTnT positive hPSC-CM with more organized sarcomeres and cell bodies were generally aligned circumferentially (Figure 5.3D). While the cellular structure of lower concentration gels was more physiologic, these constructs were challenging to reproduce reliably. The lower gel concentration and structurally weaker collagen tube led to excessive failures early in fabrication and culture. Small imperfections in the cast tube were more prevalent and more likely to cause failure when freeing cETs from molds, retracting hypodermic tubing, and ligating in place for perfusion. Even without manipulation the lower gel concentration and minor imperfections in the mold contributed to the development of holes in cETs, likely as a result of the cells contracting and remodeling the collagen matrix (Figure 5.3D). The fabrication of 6 mg/mL cETs was more robust as the stiffer gel was easier to manipulate and more resilient to imperfections in the molding process. From these results a 3 mg/mL gel concentration was chosen for the remaining cETs, which enabled more reliable fabrication of perfusable tissues while also providing cells with an environment that could be more easily remodeled.

We next sought to characterize cETs under continuous perfusion under two different loading schemes. eCTs fabricated with hPSC-CM, HS27a stromal cells, and HUVEC in 3

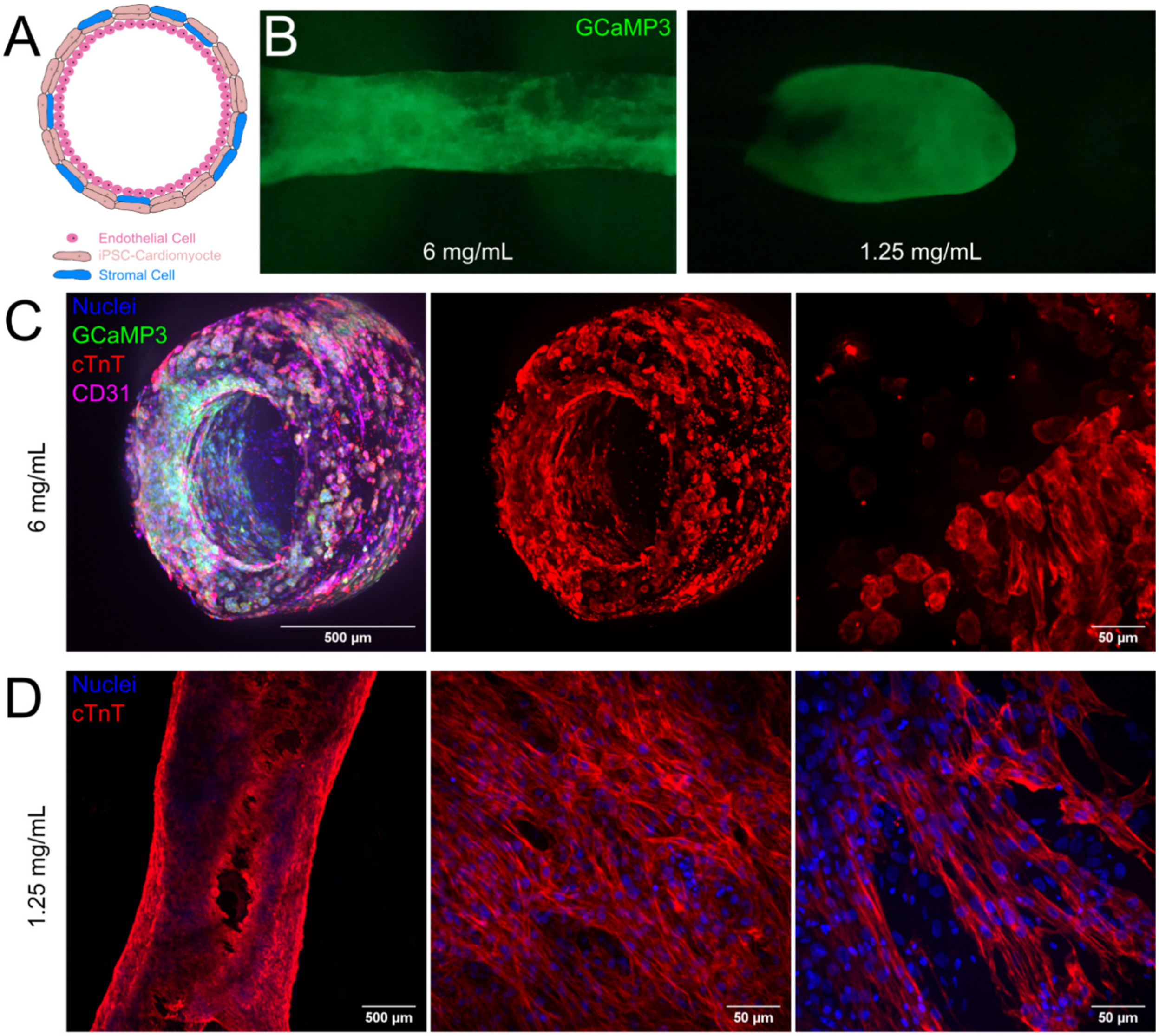

Figure 5.3 Gel concentration alters cardiac engineered tube structure. (A) Schematic of cell populations in hESC-CM containing ETs. (B) Representative images of the GCaMP3 signal in 6 mg/mL and 1.25 mg/mL collagen concentration ETs. (C) Representative staining of 6 mg/mL collagen ET showing good maintenance of tissue geometry, but an uneven distribution of cells. (D) Representative staining of 1.25 mg/mL collagen ET showing a more uniform distribution of cells and more organized sarcomere morphology.

mg/mL collagen gels were formed and cultured under static conditions for 48 hours before establishing perfusion at 2 µL/min. The outflow resistance was elevated for half of cETs by adding a 1 cm length of 30-gauge hypodermic tubing in series with the outlet connection. Tubes were cultured for one week under continuous perfusion with daily video recording of spontaneous beating using the GCaMP3 signal. The spontaneous rhythm was highly variable in cultured cETs, with some tissues displaying high frequency regular contractions (Figure 5.4A), whereas others exhibited irregular patterns (Figure 5.4B). Over time no differences were observed in contraction frequency based on the outflow resistance, although a slight but statistically insignificant ($p = 0.11$) trend towards higher contraction frequency in higher outflow resistance cETs was present (Figure 5.4C). In cETs we also sought to measure the force produced by tissue contraction by placing a pressure sensor in the flow path. In patent cETs without defects we were able to measure the pressure produced by contraction under different loading conditions. By raising or lowing the flow rate going through the tissue we could effectively change the preload on the cET (Figure 5.4D). When challenged with a larger preload, the amplitude of cET contraction significantly increased, following a length-tension type relationship (Figure 5.4E). To estimate the physical change in the cET chamber size we analyzed brightfield videos of the contracting cET and tracked the visible area of the lumen, observing that contractions decreased the cross-sectional area by approximately 5 – 7% per beat (Figure 5.4G).

5.5 Discussion

From the earliest stages of development and through adult life the myocardium and the endothelium are in close contact and communication.[25] Their link goes beyond the transport of nutrients as hemodynamic and mechanical cues influence signaling between cell types.[26] In the pursuit of understanding cardiac development and the production of mature stem-cell derived cardiomyocytes, however, recapitulation and study of this signaling axis outside of living animals to our knowledge has not been achieved. While engineered systems have included cardiomyocyte and endothelial populations, these typically lack hemodynamic control and are not suitable for determining the effect of shear stress and pressure conditions on engineered cardiac tissues. We have developed an engineered tube system to address this gap and

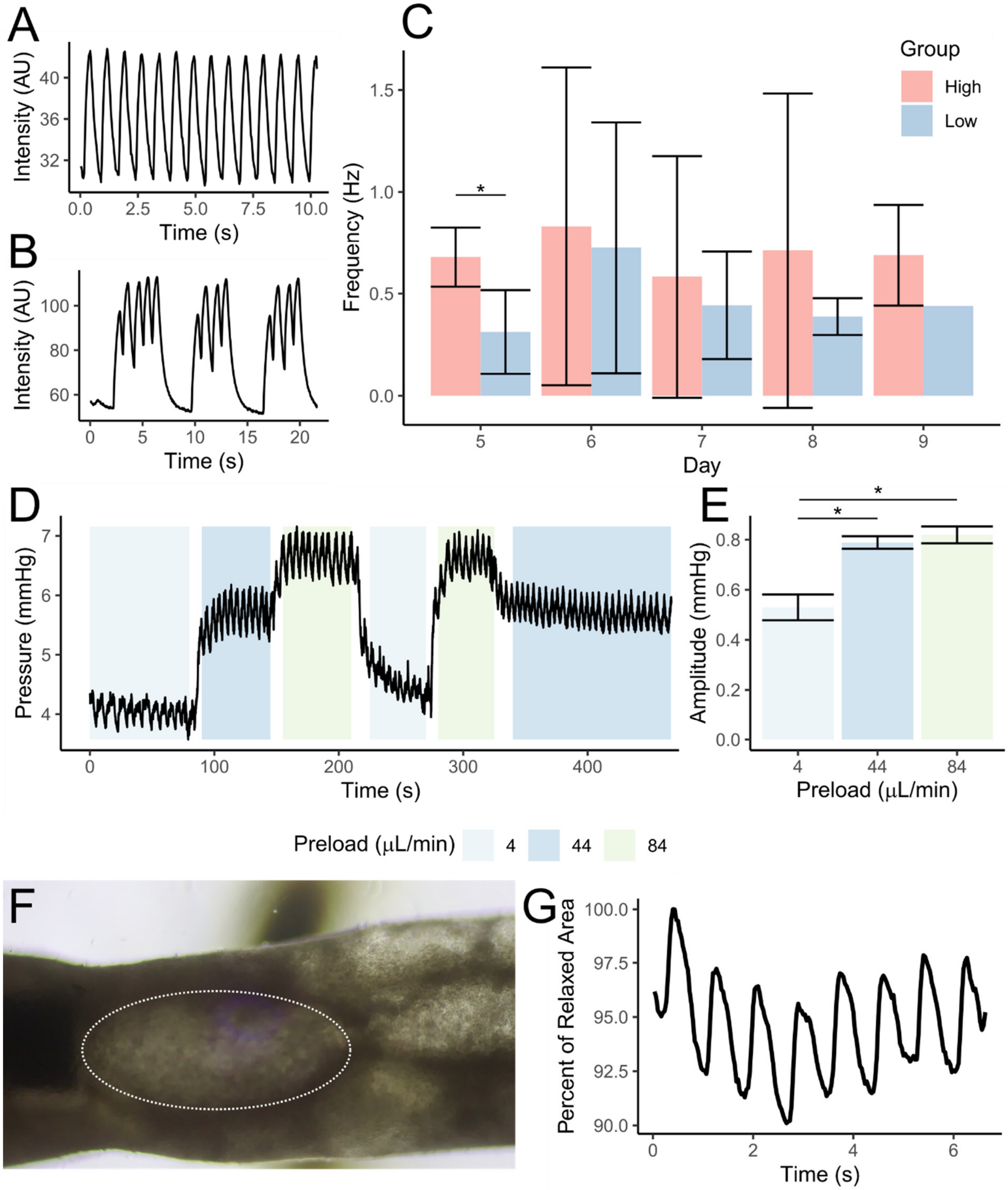

Fig 5.4 Cardiac engineered tubes exhibit length-tension behavior. Representative traces of spontaneous ET beating show regular (A) and irregular frequencies (B). Spontaneous beating frequency was highly variable in ETs under two pressure conditions (C). Representative trace of ET hydrostatic pressure under multiple hemodynamic loads (D) where the amplitude of contraction increased under larger load (E). Representative ET (F) with measurement of lumen area (white) over time (G). Error bars represent 95% confidence intervals. *$p < 0.05$

provide a model in which the role of hemodynamic parameters in cardiomyocyte biology can be systematically investigated.

Using both a mouse myoblast cell line as well as human pluripotent stem-cell derived cardiomyocytes we demonstrated the formation of engineered tubes at approximately twice the diameter of the linear human heart tube. ETs rapidly compacted after casting, achieving wall thicknesses less than 100 µm when using a 250 µm mold. These tissues could be cultured for more than one week under continuous perfusion and were capable of aligning and elongating circumferentially. After continuous culture without electrical pacing, spontaneous contractions in cardiac constructs produced measurable pressure waveforms. Altering the preload imposed on the ET increased the amplitude of the pressure waveform showing a Frank-Starling like response.[27] Together these observations indicate cardiac ETs replicated key aspects of cardiac physiology in generating hemodynamic work and responding to variations chamber pressure conditions.

While the magnitude of the pressure produced in this study is small (~25% of the linear heart tube in the mouse[28]), it is a promising first step towards mimicking early cardiac physiology in vitro. Force generation can likely be improved by implementing additional conditioning regimes known to promote the maturation of cardiomyocytes including long term electrical and mechanical pacing.[7] The implementation of electrical pacing would require minor modification of the platform to incorporate suitable field stimulation electrodes.[29] Mechanical pacing could be integrated through programming alternative waveforms into the pressure source driving flow through the ET, and synchronization with electrical stimulation. Microscale geometric patterns have also been shown to promote cardiomyocyte alignment[30] and radial patterns could be incorporated into casting molds that would transfer to ETs.

Although we did not observe differences between hemodynamic conditions here, the mechanics are in place to test a wider range of shear and pressure conditions. The high-pressure condition in this study was ~0.5 mmHg (approximately the diastolic pressure in the mouse linear heart tube) more than the low-pressure condition under ideal conditions in which there is no transmural flow. Testing across a wider dynamic range is straightforward to implement through changes in outflow resistance or flow rate. The shear stress condition imposed here was also very low (< 0.1 dyne/cm^2) in order to limit media consumption for the relatively large inner diameter of the ETs. This limitation can be addressed by using a peristaltic pump and a pulse dampener[31] to create a recirculation loop with steady flow, or by reducing the diameter of ET. The latter option is possible, but challenging due to the manufacturing tolerances required for the molding components. Pathways of particular interest in exploring the state of endothelial-myocardial crosstalk under different hemodynamic loads include several with known readily available inhibitors, including Nrg1,[32] PDGF-β,[33] ET-1,[34] and eNOS.[35]

Careful attention must also be given to the cell sources used, as the HS27a and HUVEC populations used in this study are unlikely to be representative of the cardiac populations present in early development and may not capture the same signaling events. For example, endothelial heterogeneity among different organs and in different stages of development may result in different interactions with PSC-CM.[36] The developmental origin of endocardial cells and endothelial cells of the coronary arteries and capillaries are distinct from other endothelial cells, including the coronary veins, further suggesting a specialized role.[1,37] Replacement of the stromal population with cardiac fibroblasts is also possible with recently developed differentiation protocols.[38]

5.6 Conclusions

In this study we developed a model to determine the effect of hemodynamic forces on endothelial-cardiomyocyte signaling and cardiomyocyte maturation. Engineered tubes designed as a scale model of the linear heart tube and fabricated from stem cell derived cardiomyocytes were contractile, produced measurable pressure waveforms, and exhibited hallmark Frank-

Starling behavior when preload was increased. This first of its kind system may prove useful for enhancing the function of engineered myocardial tissue and investigating developmental questions regarding signaling between endothelial cells and the myocardium and heart tube looping.

5.7 References

1. Misfeldt, A. M. *et al.* Endocardial cells are a distinct endothelial lineage derived from Flk1+ multipotent cardiovascular progenitors. *Dev. Biol.* **333**, 78–89 (2009).
2. Lucitti, J. L. *et al.* Vascular remodeling of the mouse yolk sac requires hemodynamic force. *Dev. Camb. Engl.* **134**, 3317–26 (2007).
3. Taber, L. A. Biophysical mechanisms of cardiac looping. *Int. J. Dev. Biol.* **50**, 323–332 (2006).
4. Banjo, T. *et al.* Haemodynamically dependent valvulogenesis of zebrafish heart is mediated by flow-dependent expression of *miR-21*. *Nat. Commun.* **4**, 1978 (2013).
5. Sedmera, D. *et al.* Cellular changes in experimental left heart hypoplasia. *Anat. Rec.* **267**, 137–145 (2002).
6. Scuderi, G. J. & Butcher, J. Naturally Engineered Maturation of Cardiomyocytes. *Front. Cell Dev. Biol.* **5**, (2017).
7. Ronaldson-Bouchard, K. *et al.* Advanced maturation of human cardiac tissue grown from pluripotent stem cells. *Nature* **556**, 239–243 (2018).
8. Hsieh, P. C. H., Davis, M. E., Lisowski, L. K. & Lee, R. T. Endothelial-cardiomyocyte interactions in cardiac development and repair. *Annu. Rev. Physiol.* **68**, 51–66 (2006).
9. Gitler, A. D. *et al. Nf1* has an essential role in endothelial cells. *Nat. Genet.* **33**, 75–79 (2003).
10. Marchionni, M. A. Cell-cell signalling. neu tack on neuregulin. *Nature* **378**, 334–335 (1995).
11. Zhao, Y. Y. *et al.* Neuregulins promote survival and growth of cardiac myocytes. Persistence of ErbB2 and ErbB4 expression in neonatal and adult ventricular myocytes. *J. Biol. Chem.* **273**, 10261–10269 (1998).
12. Iglesias-García, O. *et al.* Neuregulin-1β Induces Mature Ventricular Cardiac Differentiation from Induced Pluripotent Stem Cells Contributing to Cardiac Tissue Repair. *Stem Cells Dev.* **24**, 484–496 (2015).
13. Zheng, C., Zhang, X., Li, C., Pang, Y. & Huang, Y. Microfluidic Device for Studying Controllable Hydrodynamic Flow Induced Cellular Responses. *Anal. Chem.* **89**, 3710–3715 (2017).
14. Seddon, M., Shah, A. M. & Casadei, B. Cardiomyocytes as effectors of nitric oxide signalling. *Cardiovasc. Res.* **75**, 315–326 (2007).
15. Pönicke, K. *et al.* Endothelin Receptors in the Failing and Nonfailing Human Heart. *Circulation* **97**, 744–751 (1998).
16. Dimmeler, S. *et al.* Activation of nitric oxide synthase in endothelial cells by Akt-dependent phosphorylation. *Nature* **399**, 601–605 (1999).
17. Yamazaki, T. *et al.* Endothelin-1 Is Involved in Mechanical Stress-induced Cardiomyocyte Hypertrophy. *J. Biol. Chem.* **271**, 3221–3228 (1996).
18. Lux, M. *et al.* In vitro maturation of large-scale cardiac patches based on a perfusable starter matrix by cyclic mechanical stimulation. *Acta Biomater.* **30**, 177–187 (2016).
19. Nguyen, M.-D. *et al.* Effects of physiologic mechanical stimulation on embryonic chick cardiomyocytes using a microfluidic cardiac cell culture model. *Anal. Chem.* **87**, 2107–2113 (2015).
20. Rogers, A. J., Fast, V. G. & Sethu, P. Biomimetic Cardiac Tissue Model Enables the Adaption of Human Induced Pluripotent Stem Cell Cardiomyocytes to Physiological Hemodynamic Loads. *Anal. Chem.* **88**, 9862–9868 (2016).
21. Shiba, Y. *et al.* Human ES-cell-derived cardiomyocytes electrically couple and suppress arrhythmias in injured hearts. *Nature* **489**, 322–5 (2012).
22. Roberts, M. A. *et al.* Stromal Cells in Dense Collagen Promote Cardiomyocyte and Microvascular Patterning in Engineered Human Heart Tissue. *Tissue Eng. Part A* **22**, 633–644 (2016).

23. Schindelin, J. *et al.* Fiji: an open-source platform for biological-image analysis. *Nat. Methods* **9**, 676–682 (2012).
24. Feinberg, A. W. *et al.* Controlling the contractile strength of engineered cardiac muscle by hierarchal tissue architecture. *Biomaterials* **33**, 5732–5741 (2012).
25. Brutsaert, D. L. Cardiac Endothelial-Myocardial Signaling: Its Role in Cardiac Growth, Contractile Performance, and Rhythmicity. *Physiol. Rev.* **83**, 59–115 (2003).
26. Andrés-Delgado, L. & Mercader, N. Interplay between cardiac function and heart development. *Biochim. Biophys. Acta* **1863**, 1707–16 (2016).
27. Asnes, C. F., Marquez, J. P., Elson, E. L. & Wakatsuki, T. Reconstitution of the Frank-Starling Mechanism in Engineered Heart Tissues. *Biophys. J.* **91**, 1800–1810 (2006).
28. Lindsey, S. E., Butcher, J. T. & Yalcin, H. C. Mechanical regulation of cardiac development. *Front. Physiol.* **5**, 318 (2014).
29. Tandon, N. *et al.* Optimization of Electrical Stimulation Parameters for Cardiac Tissue Engineering. *J. Tissue Eng. Regen. Med.* **5**, e115–e125 (2011).
30. Williams, N. P. *et al.* Engineering anisotropic 3D tubular tissues with flexible thermoresponsive nanofabricated substrates. *Biomaterials* **240**, 119856 (2020).
31. Alloush, M. M., Liermann, M., Zedan, A. & Oweis, G. F. A Novel Pulse Damper for Endothelial Cell Flow Bioreactors. *Cardiovasc. Eng. Technol.* **10**, 95–111 (2019).
32. Hegde, G. V. *et al.* Blocking NRG1 and Other Ligand-Mediated Her4 Signaling Enhances the Magnitude and Duration of the Chemotherapeutic Response of Non–Small Cell Lung Cancer. *Sci. Transl. Med.* **5**, 171ra18-171ra18 (2013).
33. Kuai, J. *et al.* Characterization of Binding Mode of Action of a Blocking Anti-Platelet-Derived Growth Factor (PDGF)-B Monoclonal Antibody, MOR8457, Reveals Conformational Flexibility and Avidity Needed for PDGF-BB To Bind PDGF Receptor-β. *Biochemistry* **54**, 1918–1929 (2015).
34. Okada, M. & Nishikibe, M. BQ-788, a selective endothelin ET(B) receptor antagonist. *Cardiovasc. Drug Rev.* **20**, 53–66 (2002).
35. Cotter, G. *et al.* L-NMMA (a nitric oxide synthase inhibitor) is effective in the treatment of cardiogenic shock. *Circulation* **101**, 1358–1361 (2000).
36. Aird, W. C. Endothelial Cell Heterogeneity. *Cold Spring Harb. Perspect. Med.* **2**, (2012).
37. Wu, B. *et al.* Endocardial Cells Form the Coronary Arteries by Angiogenesis through Myocardial-Endocardial VEGF Signaling. *Cell* **151**, 1083–1096 (2012).
38. Zhang, J. *et al.* Functional cardiac fibroblasts derived from human pluripotent stem cells via second heart field progenitors. *Nat. Commun.* **10**, 1–15 (2019).

6. Conclusions and future directions

The in vitro models developed in this dissertation represent advances in recapitulating the diversity of geometric and hemodynamic cues present throughout the vasculature. First, we developed two novel platforms for investigating the effect of curvature on endothelial biology in both small and large vessels, showing distinct changes in endothelial responses to flow. The spiral microvessel system provides a platform from which systematic changes in vessel curvature and torsion can be investigated. Our results highlight that these geometric parameters shape endothelial transcription even in the absence of disturbed flows. This result is significant in suggesting that the considerable heterogeneity of vascular geometries present in the vasculature is correlated with a much wider continuum of endothelial responses to blood flow than is currently appreciated. Further research with spiral vessels may help to expand this understanding, but ultimately these results must be validated in the complex vascular geometries found in living animals. Controlled study of these features in vivo is made challenging by the difficulty of controlling for structure and flow in the small vessels of model organisms, but we have recently developed a multiphoton based fabrication technique that enables the production of arbitrarily shaped vascular structures as small as capillaries (Figure 6.1, Appendix C). We have shown that it is possible to use imaging data from the microvasculature to create vascular replicas at the same scale in collagen hydrogels. This new approach is an exciting advance that addresses the problems of complexity and reproducibility in studying the effect of microvascular structure on endothelial flow responses.

In large vessels we developed a technique for replicating the geometry of cerebral aneurysms and determining the effect of aneurysm specific flow on endothelial cells. Using idealized vessel models we performed proof-of-principle experiments that validated the effect of curvature and altered hemodynamic conditions on endothelial structure and the distribution

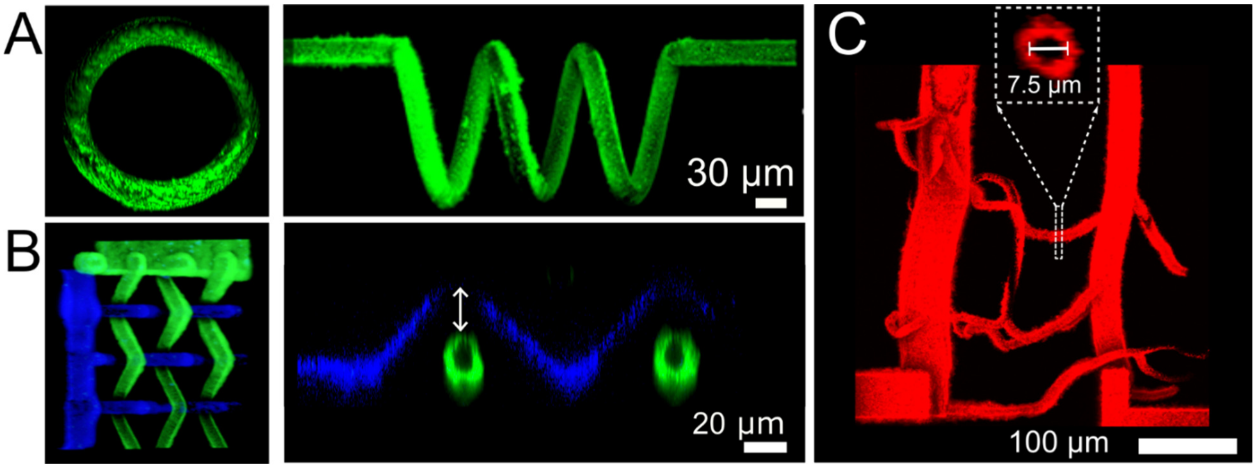

Figure 6.1 Representative Two Photon ablated vascular structures. (**A**) Ablated spiral vessel perfused with fluorescent beads. (**B**) Ablated basketweave structure (vessel diameter = 15 µm) perfused with blue and green beads in independent channels. (**C**) Imaging data from the mouse cerebral cortex was used to ablate and perfuse capillary scale vessels with fluorescent beads.

of key proteins. Further, we were the first to demonstrate that replicas of patient-specific aneurysm geometries can be used to determine endothelial gene expression information localized to specific aneurysm regions. Advances in this kind of model that incorporate smooth muscle cells and enable physiologic stretch will help to more completely bridge the longstanding gap between aneurysm computational fluid dynamic research and vascular biology. New models like this will inform approaches to the clinical management of cerebral aneurysms and will serve as testbeds for novel therapeutic approaches.

Our observations from these systems suggested that the relatively understudied hemodynamic force of pressure might have a larger than appreciated role in vascular biology. Based on this we developed microfluidic and tissue platforms to test the effect of pressure on endothelial flow sensing and vascular remodeling. We found that pressure conditions could dramatically alter the morphology and density of endothelial cells even when exposed to shear stress. RNA sequencing results from these studies revealed that transcriptional differences developed between cells under the same shear stress and different pressure conditions, but the consequence of these differences was not fully determined. In 3D tissues pressure differences led to very different levels of vascular remodeling, with high-pressure inducing regression and low-pressure promoting density and interconnectivity. These results suggest pressure may play a role in the development of vascular hierarchy. Additional work is needed to link these transcriptional and remodeling responses, but we have provided significant evidence that pressure cues influence endothelial cells in 2D and 3D paradigms. Based on these findings microfluidic devices made from materials that cells cannot remodel may severely limit an understanding of the effect of pressure conditions. Future models that can support perfusion with highly controlled shear and pressure parameters in cell-remodelable biomaterials will enable a deeper understanding of the role of pressure in vascular biology.

Finally, we aimed to develop a model to resolve how pressure and shear conditions influenced endothelial interactions with cardiomyocytes. While endothelial cells and cardiomyocytes are closely apposed from the earliest stage of development, the role of these hemodynamic cues on the development of cardiac tissues is not well understood. We took inspiration from the linear heart tube of cardiac development and developed a scale model containing endothelial, stromal, and stem-cell derived cardiomyocytes. Using a custom designed perfusion apparatus that enables real-time monitoring of intraluminal pressure we demonstrated that these engineered tubes could withstand the shear and pressure conditions of early heart development. We showed that engineered cardiac tubes spontaneously beat and generated measurable pressure waveforms. When challenged with increasing preload through increased hemodynamic load we also observed a Frank-Starling like increase in the pressure produced by the tissue. The replication of these characteristic features of the early heart suggests this platform will be useful for interrogating the effect of hemodynamic conditions on developing cardiac tissues. The outcome of those experiments could lead to a greater understanding of the factors that guide cardiac tissue maturation and the development of heart tissues for use in disease modeling, drug developments, or novel therapeutics.

This dissertation demonstrates and expands upon the influence of geometric and hemodynamic factors on the endothelium through the development of several in vitro model systems. Together these provide new insights into endothelial biology and provide new tools for enabling a more complete understanding of vascular biology.

Appendix A. Supplemental Figures to Chapter 3

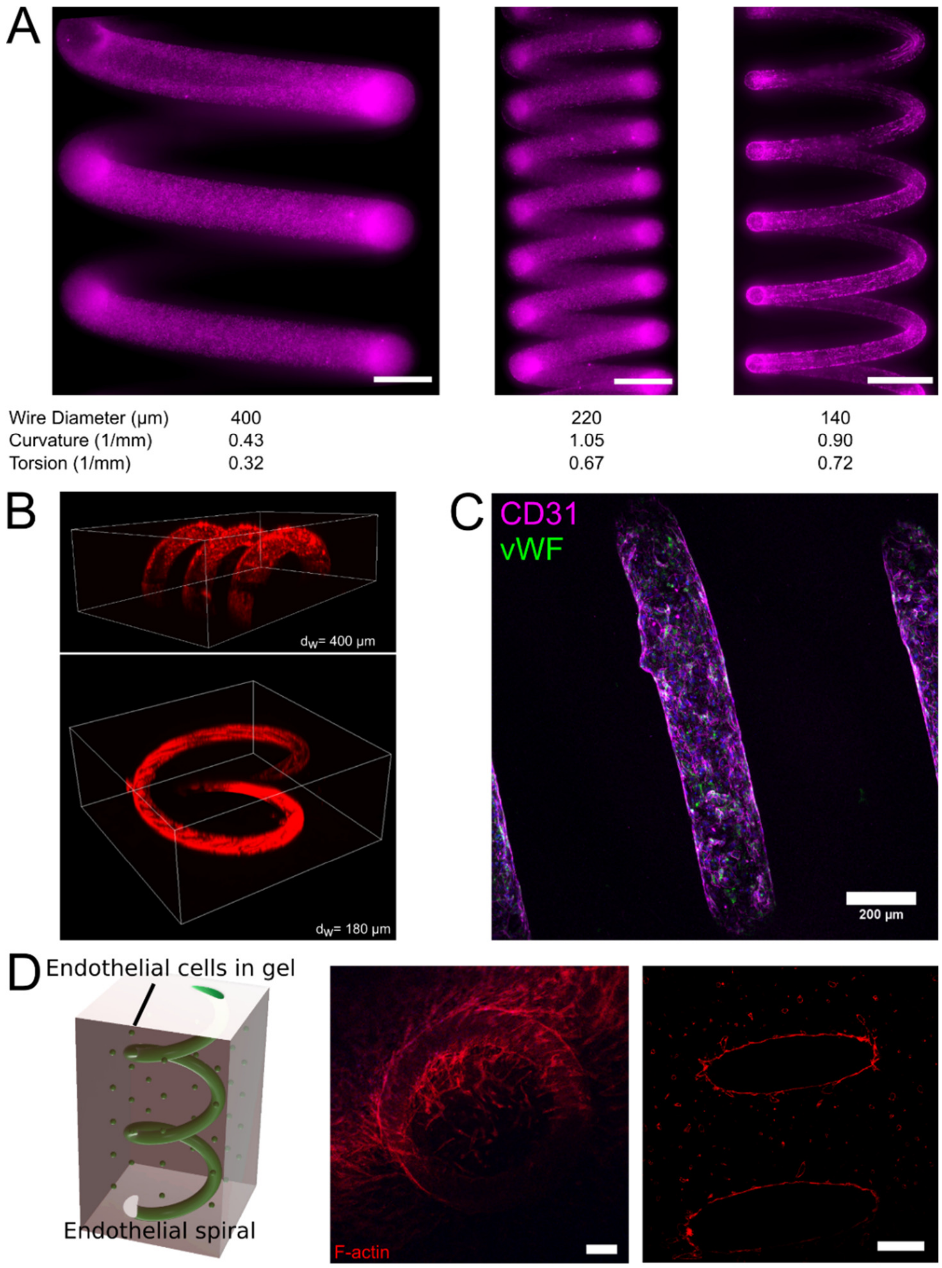

Figure A1 Spiral vessel dimensions, cell seeding, and vasculogenesis model. (A) Representative spiral vessels formed in 7.5 mg/mL collagen hydrogel and corresponding vessel diameter, curvature, and torsion values (scale = 500 µm). (B) 3D reconstructions of confocal z-stack images of 400 µm (upper) and 180 µm (lower) spiral vessels in collagen hydrogel perfused with fluorescent beads (1 µm diameter). (C) Maximum intensity projection (MIP) of representative endothelialized 180 µm spiral vessel. Magenta, CD31; green, von

Willebrand Factor; blue, nuclei. (D) Anastomoses of spiral vessel from the lumen with self-assembled endothelial cell network in the bulk collagen matrix. Left panel: schematic; center panel: MIP of a single spiral loop in XY plane (scale = 200 μm); and optical section of the side view of spiral vessel connected with self-assembled vascular network (scale = 400 μm).

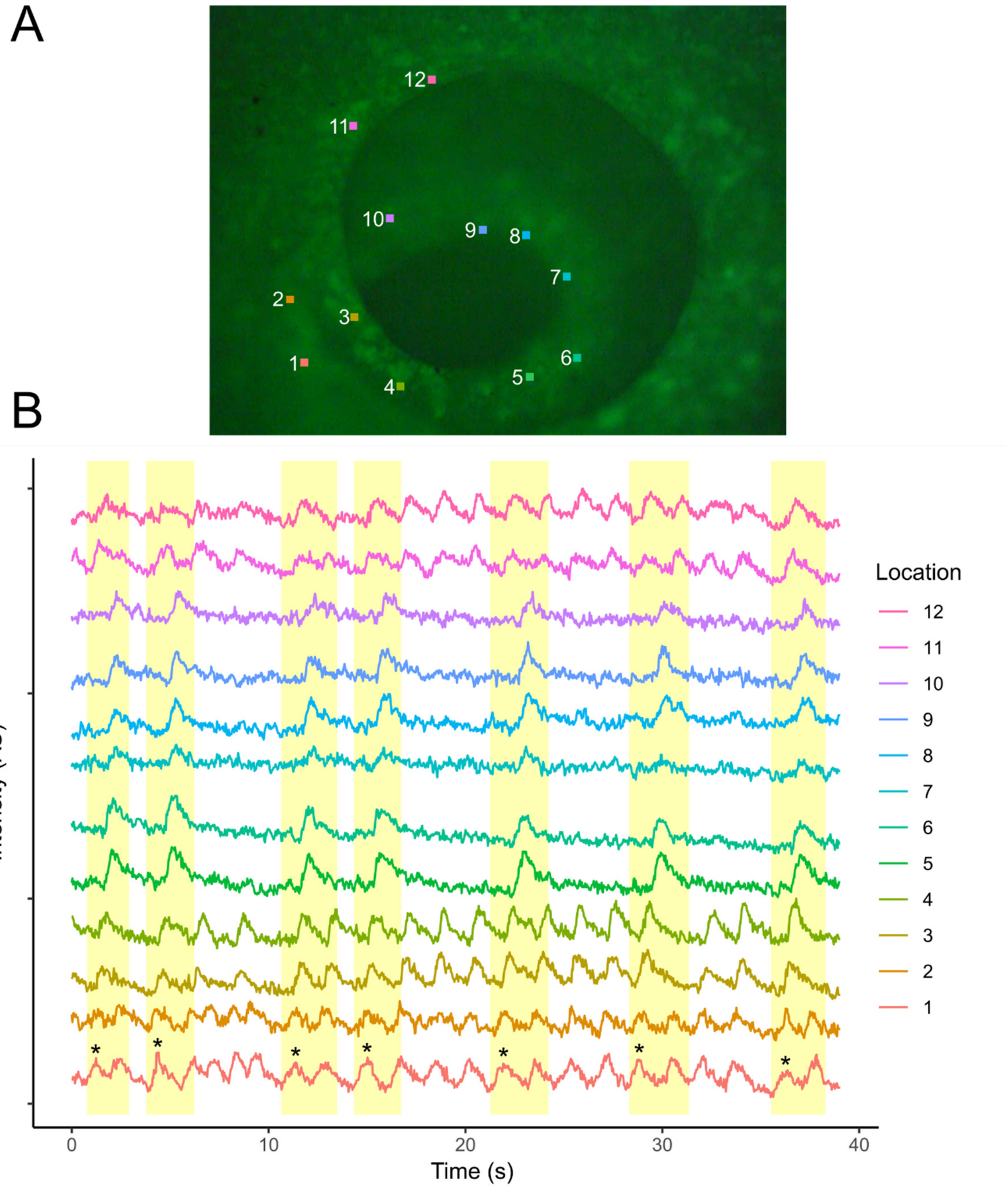

Figure A2. Vascularized heart chamber calcium wave propagation. (A) Snapshot frame from Movie S2 with 12 regions of interest along the spiral vessel. Regions 1, 2, 11, and 12 are on the same plane at the top surface, regions 3 – 10 extend into the tissue. (B) GCaMP3 intensity for each region of interest plotted over the time. Highlighted regions indicate calcium waves that travel from the top surface to the bottom of the chamber with the initiating wave marked by a (*).

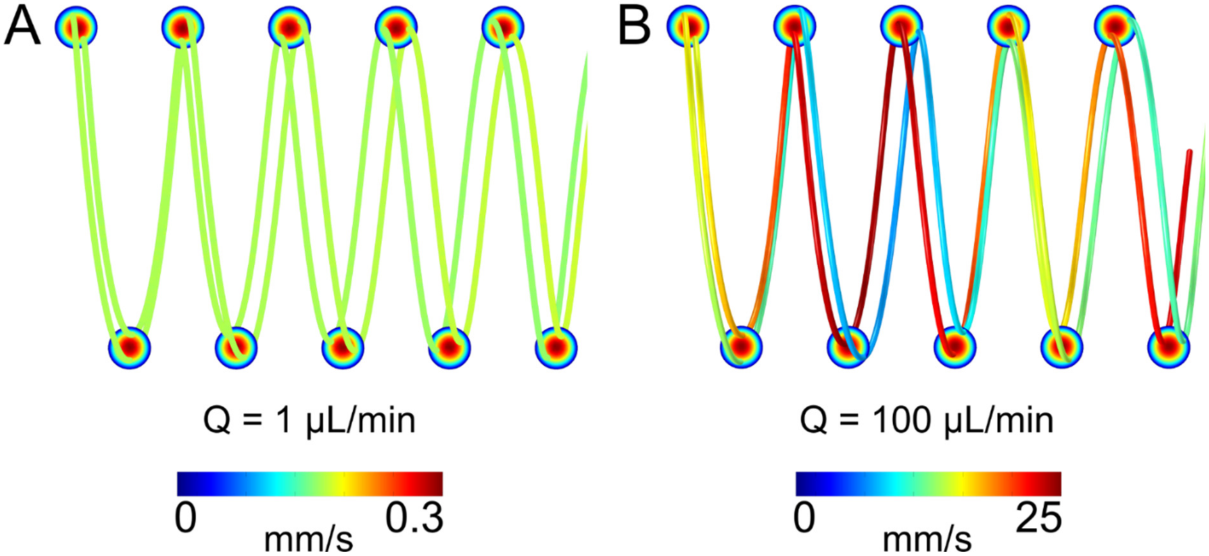

Figure A3. Vascularized heart chamber calcium wave propagation. Computational fluid dynamics plots of spiral vessel streamlines (color expressed with primary velocity magnitude) at Q = 1 μL/min (A) and Q = 100 μL/min (B).

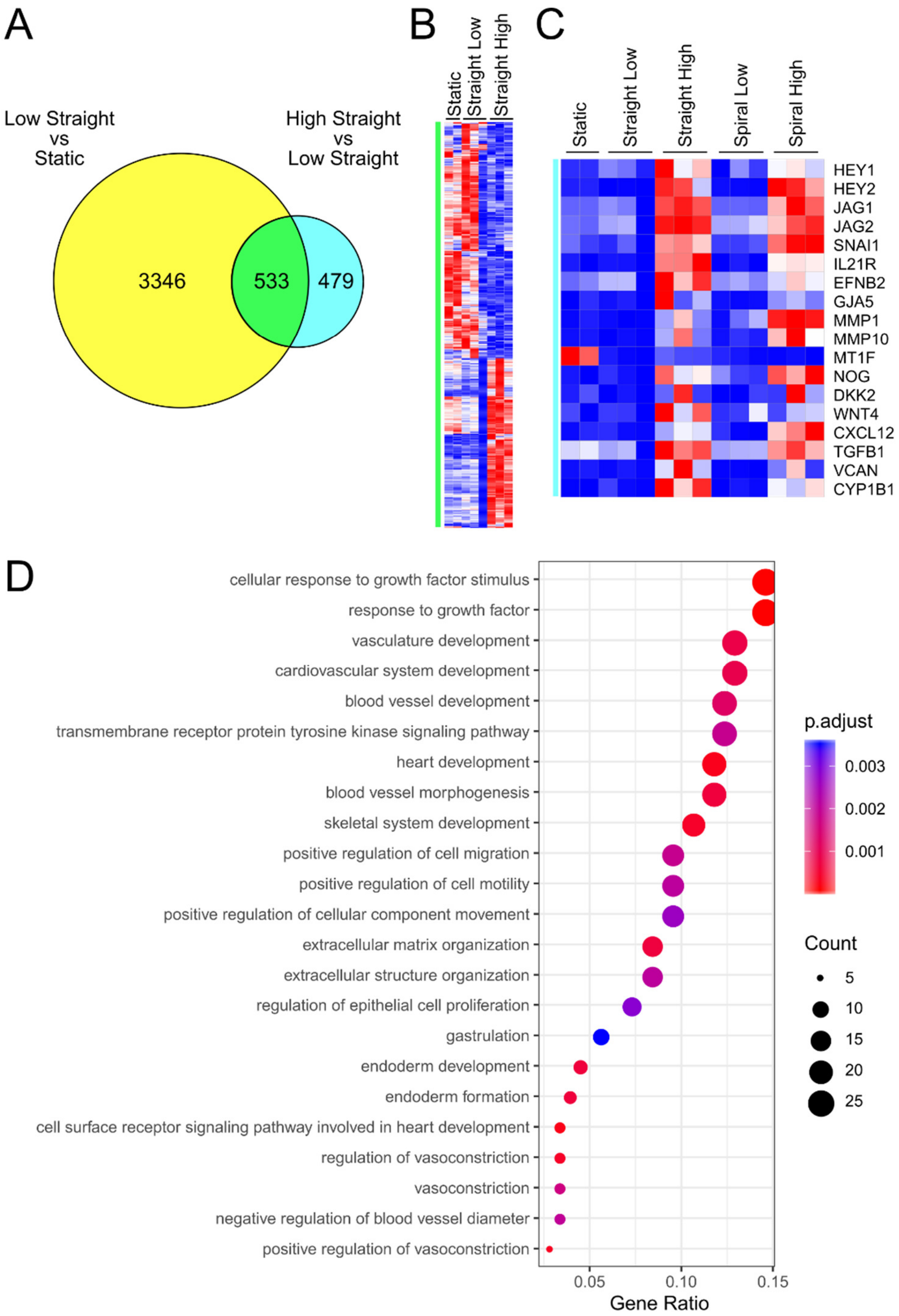

Figure A4. Bulk RNAseq comparison of spiral and straight flow to static conditions. (A) Venn diagram of significantly regulated transcripts in ECs cultured at low flow in straight tubes compared with static culture and those in high flow compared to low flow conditions in straight tubes. (B) CPM heatmap of overlapping region (green) of (A). (C) CPM heatmap of selected genes significantly regulated by increasing flow (corresponding blue region of A). (D) GO enriched terms associated with upregulated genes identified in straight high versus straight low, but not in low straight versus static.

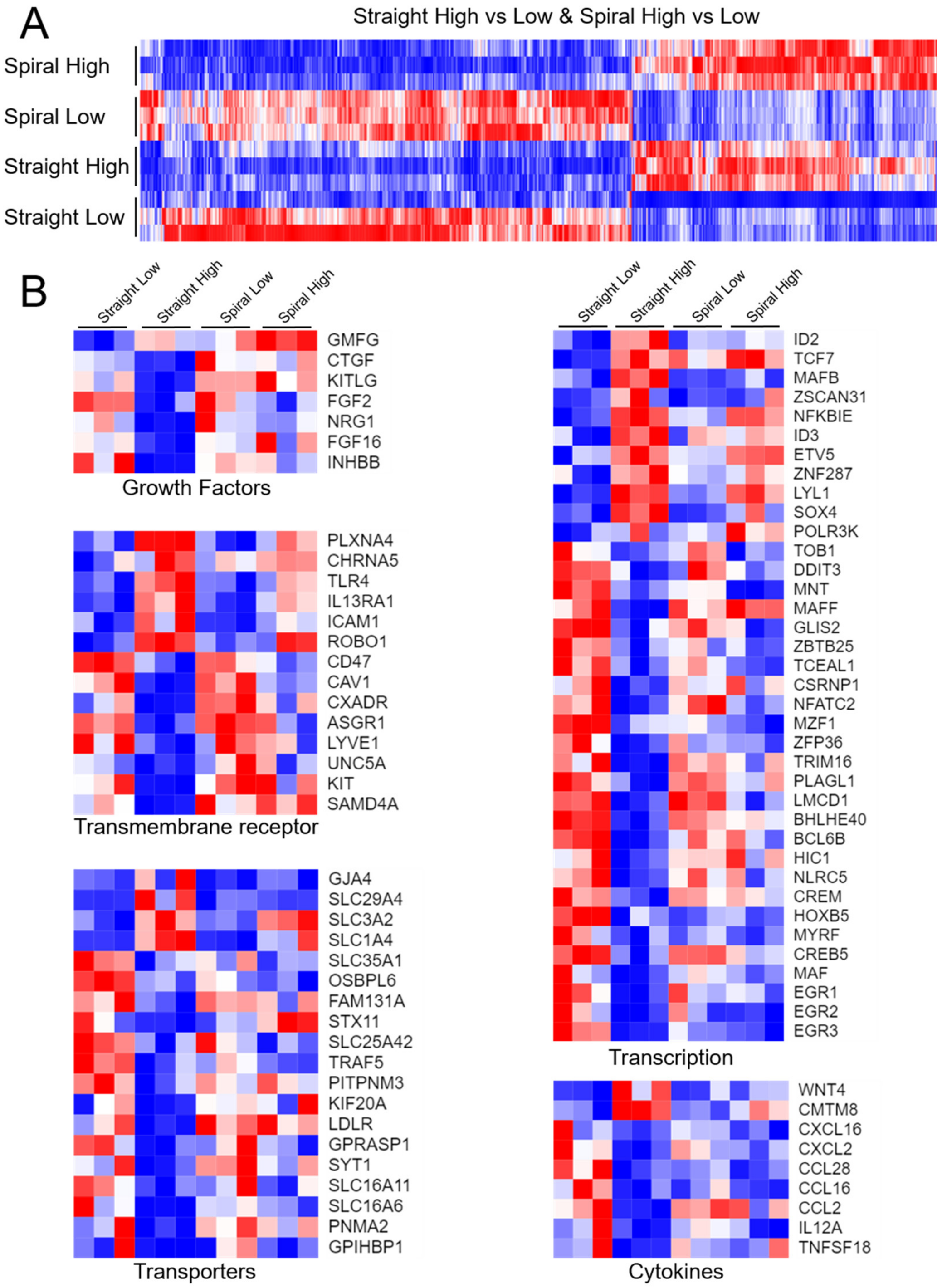

Figure A5. Genes that are significantly regulated when flow is increased in spiral or straight geometries. (A) CPM heatmaps of all genes that are significantly changed by increasing flow in both spiral and straight geometries. (B) CPM heatmaps of selected genes associated with growth factors, transmembrane receptors, transporters, transcription factors, and cytokines that are significantly changed by increasing flow in straight vessels, but not changed by increasing flow in spiral vessels.

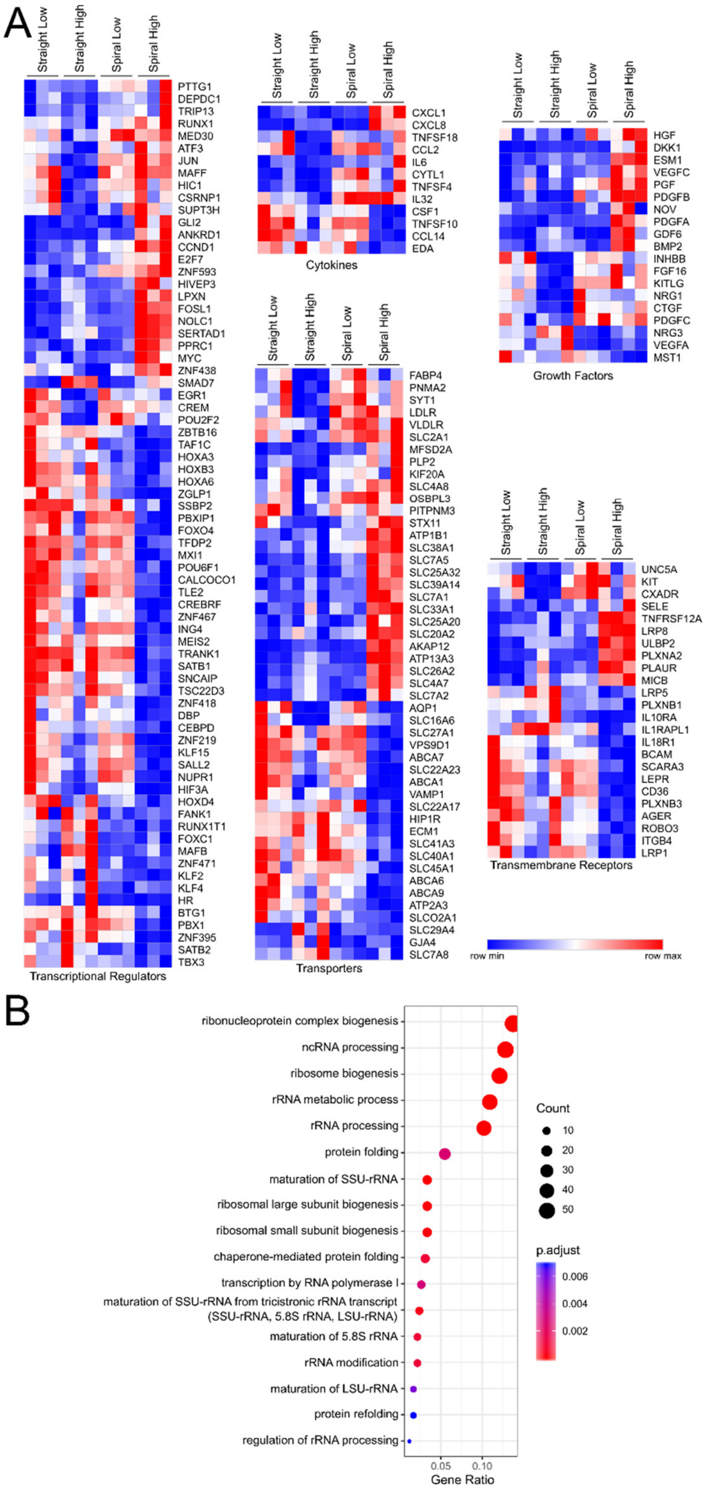

Figure A6. Genes that are significantly changed in high spiral flow. (A) CPM heatmaps of selected genes associated with transcriptional regulators, cytokines, transporters, growth factors, and transmembrane receptors that are significantly changed by increasing flow in spiral vessels, but not in straight vessels. (B) Enriched GO terms from genes significantly upregulated in spiral high flow versus low flow, but not in straight high flow versus low flow.

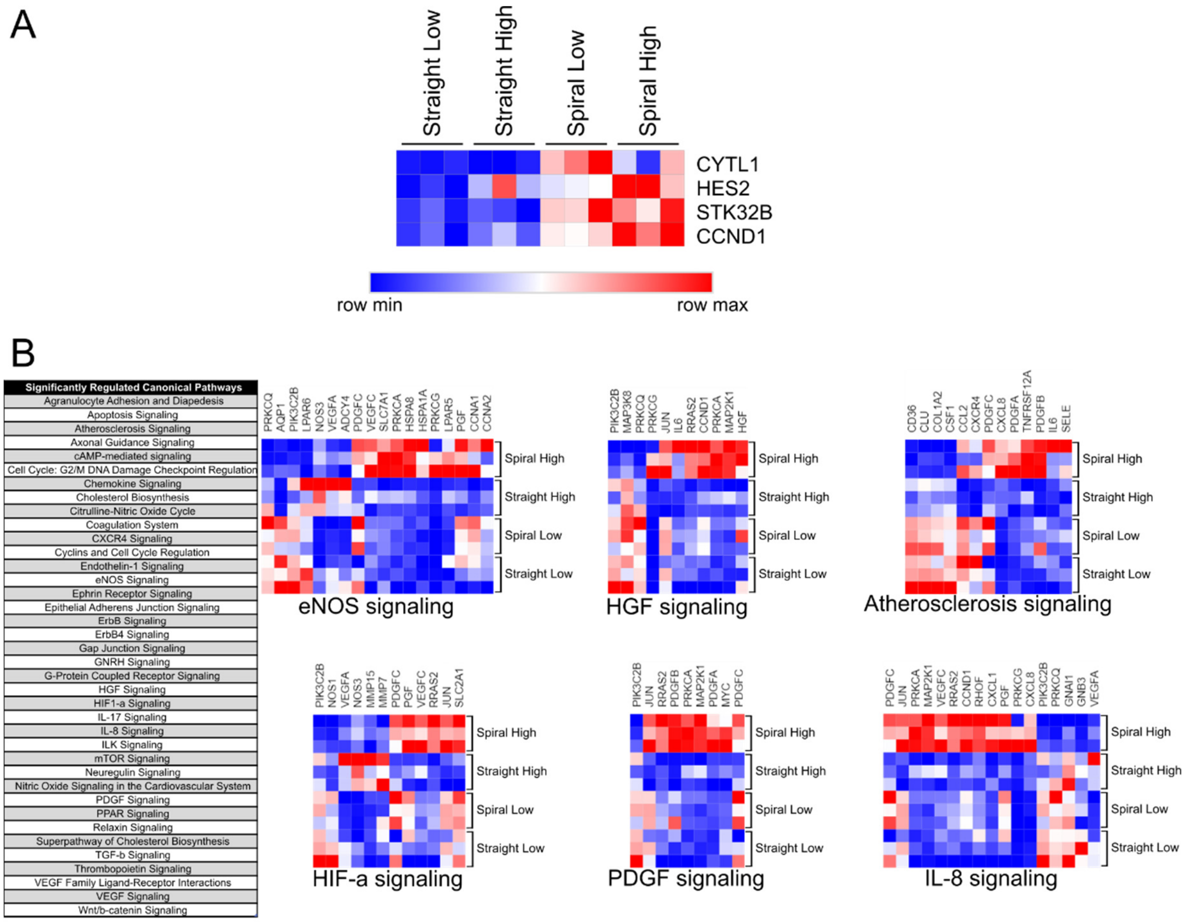

Significantly Regulated Canonical Pathways
Agranulocyte Adhesion and Diapedesis
Apoptosis Signaling
Atherosclerosis Signaling
Axonal Guidance Signaling
cAMP-mediated signaling
Cell Cycle: G2/M DNA Damage Checkpoint Regulation
Chemokine Signaling
Cholesterol Biosynthesis
Citrulline-Nitric Oxide Cycle
Coagulation System
CXCR4 Signaling
Cyclins and Cell Cycle Regulation
Endothelin-1 Signaling
eNOS Signaling
Ephrin Receptor Signaling
Epithelial Adherens Junction Signaling
ErbB Signaling
ErbB4 Signaling
Gap Junction Signaling
GNRH Signaling
G-Protein Coupled Receptor Signaling
HGF Signaling
HIF1-a Signaling
IL-17 Signaling
IL-8 Signaling
ILK Signaling
mTOR Signaling
Neuregulin Signaling
Nitric Oxide Signaling in the Cardiovascular System
PDGF Signaling
PPAR Signaling
Relaxin Signaling
Superpathway of Cholesterol Biosynthesis
TGF-b Signaling
Thrombopoietin Signaling
VEGF Family Ligand-Receptor Interactions
VEGF Signaling
Wnt/b-catenin Signaling

Figure A7. Significant differences in gene expression in low flow and Ingenuity Pathway Analysis. (A) Heatmaps of significantly upregulated genes in spiral low flow versus straight low flow. (B) Heatmaps of significantly regulated canonical pathways identified by Ingenuity Pathway Analysis (IPA) and heatmaps of genes associated with selected signaling pathways.

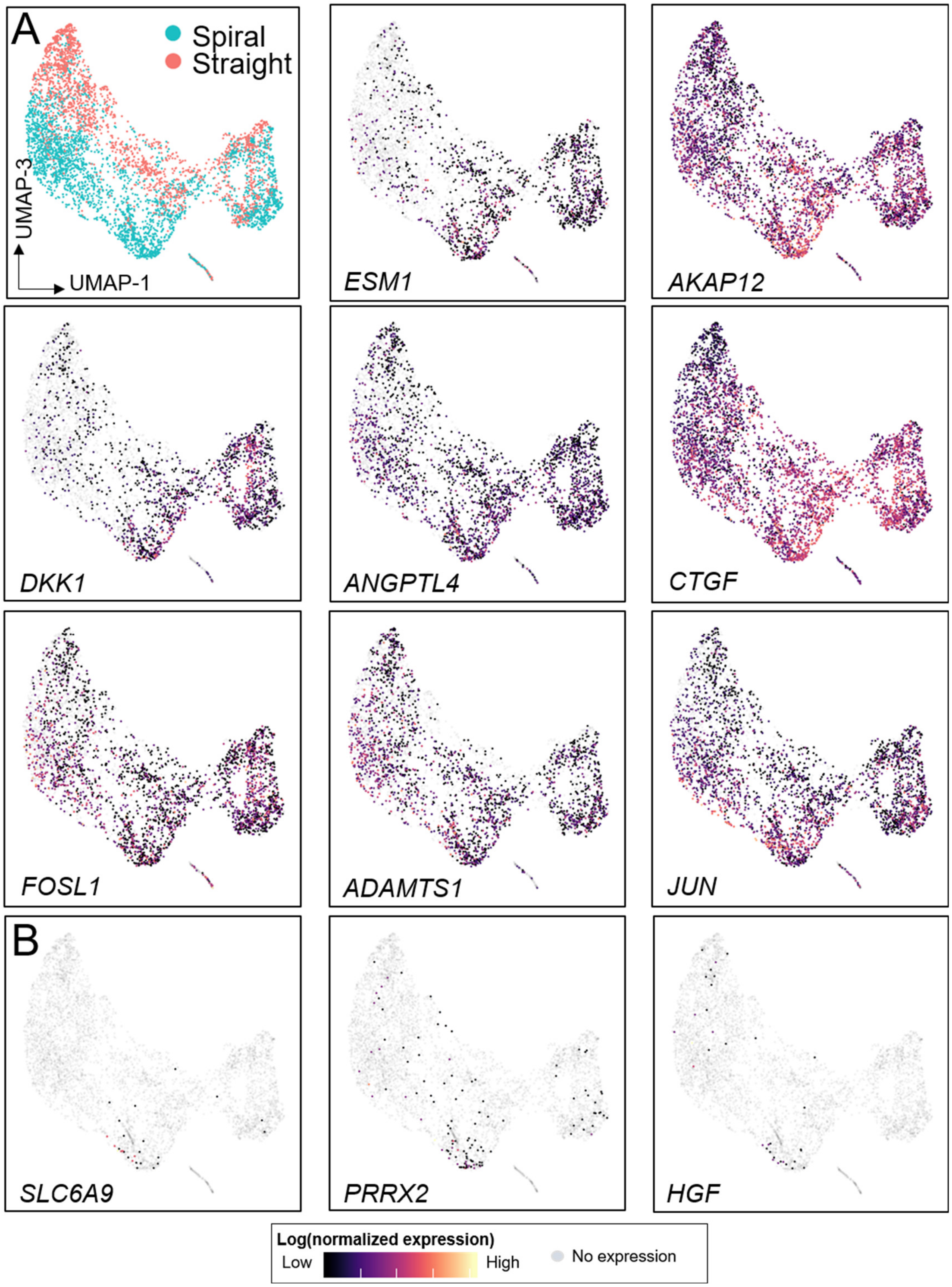

Figure A8. UMAP distribution of significantly regulated genes in both bulk and single cell RNA sequencing. (A) Selected genes that were significantly different in spiral versus straight vessels under high flow. (B) Differentially expressed genes detected in scRNAseq, but not in bulk RNA sequencing.

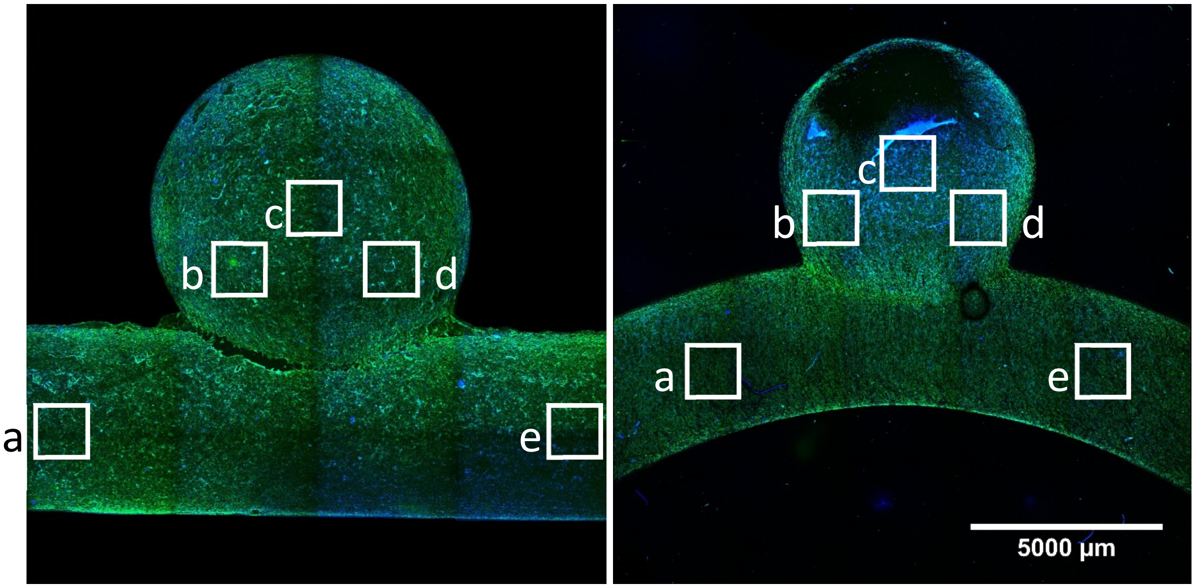

Vessel	Location	X (mm)	Y (mm)
Straight	a	-7	-4.5
Straight	b	-1.33	-1.13
Straight	c	0	0
Straight	d	1.33	-1.13
Straight	e	-7	-4.5
3 mm	a	-7.3	-6.25
3 mm	b	-1.33	-1.13
3 mm	c	0	0
3 mm	d	1.33	-1.13
3 mm	e	7.3	-6.25

Figure A9. Location of analyzed segments in idealized aneurysm models. Similar regions of straight (A) and curved (B) aneurysm models were defined for imaging where the coordinates of the center of each imaging field is listed in (C).

Figure A10. Distribution of cell angles in different idealized aneurysm geometries. Individual cell angles were determined by tracing cell borders and calculating the angle of the long axis of a best fit ellipse to the cell geometry. More than 50 cells were traced for each field. Rows represent independently perfused idealized vessels. 0 degrees = predominant direction of flow.

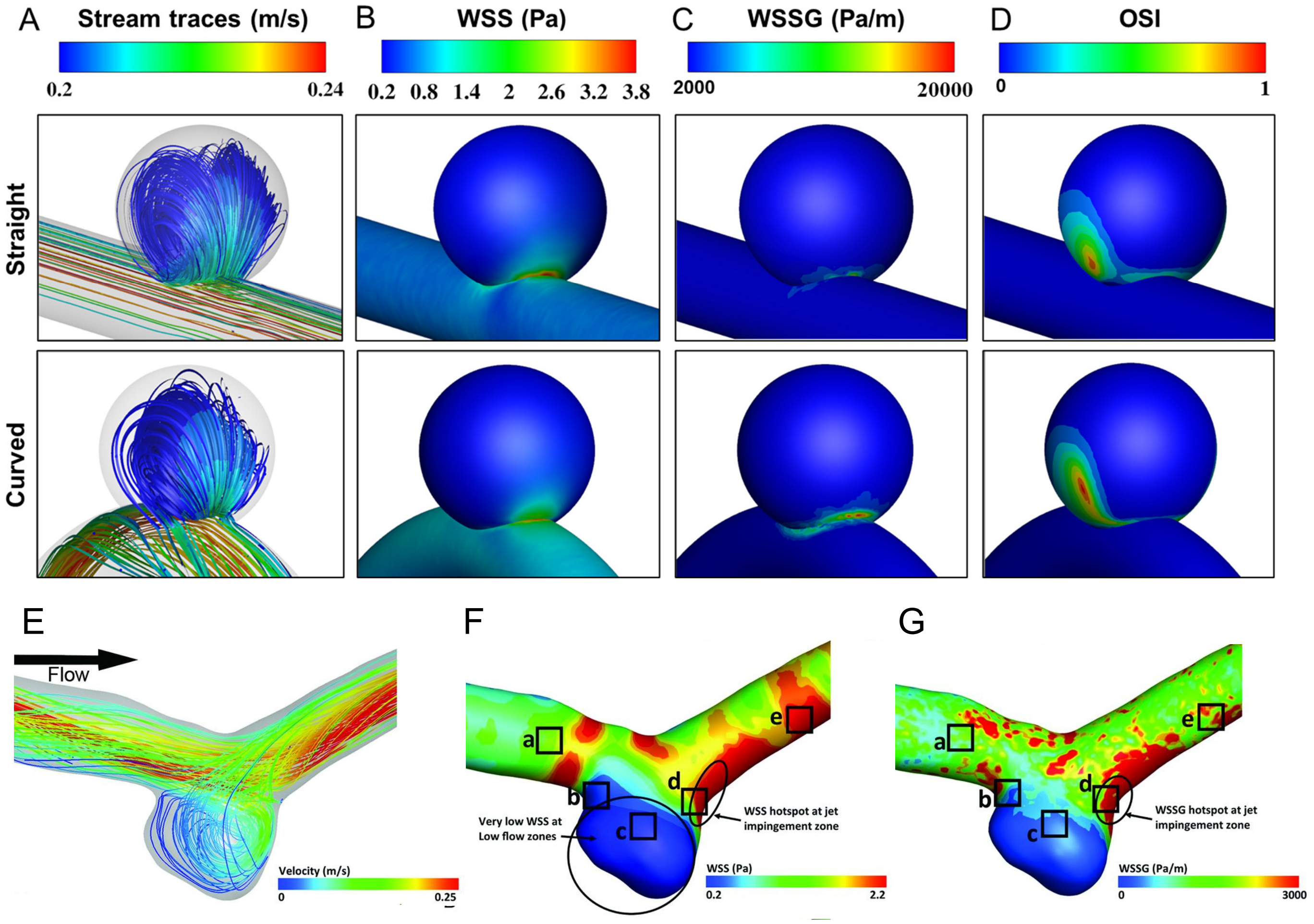

Figure A11. Computational fluid dynamic analysis of aneurysm geometries performed by Aliseda Group. Results of computational fluid dynamic (CFD) analysis of idealized aneurysm geometries showing stream traces (A), wall shear stress (WSS) distribution (B), wall shear stress gradient (WSSG) distribution (C), and oscillatory shear index (OSI) (D) in straight and curved models. Computational analysis of patient specific aneurysm geometry showing stream traces (E), WSS (F), and WSSG (G). CFD analysis was performed by members of Alberto Aliseda's group, including Venkat K Chivukula, Fanette Chassagne, and Angela Straccia.

Appendix B. Supplement to Chapter 4

Observation of pressure dependent endothelial cell morphology in spiral vessels

Spiral PDMS device fabrication and culture

400 µm spiral PDMS vessels were fabricated as described in Chapter 4 and seeded with HUVEC. Vessels were perfused at 1 µL/min for 3 days with growth media supplemented with 3.5% dextran. On day 3, vessels were separated into three flow conditions: 1 µL/min, 50 µL/min, or 100 µL/min. These flow rates were maintained for 1 hour before all devices were fixed in 4% formaldehyde for 20 minutes. Spirals were stained for VE-cadherin and nuclei and imaged by confocal microscopy.

Spiral PDMS image quantification and analysis

Regions of interest from the 2nd and 7th loop from the spiral inlet were imaged, and maximum intensity projections of confocal Z stacks were analyzed for each spiral device. Equal sized fields were selected from each image and cell area, cell perimeter, and the angle of each cell's major axis relative to the direction of flow were measured using ImageJ. Cell shape index was calculated from this data using the formula shape index = 4πA/P2. Cells with a shape index value below 0.7 (indicating a cell is round) were excluded from comparisons of the cell's major axis.

Cell morphology varies with transluminal pressure

To understand if transluminal pressure affects how endothelial cells respond to pressure we fabricated spiral vessels in PDMS and cultured cells under different flow rates. Appreciable changes in transluminal pressure develop over the length of a spiral vessel, but the wall shear stress remains constant. We compared the morphology of cells in regions of different pressure within a single spiral vessel (Figure B1A). Lower pressure regions of spiral vessels had significantly greater alignment of cells with the direction of flow than higher pressure regions in both the 50 µL/min ($p < 0.05$) and 100 µL/min ($p < 0.05$) flow condition (Figure B1B, C). No significant difference in alignment was observed between high and low-pressure regions of 1 µL/min vessels. Differences between these regions persisted in terms of cell area (Figure B1D). Cell area was significantly greater in lower pressure regions than in higher pressure regions in vessels exposed to 50 µL/min ($p < 0.05$) and 100 µL/in ($p < 0.05$) flow. Under 1 µL/min flow, cell area was unchanged in different vessel regions.

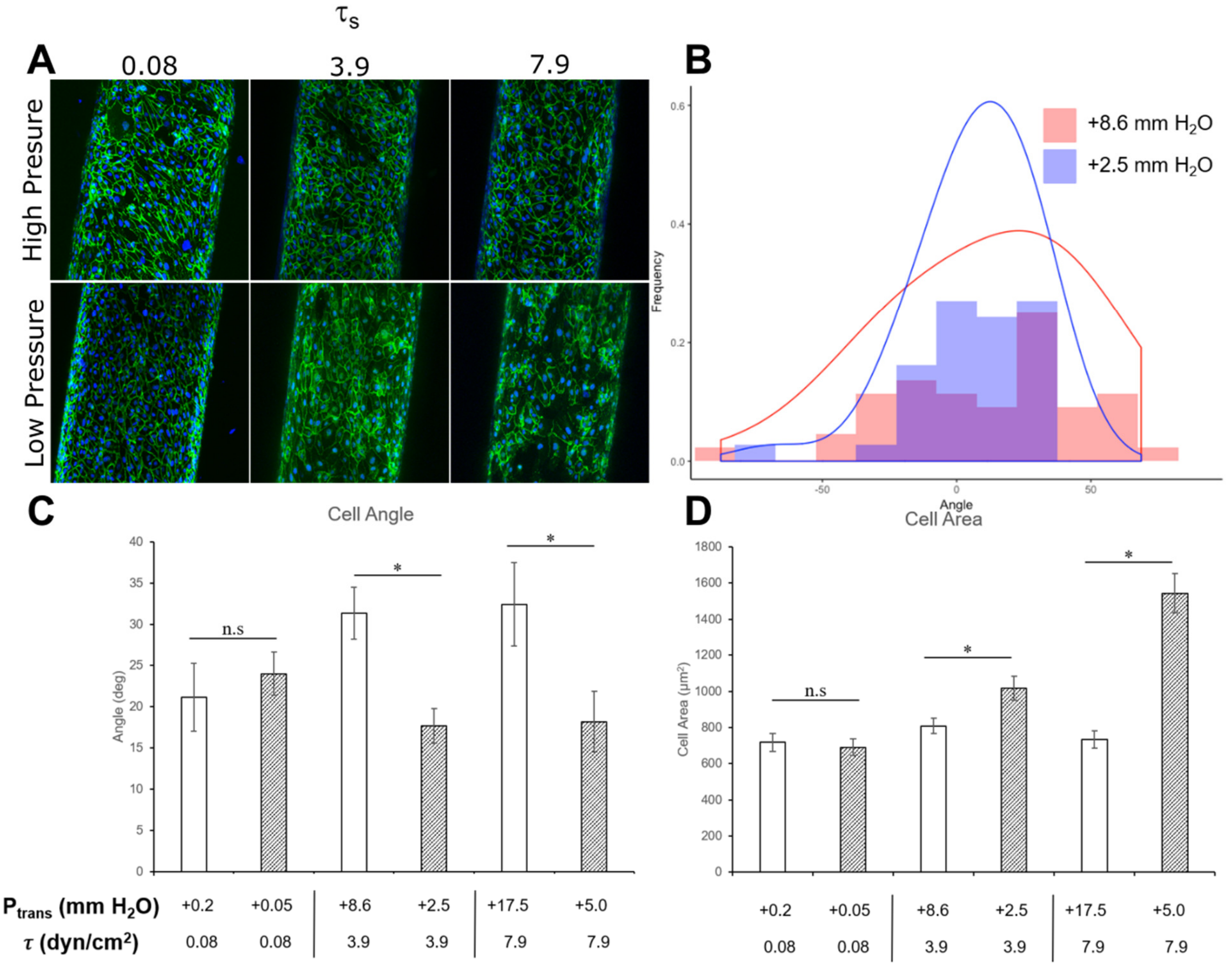

Figure B1. Endothelial cells are more responsive to shear stress at lower pressures. (A) Representative images of regions of interest in spiral vessels under different shear stresses (Green = VE-cadherin, Blue = nuclei). Cells in lower pressure regions of the vessel were significantly more aligned in the direction of flow (B, representative distribution, 0 deg = flow direction). For low flow, no change in alignment was observed. Cell area was also dependent on location, where we observed significantly larger cells in lower pressure regions of spiral vessels under moderate and high flow rates (D). * $p < 0.05$.

Appendix C. Two photon fabrication of biologically inspired microvasculature

Biofabrication of physiologic scale microvessels

This work has highlighted that shear stress, pressure, and geometry all contribute to the endothelial response to blood flow. Limitations in current engineering approaches, however, have left blind spots in our understanding of the role of these forces in true microvascular and capillary scale vessels. Our casting approaches, as well as advanced 3D bioprinting techniques struggle to generate vascular structures below 100 μm in diameter, despite the abundance of these vessels in vivo. While some approaches produced lumen less than 50 μm in diameter, these often faced challenges to seeding and did not have complete control over the fabricated geometry. For example, spun microfiber meshes made from a dissolvable material[1] have been used to generate capillary lumen in a hydrogel, but these could not be reliably seeded with endothelial cells and the geometry of the network was random and uncontrolled. Recent advances from our lab have shown that two-photon (2P) microscopy can be used to generate capillary scale vessels in collagen hydrogels by laser ablation.[2] This first-of-its-kind controlled fabrication of capillaries revealed novel interactions between capillary endothelial cells and malaria infected red blood cells, but it was technically limited to hand-drawn geometries. We sought to extend this approach to arbitrary geometries and incorporate multiple cell types to better mimic the vascular structure of native tissue and to enable the controlled study of hemodynamic forces in these environments.

A 3D Model to Microscope Pipeline

The process of converting a digitized 3D object to a physical object has been tackled for decades in manufacturing industries utilizing computer numerical control (CNC) and has been democratized in the last decade with the advent of consumer 3D printing. Whether using a subtractive manufacturing technique (e.g. milling) or an additive one (e.g. 3D printing), the generalized workflow involves converting a 3D geometry into instructions for a machine to either remove material that does not belong in the final structure, or to add material until the final structure has been achieved. Here, we adopted a 3D-printing like approach, but adapted to the subtractive nature of 2P ablation.

The workflow involves (1) model generation, (2) model slicing, (3) model conversion to microscopy format, and (4) 2P ablation. We utilized geometries designed in computer aided design software (Fusion 360, Autodesk) as well as geometries derived from 2P imaging of the mouse cerebral cortex. These files were converted to a 3D mesh format (.stl) and imported into a commercially available slicing software (Autodesk Netfabb 2019). Whole 3D models were sliced into a series of 1 µm thick layers and converted into vector graphics files (.svg) which contain the bounding points of the model geometry. A custom script was written to then convert the vector graphics file into a format accepted by the Olympus Fluoview software to drive an Olympus FV1000 Multi-photon microscope. The built-in multi-area time lapse (MATL) feature was used as the basis for bringing custom data into the microscope environment. In normal use the MATL function enables users to program acquisition parameters including laser settings, position settings, regions of interest, and other imaging information from within the Fluoview workspace. This information is stored in a Microsoft Access Database and is readily modified programmatically. Using R, the XY coordinates defining polygonal regions of interest were imported from vector graphics files into the Access database along with ablation parameters including slice thickness, laser power, and pixel dwell time. Through this workflow approximately 3000 custom polygons can be automatically programmed for ablation in a single run on the microscope. For complex structures that require more polygons, the ablation can be split among multiple files and then run in sequence to produce the final structure. Once created, these customized files can be opened within the Fluoview software and are run like any other image acquisition.

Representative structures

To demonstrate the power of this approach, we fabricated several example geometries of varying complexity. To explore the minimum feature size of structures we ablated a 3D basketweave pattern in which two orthogonal vascular networks interdigitated but remained independently perfusable with fluorescent microbeads (Figure C1A). The diameter of each vessel is approximately 15 µm, and individual vessels are approximately 15 µm from the nearest neighboring vessel. Next, we designed a model Bowman's capsule featuring a tortuous 15 µm diameter glomerular vessel surrounded by an independently perfused 300 µm capsule (Figure C1B). Finally, 2P imaging data from the mouse cerebral cortex microvasculature was segmented into a 3D model and used to ablate collagen vessels (Figure C1C).

Engineering hierarchy through ablation

A major challenge in vascular engineering is re-creating the hierarchy and endothelial heterogeneity present throughout the vasculature. Smooth muscle and perivascular cell coating of blood vessels progressively decreases as vessels approach capillary diameters. Endothelial cells themselves vary significantly depending on the organ and vascular bed in where they reside, suggesting that engineered tissues should have compartmentalized endothelial populations for optimal tissue function. Neither of these features have been reproduced reliably in engineered tissues due to the difficulty of selectively populating regions

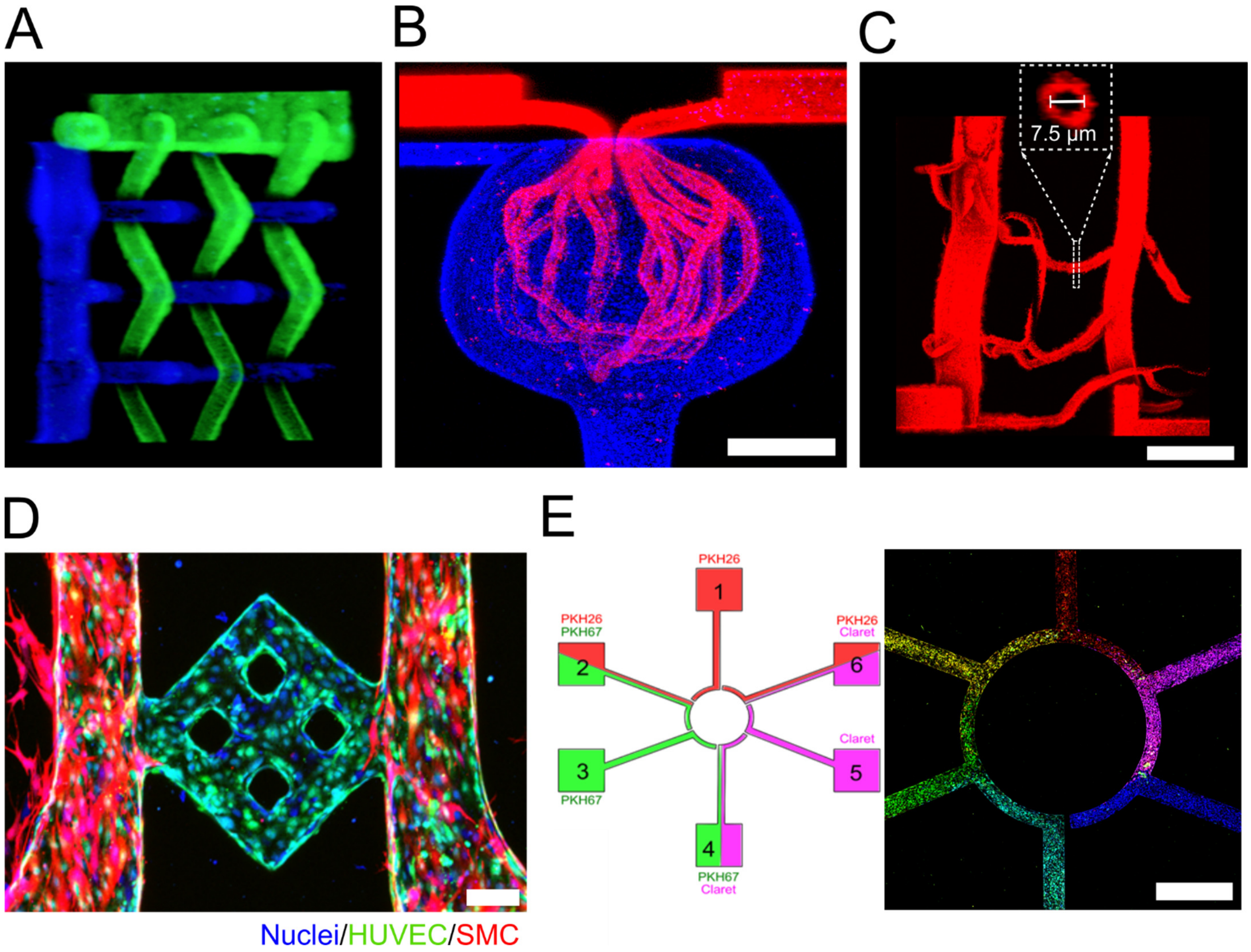

Figure C1. Representative 2P ablated structures. (**A**) Ablated basketweave structure (vessel diameter = 15 μm) perfused with blue and green beads. (**B**) Engineered model glomerulus, with vessels perfused with red beads and Bowman's space perfused with blue beads. (**C**) Imaging data from mouse cerebral cortex was used to ablate and perfuse small vessels. (**D**) Hierarchical vessel seeded with smooth muscle cells and endothelial cells in the outer channels, but only endothelial cells in the center. (**E**) Multiple endothelial populations stained with different combinations of membrane dye occupying a single continuous vessel after connecting with 2P ablation. Scale in B, C E = 100 μm. Scale in D = 1 mm.

of the vasculature. 2P ablation provides a method for addressing both challenges through multiple rounds of seeding and ablation.

To demonstrate the process for generating a selectively muscularized vessel, we first created two parallel, but independently perfused lumen with a 500 μm space separating them. We seeded the two channels first with smooth muscle cells and allowed them to them to adhere overnight. We next ablated a connection between the two muscularized parent vessels and immediately seeded endothelial cells into the now continuous network. This sequence resulted in a continuous layer of endothelial cells throughout the entire vessel, but smooth muscle cells surrounded the endothelial cells only in the parent vessels, mimicking the organization of an arteriole-capillary-venule unit. While simplified in this example, this approach could be extended to more complicated geometries and additional cell types and compartments.

Using a similar strategy, we sought to demonstrate how distinct endothelial compartments could be connected in a continuous vessel by ablation. In place of unique endothelial cells, we generated 6 uniquely colored populations of human umbilical vein endothelial cells using 6 combinations of 3 different membrane dyes (PKH67, PKH26, and CellVue Claret, Sigma). We then seeded these populations into 6 independent compartments arranged in a disconnected circle. Following seeding we ablated connections between compartments to complete the circle. Cells spread into the ablated regions but maintained their distinct localization while in under flow in a single continuous channel.

References

1. Lee, J. B. *et al.* Development of 3D Microvascular Networks Within Gelatin Hydrogels Using Thermoresponsive Sacrificial Microfibers. *Adv. Healthc. Mater.* **5**, 781–5 (2016).
2. Arakawa, C. *et al.* Biophysical and biomolecular interactions of malaria-infected erythrocytes in engineered human capillaries. *Sci. Adv.* **6**, eaay7243 (2020).